Multi-phase and multi-material interactions in granular media

Caroline Chalak

Communauté
UNIVERSITÉ Grenoble Alpes

THÈSE

Pour obtenir le grade de

DOCTEUR DE LA COMMUNAUTE UNIVERSITE GRENOBLE ALPES

Spécialité : **Matériaux, Mécanique, Génie Civil, Electrochimie**

Arrêté ministériel : 7 août 2006

Présentée par

Caroline Chalak

Thèse dirigée par **Félix Darve** et
codirigée par **Bruno Chareyre**

préparée au sein du **Laboratoire 3SR (Sols, Solides, Structures, Risques)**
dans **l'École Doctorale IMEP-2 (Matériaux, Mécanique, Energétique, Environnent, Procèdes, Production)**

Multi-phase and Multi-material Interactions in Granular Media

Thèse soutenue publiquement le **1er juillet 2016**,
devant le jury composé de :

M. Bernard Cambou
Professeur émérite, Ecole centrale de Lyon , Président du jury
M. Olivier Millet
Professeur, Université de la Rochelle, Rapporteur
M. Jean-Yves Delenne
Directeur de recherche, Université de Montpellier 2, Rapporteur
M. Patrick Selvadurai
Professeur, Université de McGill (Canada), Examinateur
M. Ehsan Nikooee
Dr, Université de Utrecht (Pays-Bas) , Invité
M. Felix Darve
Professeur émérite, INP Grenoble , Directeur de thèse
M. Bruno Chareyre
Maitre de conférence, INP Grenoble , Co - encadrant de thèse

Acknowledgements

I would like to acknowledge in the beginning my parents Fadi and Hiba who encouraged me to start the International Master "Geomechanics, Civil Engineering and Risk" in Grenoble and were always supporting me. Many thanks also to Prof. Cino Viggiani for all the support during the master year and after during the PhD as well not only in the scientific context but also for his human qualities.

I would also like to thank Helen Lewis, Gary Couples and Emmanuel Lecomte for introducing me to the research world, when I did my Master thesis with them in Edinburgh, Scotland. It has been a privilege to work with them: scientific competence, friendly manners, human qualities... They made my first research experience quite enjoyable, and it is because of this that I pursued my work in research afterwards.

In Edinburgh, I met also great friends that made my stay in Scotland just wonderful!: Nikhil,Dima, Harina, Nina, Alex, Judd, Aicha, Mojtaba, Reza, Babak, Behnaz, Samira, Morteza..

Thanks to my supervisors Felix Darve and Bruno Chareyre for the advises and comments during the PhD, and to Prof. Selvadurai for all the discussions and the review and useful remarks on the part of the work I did with him to help improve the quality of the work and this manuscript..

My PhD thesis was funded by the Marie Curie ITN Project MuMoLaDe that is to be thanked deeply for giving me the opportunity to be a part of this project. In the framework of the MuMoLaDe project, I would like to thank Prof. Wei Wu the coordinator of the project and Mr. Faquiang and Gregor. Big thanks to the MuMoLaDe group, with whom I spent really good time, and adventures (scientific and personal) to keep as great memories, they were all and still great friends (Eva, Maria, Toan, Alessandro, Konstantine, Miguel, Barbara, Peng, Vasilis, ALexandra, Pablo, Lorenzo, Xiaogang, Xiannan Adel).

Special thanks to the very good people and friends I met in Grenoble, Zeynapouli, Ranime, Benjamin, Stiven, Yen-Shin, Evangelia, Christinaki, Elenaki, Rahaf, Bassel, Mireille, Eleonor, Sheherezade ... We spent together great moments and they were always there for me when help is needed.

Many thanks to the people I met in Lyon, for the nice company and the support in my teaching experience, the scientific discussions and their understanding until I finished my PhD thesis: Laurent Briancon, Christian Olagnon, Claire Silvani, ALi Daouadji, Irini Djeran-Maigre, Florent Prunier, Noureddine , Jostar , Christine, Jean, ... ; and of course for my friends Souha, Tala, Louis, ALejandro, and Francois.

Finally , the last thanks are said to be the most important, so thank you again for my family mom, dad and brothers, and a very special acknowledgement goes to Marco for being what he is and for being a part of my life.

Abstract

The discrete element method is used to study two interaction types in granular materials for two different applications.

The first application embodies hydromechanical coupling to study the behavior of unsaturated granular materials. An extended numerical model of pendular bridge for spherical grains is introduced, enabling the determination of interfacial areas and taking into account the roughness of the grains. On this basis, the free energy of interfaces is defined, and its changes are found to balance the mechanical work exerted by the bridge on the particles of a two grain system, following the first law of thermodynamics. The model enables tracking the changes of free energy in deforming granular systems simulated with the discrete element method. Simulations of regular and random packings are presented to discuss the effective stress concept and check whether the Love-Weber expression of averaged stress is able to describe well the behavior of partially saturated granular materials for different configurations and mechanical aspects. Though frequently supposed to play the role of effective stress in multiphase systems, the Love-Weber stress is found to be valid only for regular packings to describe the deformation behavior in the elastic regime. In random packings, it does not compare consistently with the changes of elastic free energy. At the peak for shear strength, Love-Weber stress can be defined as a possible micromechanical effective stress formula for some configurations. It verifies a unique Mohr-Coulomb rupture envelop when the envelops are plotted in p_{cont}, q_{cont} in the case of random packings with rough /smooth grains and tightly graded particle size distributions. It is however shown that this property does not hold for all the possible particle size distributions.

The pendular bridge model is coupled with the funicular model of [94] allows the simulation of a full drainage process where it is shown that the addition of the menisci have a noticeable impact on the behavior of unsaturated soils.

The second application embodies particle-elastic continuum interaction to study the compaction of proppant region that is of big importance in the oil and gas production industry. A granular pile is compacted between two rigid plates. The stress distribution induced by the pile of proppants on the plates is investigated and related to the aperture of the frac-

ture and the contact zone on each plate. This stress distribution can be used to improve the results of the analytic solutions. The influence of friction angle between the grains and the grains and the plates are also investigated. The rigid plates are replaced in a second part by an elastic rock block simulated using DEM, gluing- particles together with elastic contacts. DEM is shown to be adequate to simulate an elastic continuum medium as the comparison of the analysis of a rigid disc inclusion problem in the discrete rock block with analytic results of [79] fit very well. The rigid shaped disc is replaced by a granular proppant afterwards and the geometry of the fracture for different overburden stress values is investigated.

Keywords : Granular material, partially saturated, thermodynamics, interfaces, effective stress, proppant.

Resumé

La méthode des éléments discrets est utilisée pour étudier deux types d'intéraction dans les matériaux granulaires pour deux applications différentes.

La première application introduit un couplage hydromécanique pour étudier le comportement des matériaux granulaires partiellement saturés. Un modèle numérique en régime pendulaire pour les grains sphériques permettant la détermination des aires interfaciales et tenant compte de la rugosité des grains est développé. Sur cette base, l'énergie libre des interfaces est définie, et sa variation se trouve à équilibrer le travail mécanique exercée par le pont liquide sur les particules d'un système à deux grains conformément à la première loi de la thermodynamique. Le modèle permet de détecter l'evolution de l'énergie libre dans les systèmes granulaires deformés et simulés avec la méthode des éléments discrets. Des simulations sur des assemblages réguliers et aléatoires sont présentés pour discuter le concept de la contrainte effective et vérifier si l'expression Love-Weber de contrainte moyennée décrit bien le comportement des matériaux granulaires partiellement saturés pour différentes configurations et aspects mécaniques. Bien souvent censé jouer le rôle de la contrainte effective dans les systèmes multiphasiques, la contrainte moyennée de Love-Weber n'est valable que pour des assemblages réguliers en régime élastique. En cas d'assemblages aléatoires, elle ne compare pas toujours avec les variations de l'énérgie libre élastique. Au pic pour la résistance au cisaillement, Love-Weber vérifie une enveloppe de rupture Mohr-Coulomb unique pour les assemblages avec une granulometrie uniforme ; elle peut alors être défini comme une possible formulation de contrainte effective micromécanique dans ce cas. Il est cependant montré que cette hypothèse n'est pas valable pour toutes les configurations de granulometrie possibles. Le modèle pendulaire est couplé avec le modèle funiculaire de [94], ce qui permet la simulation d'un drainage complet. Les résultats montrent que l'addition des ménisques a un impact important sur le comportement mécanique des sols non saturés .

La deuxième application introduit les interactions des grains avec un milieu élastique continu pour étudier la compaction des agents de soutènement (proppants) qui est d'une grande importance dans l'industrie de la production pétrolière. Un tas granulaire est compactée entre deux plaques rigides. La répartition des contraintes induites par le tas d'agents de soutènement sur les plaques est étudiée et reliée à l'ouverture de la fissure et la zone de contact sur chaque plaque. L'influence de l'angle de frottement entre les grains et entre les grains et les plaques est également étudiée. Les plaques rigides sont remplacés dans une deuxième partie par un bloc rocheux élastique simulé à l'aide de la DEM,en collant des particules entre elles par une très forte cohésion ajoutée aux contacts. La DEM est trouvée

capable de simuler un milieu de continu élastique, vue que la comparaison de l'analyse d'un problème d'inclusion d'un disque rigide dans le bloc rocheux avec les résultats analytiques de [79] est très proche. La géométrie de la fracture lorsque le disque rigide est remplacé par un tas de proppants granulaire est finalement présentée pour différentes valeurs de contrainte verticales.

Mots clés : Matériau granulaire, partiallemment saturé, thermodynamiques , interfaces, contrainte effective , proppant.

Contents

Contents **7**

List of Figures **11**

List of Tables **17**

1 Introduction **1**

1.1 Introduction 1

1.2 Unsaturated soils 3

1.2.1 DEM modeling of wet granular media 8

1.2.2 Effective stress concept in unsaturated soils 10

1.3 Compaction of proppant region. 14

2 DEM modelling of unsaturated soils **17**

2.1 Introduction 17

2.2 Discrete element method 17

2.2.1 Computational cycle 18

2.2.2 Interaction law 19

2.2.3 Critical time step 21

2.3 Numerical model: the pendular model 22

2.3.1 Assumptions for the numerical model 22

2.3.2 Young-Laplace equation 24

2.3.3 Roughness of the grains 31

2.4 Capillary Interaction Law: look up table 34

2.5 Limitation of the model 36

2.6 Conclusion 38

3 Energetic study of three phase systems **41**
3.1 Introduction . . . 41
3.2 Energy balance of a two-grain system . . . 41
3.2.1 External work . . . 42
3.2.2 Internal energies . . . 43
3.3 Model verification . . . 46
3.3.1 External work input . . . 46
3.3.2 Internal free energy . . . 48
3.3.3 Energy balance . . . 49
3.3.4 Movement at constant suction or constant volume . . . 51
3.4 Energy balance of a packing . . . 52
3.4.1 Sample preparation . . . 52
3.4.2 Energy balance . . . 53
3.5 Energy balance: Energy loss/gain and plasticity . . . 55
3.5.1 Two grains system: breakage or formation of a meniscus . . . 55
3.5.2 Energy balance for a packing . . . 56
3.6 Conclusion . . . 58

4 Effective stress in three phase granular materials **61**
4.1 Introduction . . . 61
4.2 Effective stress in the pendular regime in granular materials subjected to small deformation . . . 62
4.2.1 Contact stress . . . 63
4.2.2 Regular packings . . . 64
4.2.3 Random packings . . . 65
4.3 Conclusion . . . 70

5 Roughness and particle size distribution effects on the shear strength properties of unsaturated granular material in the pendular regime **73**
5.1 Introduction . . . 73
5.2 The roughness of the grains . . . 74
5.3 The particle size distribution of the grains . . . 78
5.3.1 Influence of the particle size distribution on the friction angle. . . . 85
5.3.2 Contact Stress vs Effective Stress . . . 86
5.4 Conclusion . . . 91

6 Pore-scale simulation of drainage in granular materials: Passage from saturated to funicular to pendular regimes 95
6.1 Introduction . . . 95
6.2 DEM-PFV model . . . 96
6.2.1 Drainage . . . 97
6.2.2 Forces on the particles . . . 98
6.2.3 Stresses . . . 101
6.3 Pendular + Funicular model . . . 101
6.4 Sample Preparation . . . 104
6.5 Results and discussion . . . 104
6.5.1 Hydraulic behavior . . . 104
6.5.2 Mechanical behavior . . . 110
6.5.3 $p_c - \varepsilon - S_r$ relationship . . . 110
6.6 Conclusion . . . 114

7 Compaction of a proppant region using DEM 119
7.1 Introduction . . . 119
7.2 Development of the DEM model for the proppant region . . . 129
7.3 Proppant Compaction . . . 129
7.4 Stress distribution . . . 133
7.5 Influence of the plate friction angle . . . 136
7.6 Influence of the inter-granular friction angle . . . 138

8 Simulation of the compression of proppant between two similar elastic rock blocks. 143
8.1 Introduction . . . 143
8.2 Simulation of the compression of a rigid disc inclusion between two similar elastic rock blocks. . . . 144
8.2.1 Model description . . . 144
8.2.2 Elastic properties of the rock block . . . 147
8.2.3 Fracture opening and stress distribution . . . 149
8.2.4 Validation of the results . . . 151
8.3 Simulation of the compression of granular proppant between two similar elastic rock blocks. . . . 153
8.3.1 Model description . . . 153
8.3.2 Fracture opening . . . 157

8.4 Conclusion 158

9 Conclusion and Perspectives **163**

9.1 Multiphase system 163

9.1.1 Conclusions 163

9.1.2 Perspectives 164

9.2 Multi-material system 165

9.2.1 Conclusions 165

9.2.2 Perspectives 165

Bibliography **167**

List of Figures

1.1 Illustration of different regimes of unsaturated soils 5
1.2 Patterns of drainage and imbibition for pores in parallel and in series 6
1.3 The surface tension 7
1.4 The water soil retention curves in a sand taken from [24] 7
1.5 Water retention curves for various types of soil (from [12]) 8
1.6 The Mohr Coulomb rupture envelop and the evolution of the cohesion with the water content from the work of [71] 9
1.7 The retenstion curve presented by [23] by DEM. 10
1.8 The effective stress parameter versus the degree of saturation from [95] . . 12
1.9 (a) 2D plot of the wetting and drying paths and (b) 3D plot of suction stress for Buffalo dam clay (the experimental data is from [40]). The figure is from [58] 15

2.1 Computational cycle of a DEM model. 19
2.2 Contact variables: stiffnesses and friction angle 20
2.3 Elastic contact law for normal interaction and elastic-plastic tangential interaction. 21
2.4 Illustration of different roughness regimes and the dependency of the capillary law on the volume of the wetting liquid. 24
2.5 Illustration of a liquid bridge connecting two particles. 25
2.6 Illustration of the three interfaces. 27
2.7 Output variables of Young-Laplace equations for different suction values. . 28
2.8 The energy of interfaces corresponding to the solutions of Laplace-Young equation for various suctions. 29
2.9 The identified stable solution of Laplace-Young for various suction values. . 30
2.10 Illustration of particles with (a) negative and (b) positive roughness. 31

2.11 (a)Negative and (b)Positive roughness as taken into account in the numerical model. 32
2.12 Influence of the suction change on the capillary force for various values of roughness for two grains in contact. 33
2.13 Interpolation scheme for a random configuration from the look up table discrete solutions, in the case of suction and volume control 35
2.14 Comparison between the suction and volume control for a random configuration showing the variation of suction, volume, force and interfaces with the distance between the grains. 37
2.15 Illustration of menisci starting to overlap. 38

3.1 Idealized system inspired by the work of Morrow (1970) [54] 42
3.2 Illustration of the three existing interfaces 46
3.3 The path of the external work applied to the system as function of the suction and the relative displacement 47
3.4 The change of elastic energy , interfacial energy and total internal energy as function of(a)relative displacement and (b) suction. 48
3.5 The energy change of each interface and the total capillary energy change as function of (a) relative displacement and (b) suction. 50
3.6 The energy balance of the system as function of (a) relative displacement and (b) suction 51
3.7 Energy balance for the path A $\rightarrow$ B for suction and volume control cases. . 52
3.8 Energy balance verification for a packing 55
3.9 The energy balance showing the energy loss when the meniscus is broken . 57
3.10 59

4.1 (a)-Illustration of regular cubic packing and (b)- random packing with periodic boundary conditions 64
4.2 The components of external work and internal energy for wet packing in the case of isotropic compression for (a)-dense packing and (b)-loose packing . 66
4.3 The variation with the degree of saturation of the derivative of internal energies for a dense and loose packing 67
4.4 The variation of the difference between effective and contact stress with the degree of saturation in pendular regime for (a)dense packing and (b)loose packing 68

4.5 The logarithmic distribution of the PDF of the normal forces for (a)-dry and (b)- wet dense samples. 69
4.6 The probability density functions of (a) normal forces and (b) shear forces in dry and wet dense samples 70

5.1 Unique rupture envelop obtained by the intergranular contact stress for various saturations from [74] 74
5.2 Mohr-Coulomb envelops for different roughness values ($\kappa = 0, -1, 2$ %) for $S_r = 0.01$ 75
5.3 The evolution of the force with the suction for various roughness values ($\kappa = 0, -1, 2$ %) in the case 2 grains in contact. 76
5.4 Mohr-Coulomb envelops for different roughness values for various degrees of saturation 77
5.5 The evolution of the cohesion with the saturation for various roughness values ($\kappa = 0, -1, 2$ %) 78
5.6 q_{cap} plotted as function of p_{cap} for different roughness values ($\kappa = 0, -1, 2$ %). 79
5.7 Unique rupture envelop obtained by the intergranular contact stress for various roughness values ($\kappa = 0, -1, 2$ %). 79
5.8 The granulometric curve as taken into account in the DEM simulations. . . 80
5.9 Mohr-Coulomb envelops for different saturation and different p_p values (r=0.5). 81
5.10 Mohr-Coulomb envelops for different saturation and different r values ($p_p =$ 0.5). 82
5.11 The cohesion as function of the degree of saturation for various p_p values (r=0.5). 84
5.12 The cohesion as function of the degree of saturation for various r values (p_p=0.5). 85
5.13 The normalized cohesion as function of the degree of saturation for various (a) r (p_p=0.5) and (b) p values (r=0.5). 86
5.14 The deviatoric capillary stress q_{cap} plotted as function of the mean capillary stress p_{cap} for different particle size distributions. 87
5.15 The deviatoric capillary stress q_{cap} plotted as function of the mean capillary stress p_{cap} for different particle size distributions. 88
5.16 Mohr-Coulomb envelops of dry materials for $p_p = 0.3, 0.5$ and 0.7 ($r = 0.5$) 89

5.17 Mohr-Coulomb envelops of dry materials for $r = 0.3, 0.5$ and 0.7 ($p_p = 0.5$) 90
5.18 Mohr-Coulomb envelop plotted in (p_{cont}, q_{cont}) for a sample with $r = 0.3, 0.5, 0.7$ and $p_p = 0.5$ 92
5.19 Mohr-Coulomb envelop plotted in (p_{cont}, q_{cont}) for a sample with $r = 0.5$ and $p_p = 0.3, 0.5, 0.7$ 93
5.20 Mohr-Coulomb envelop plotted in (p_{cont}, q_{cont}) for a sample with $r = 0.3$ and $p_p = 0.3$ 94

6.1 Definition of the pore network generated by regular triangulation in 3D and 2D 96
6.2 2D cut from the sample during the drainage process ($S_r = 0.23$). 99
6.3 Two phase fluid pressure and the interfacial tension on the solid phase. . . . 100
6.4 Menisci formed only along dry facets. 102
6.5 Simplified scheme for the addition of the meniscii in the case of connected and disconnected phases. 103
6.6 The water retention curves for both dense and loose packings in the case of connected (C) and disconnected phases (DC). 106
6.7 The evolution of the normalized number of menisci ($\overline{N_m} = N_m/N_{cont}$) with the suction and the saturation. 107
6.8 The capillary stress components during the drainage process. 107
6.9 The probability density functions of the number of the menisci as function of the distance (a) in the case of connected and disconnected phases and (b) in the case of dense and loose packing. 109
6.10 The stresses (capillary,funicular and total stresses) evolution during the drainage process in the case of connected phases. 111
6.11 The stresses (capillary,funicular and total stresses) evolution during the drainage process in the case of disconnected phases. 111
6.12 The evolution of strain with the capillary pressure during the drainage process for the dense packing in the case of connected and disconnected phases. 112
6.13 The evolution of strain with the capillary pressure during the drainage process for the loose packing in the case of connected and disconnected. 113
6.14 The variation of the effective stress parameter with the saturation for the dense packing in the case of connected and disconnected phases. 115
6.15 The variation of the effective stress parameter with the saturation for the loose packing in the case of connected and disconnected phases. 116

6.16 The loading unloading paths for dense and loose packings. 117

7.1 Illustration of a vertical well. 120
7.2 Sand movement and settling in slot flow experiment [38]. 122
7.3 The idealized study where proppant is discrete and rock formation is modeled as an elastic continuum. 124
7.4 A disc inclusion between two elastic semi infinite spaces (from [79]) 125
7.5 Separation at the elastic interface by tractions (from [80]) 126
7.6 Separation at the interface by equal concentrated forces (from [80]) 126
7.7 Results for the zone of separation at the interface for different disc thicknesses(from [79]) 127
7.8 Illustration of the model. 129
7.9 Illustration of the model during the simulation. 130
7.10 The rings that are taken into account in the estimation of b. 131
7.11 Evolution of the upper and lower contact zone radii during the simulation. . 131
7.12 The proppant compaction curve of the lower contact zone. 132
7.13 The proppant compaction curve of the upper contact zone. 133
7.14 The proppant compaction curve of the lower contact zone. 134
7.15 The global second order work and the kinetic energy versus the plate displacement.(from [20]) 135
7.16 The kinetic energy on the lower contact zone. 136
7.17 (a) Illustration of the square taken into account to calculate the stress distribution in the contact zone. (b) Stress value in different squares as function of the number of the particles inside the square. 137
7.18 Stress distribution on the lower plate in X and Y directions 138
7.19 (a)Stress distribution on the upper and lower zone for $Log(H_0/H) = 0.63$(c)Stress distribution on the upper and lower zone for $Log(H_0/H) = 1.17$ (e)Stress distribution on the upper and lower zone for $Log(H_0/H) = 1.44$ 139
7.20 The distribution of normal stresses on the compression plates used to compress a slab of a cohesive soil, and compared to PRANDTL distribution for an ideal metal. (from [45]) 140
7.21 The proppant compaction curves for different plate sliding friction. 141
7.22 The proppant compaction curves for various inter-granular friction angles. . 142

8.1 A disc inclusion between two elastic semi infinite spaces (from [79]). . . . 145
8.2 Illustration of the rock block with the defined dimensions. 145

8.3 Illustration of the model. 146
8.4 Illustration of the different stages of the disc inclusion simulation. 148
8.5 $(\sigma_z - \sigma_r)$ as function of the vertical strain. 149
8.6 The lateral strain as function of the vertical strain. 150
8.7 Illustration of the interface view of the rock block showing the rings considered to evaluate the stresses. 152
8.8 Stress distribution on the interface. 152
8.9 The validation of the numerical results: comparision with the analytic results of [79]. 153
8.10 Results for the zone of separation at the interface for different disc thicknesses(from [79]) 154
8.11 Illustration of the different stages of the deposition of the granular proppant. 156
8.12 Results for the evolution of b/a in the case of granular proppant compaction and comparison with the results in the case of disc inclusion. 158
8.13 Results for the evolution of Δ/a during the compaction of the proppant (disc shaped and granular pile). 159
8.14 Results for the the evolution of Δ/b during the compaction of the proppant(disc shaped and granular pile). 159
8.15 The evolution of $\Delta * a/D^2$ during the compaction of the proppant. 160
8.16 The evolution of $\Delta * b/D^2$ during the compaction of the proppant. 160

List of Tables

6.1 Particle size distribution of the granular sample 104

7.1 The initial deposited configuration of the pile of sand for different plate friction. 138

8.1 The values of the opening obtained from the stress distribution curve and from the ring method. 151

Chapter 1

Introduction

1.1 Introduction

The study of the behavior of granular materials is an interest to many, in soil and solid mechanics, in physics,... The importance of the interactions between the different particles in such materials and the complex phenomena that could be observed (segregation, flows, avalanches...), makes it insufficient to study them in the framework of continuum mechanics. New numerical tools based on discrete element methods (DEM) introduced by [18] are then developed and used since almost 40 years, to better understand these phenomena.

The discrete element method enables the simulation of grain assemblies in order to study how they behave under different conditions. It is based on the description of the local interactions between the particles of the granular sample.

Many applications however, requires more complex interactions law to study not only frictional dry granular materials but also cohesive materials, and coupled problems that involves interactions between grains and other elements such as partially or fully saturated granular materials that requires fluid-particles interaction law, particle-geogrid interaction, particle- structure (such as particle- rock interaction in the case of proppant compaction) ,....

DEM simulations are used in this thesis to study two problems in which coupling is a must.

The first problem embodies coupling between solid grains and fluids, and involves more understanding of the behavior of partially saturated granular materials in the pen-

dular regime, in which the presence of two non miscible fluids generates capillary cohesion mechanisms. The influence of this phenomenon on the macro behavior of granular materials is also studied. This approach enables not only to investigate the microscopic mechanisms in partially saturated materials, but also to discuss the concept of effective stress that is the question of continuous debates in the case of unsaturated soils.

The DEM model that is proposed in this thesis is an extension of the work of [74], and is limited to small amount of water content in which the wetting liquid phase is distributed in discontinuous way inside the pores (pendular regime). The model is also coupled with the model of [94] in order to simulate the full range of saturation.

The second problem embodies coupling between granular grains and continuum elastic structure to study the compaction of a proppant region that is a big interest in the hydrocarbon production industry. The resource production depends very much from the effective permeability of the rock formation. To increase the permeability of the rock formation, fractures are created in the formation by injecting fluids at very high pressure. Together with the fluids, proppants are injected to sustain these fractures open. The permeability is then very much dependent of the opening, extent and topography of the fractures that is itself dependent from the interaction between the proppant and rock formation.

This thesis structure is constituted of the following chapters after this introduction and state of the art.

The hydro-mechanical coupling problem in treated in 5 chapters:

Chapter 2 describes the micro-mechanical numerical model that is used and implemented in the open source DEM code Yade-DEM. All the assumptions that are made to establish the pendular law of interaction are also presented.

Chapter 3 is an energetical validation of the numerical model presented in chapter 2.

Chapter 4 discusses the concept of effective stress in partially saturated materials subjected to small deformation. The effective stress derived from the elastic energy and the contact stress obtained by averaging the local forces at contacts are compared. The efficiency of Love-Weber stress to describe the behavior of such materials is questioned.

In chapter 5 , The influence of roughness the grains and particle size distribution on the shear strength of partially saturated materials in pendular regime is presented, and the efficiency of Love-Weber to predict the rupture of unsaturated soils is questioned in this case.

In chapter 6, the pendular model is coupled with the model of [94] to simulate a complete drainage. The consequences of accounting for the pendular menisci on the deformation of the material and on the effective stress parameter are presented.

The grain-fracture wall interaction mechanism is discussed in 2 chapters:

In chapter 7, the compaction of a pile of proppant between two rigid plates is simulated and the stress induced by the compacted pile on the plates is investigated. The distance between the plates and the contact zone on each plate are related to the pressure applied on the pile.

In chapter 8, the rock formation is constructed by DEM and it is verified that DEM is able to simulate an elastic continuum by verifying analytic solutions developed in the case of rigid disc inclusion in [79]. In a second part, the rigid disc shaped proppant is replaced by a granular pile of proppant deposited by gravity and the geometry of the fracture is linked to the pressure applied on the elastic rock block.

1.2 Unsaturated soils

Unsaturated soils are the soils whose pores are filled by more than one fluid (water and air in the classical case or different liquid and gaseous fluids as it is the case for hydrocarbon reservoirs). Another definition has been given by [26] considering that unsaturated soils are the soils that have negative pore-water pressures.

In general, a granular soil is composed of three distinct phases: solid, liquid and gaseous.

- The solid phase which is constituted by soil grains of different shapes and sizes, and various mineral compositions.
- The liquid phase that can be adsorbed by the grains or not, and is composed in general of water that contains dissolved or trapped air.
- The gaseous phase that is a mix of air and water vapor. The main constituent remains the dry air.

We assume for sake of simplicity in the following that the pores are filled only by two immiscible phases: a wetting phase (w) and a non-wetting phase (n). The wetting and non wetting phases are identified through the contact angle which is the relative angle with the solid surface. The smallest angle corresponds to the wetting phase.

The proportions of water vapor and dissolved gas depends on the degree of saturation and the water pore pressure and influence the compressibility of both liquid and gaseous phases.

The degree of saturation S_r of a soil is the fraction of the volume of water on the volumes of the voids (The volume of the voids is the volume of the pores (total volume minus the volume of the solid phase)):

$$S_r = \frac{V_w}{V_v} \tag{1.1}$$

The different degrees of saturation in the soil allows to define different regimes(figure 1.1):

- Dry soil: the gaseous phase is the only phase that exists in the pores ($S_r = 0$).
- Hygroscopic regime: This regime occurs when the water is retained by the micro-pores or the asperities of the grains. This regime exists mainly in the case of clay. For sands, the amount of water retained by the asperities is negligible that we can consider that this regime does not exist.
- Pendular regime: When the amount of water becomes more important, the effect of the surface tension is remarkable and the grains are connected by discontinuous water bridges. The gaseous phase remains continuous in this case ($S_r < 7\%$).
- Funicular regime: When the amount of water is high enough to allow the fusion of the menisci, in such a way that the liquid phase becomes continuous and the gaseous phase becomes discontinuous, this is the funicular regime.
- Capillary regime: Before the total saturation of the soil, the liquid phase fills all the pores, and the gaseous phase exists only in the form of bubbles. This is what is called the capillary regime.
- Saturated regime: the gaseous phase disappears totally, and the liquid phase is the only phase that fills the pores ($S_r = 1$).

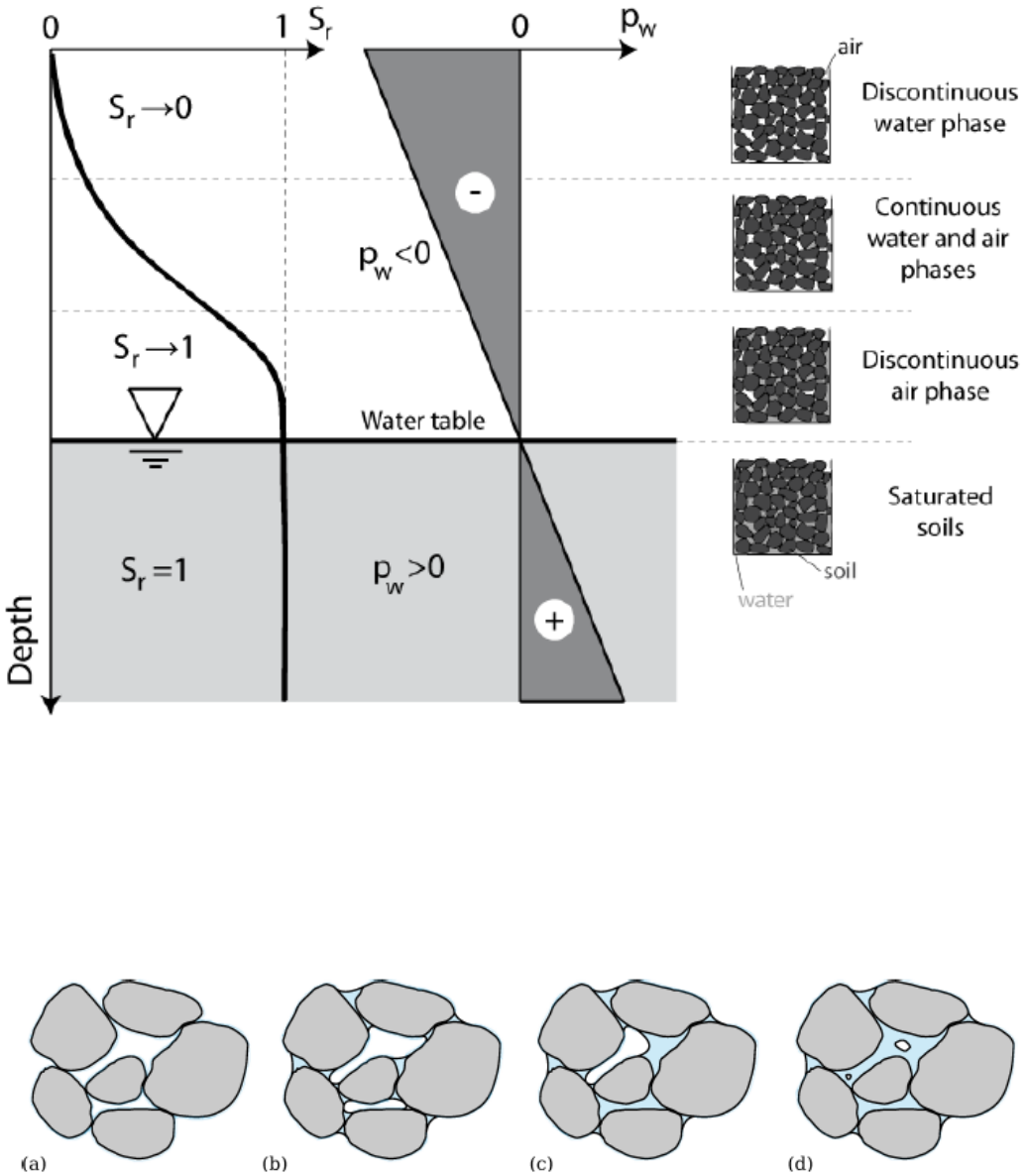

Figure 1.1 Illustration of different regimes of unsaturated soils

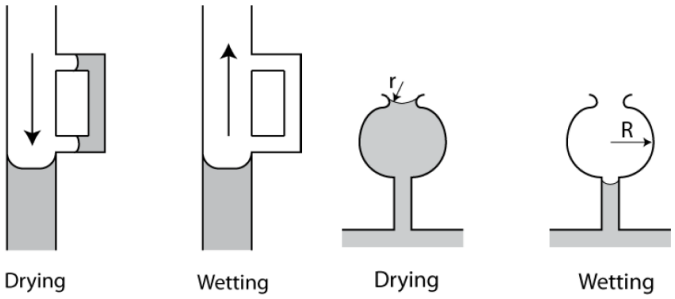

Figure 1.2 Patterns of drainage and imbibition for pores in parallel and in series

The pressure difference between the wetting and the non wetting phase is the matric suction ($p_c = p_n - p_w$). The matric suction for a given saturation is directly linked to the surface tension. The surface tension is a property of the contractile skin or the interface separating the wetting and non wetting phases that is a mixture of both liquids. This interface is purely elastic and can sustain tension [72]. This tension results from the equilibrium of forces, the molecules in the interface are subjected to unbalanced force due to the pressure difference between wetting and non wetting liquid, which generates a tensile force T_s to ensure equilibrium. The surface tension is the tensile force per unit of length (figure 1.3).

The matric suction is part of the total suction in the soil that is equal to the free energy of the water [1]. Another component is the osmotic suction that refers to the presence of salts in the water. Higher is the concentration of salts in the pore liquid, higher is the osmotic suction.

The matric suction is directly proportional to the relative humidity. That means that each value of suction corresponds to one value of relative humidity and hence to one value of water content. But experimental results for wetting and drying cycles for soil at constant net stress ($\sigma - p_n$) show that both curves are not the same. The drying curve is above the wetting curve (for the same value of suction, the water content in the case of drying is higher than the one in the case of wetting (figure 1.4)). These curves are called "soil water retention curves".

This phenomena is called capillary hysteresis, it is a characteristic of porous materials and can be explained as follows: The porous media is constituted of pores in parallel or in series. Young-Laplace equation implies that the suction is inversely proportional to the curvature of the pore. Higher the curvature, lower is the suction needed to dry a pore. In the case of the pores in parallel, the suction needed to dry the smallest pore is higher than the one needed to dry the big one. Then the big pore is dried while the water remains in the

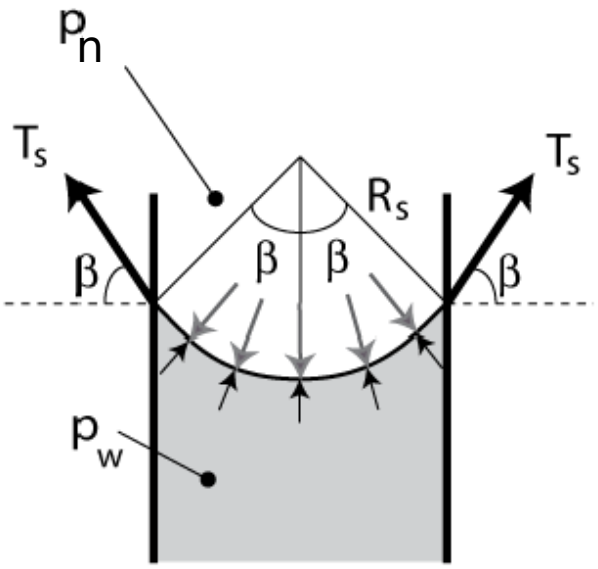

Figure 1.3 The surface tension

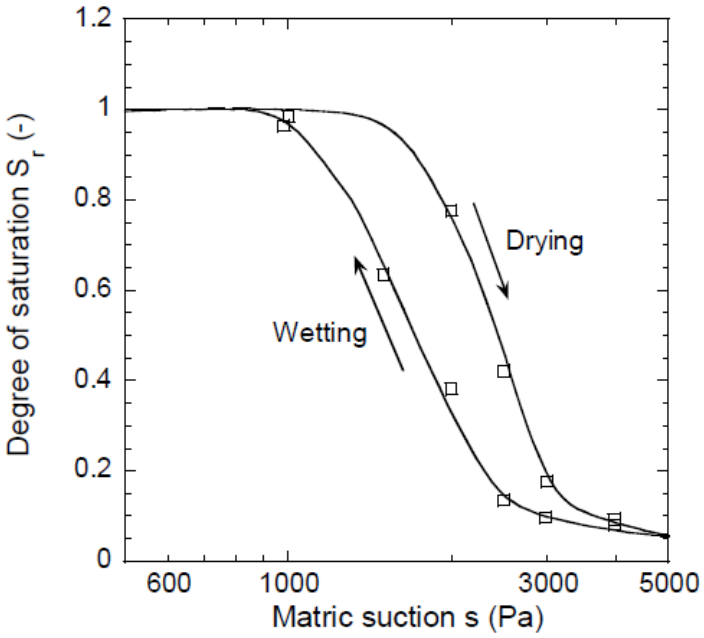

Figure 1.4 The water soil retention curves in a sand taken from [24]

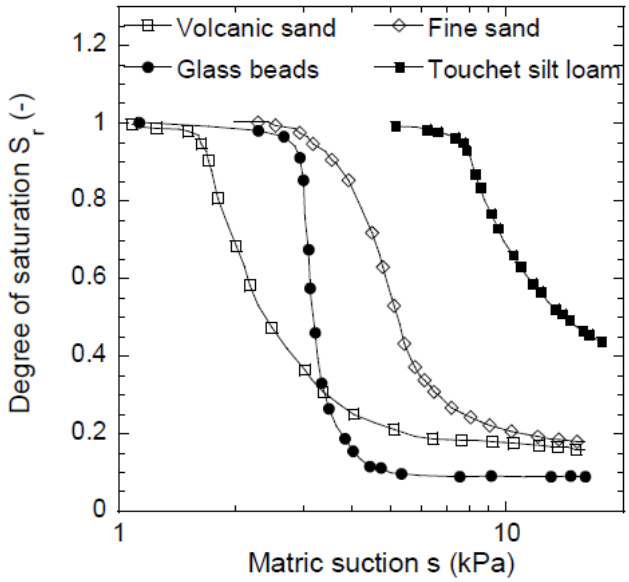

Figure 1.5 Water retention curves for various types of soil (from [12])

small pore (figure 1.2). In the case of imbibition for the same suction, the small pore is dry.

In the case of pores in series, different sizes of pores exist and the suction to dry a pore must be higher than the suction corresponding to the radius of the pore r in the case of drainage. In imbibition, the filling of the pore is controlled by the radius R.

The water retention curves and the capillary hysteresis are very much dependent from the type of soil, more precisely the granulometry that provides information on the size and type of soil grains (figure 1.5).

1.2.1 DEM modeling of wet granular media

In this section, the main previous models and results for the simulations of wet granular materials are presented.

The presence of the water in the sample is modeled by the addition of an attractive force between the grains. This capillary cohesive force is actually function of many parameters (suction, curvature and volume of the meniscus, particle size...). To solve the problem, several solutions have been proposed. Three main suggestions can be distinguished:

- The method that is used the most, is the toroidal approach where the meniscus is assumed to have the shape of a torus [28, 37].

- The second approach is the one based on the work of [49] where the capillary force is linked to the geometry of the meniscus
- The third approach is the one introduced by [74], in which the exact solution of Young-Laplace equation is presented. This work is and extension of the model of [74].

The main result obtained by the previous works , independently from the approach that is used is the increase of shear strength of the sample when the water is present. The presence of attractive forces at the local scale is transformed into a macroscopic cohesion.

The work of [70, 71] is remarkable on this side, where comparison were made between simulations and laboratory experiments on sand and glass beads. The cohesion increases with the increase of the water content [71] , while it has been proved that the friction angle remains constant (figure 1.6).

Some studies like [28, 74] were interested in the modeling of wetting collapse. [28] has put in evidence the micro structural causes of such phenomena and studied the influence of the meniscii on the stability of non saturated granular materials.

On the other hand, [23] was the first to present a water-retention curve from DEM simulations in monodisperse packings, and put in evidence the hysteresis linked to the creation and rupture of the menisci (figure 1.7).

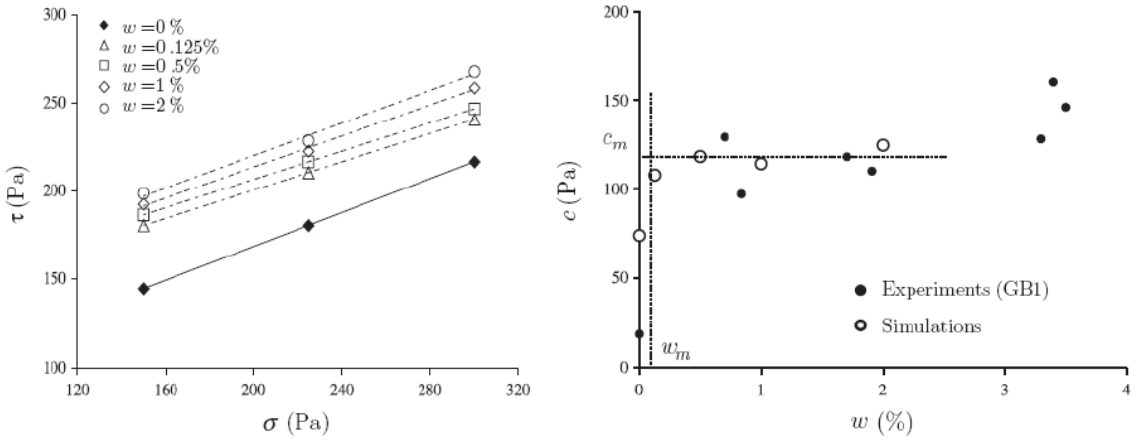

Figure 1.6 The Mohr Coulomb rupture envelop and the evolution of the cohesion with the water content from the work of [71]

These previous works have mainly focused on the simulation of smooth grains with tightly graded particle size distribution. The influence of the particle size distribution on the

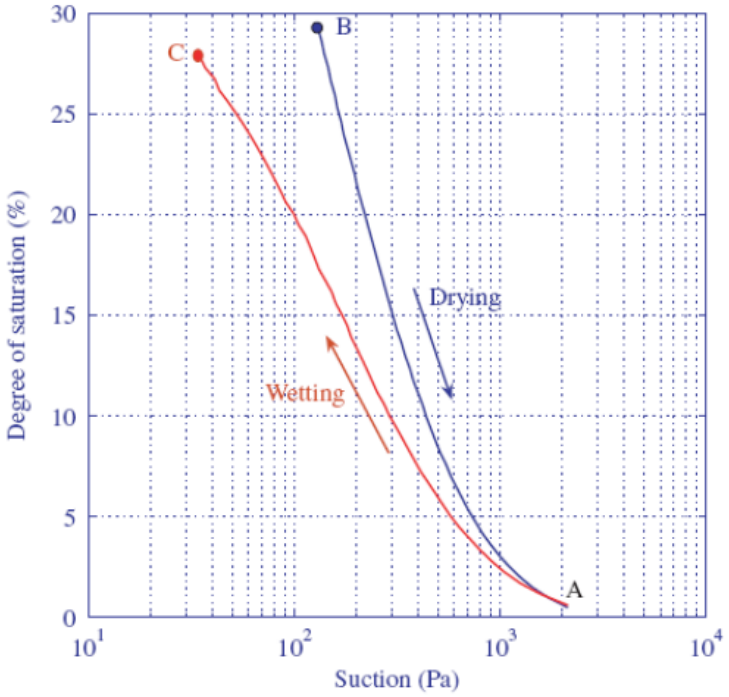

Figure 1.7 The retenstion curve presented by [23] by DEM.

mechanical behavior of soils has been mainly investigated in the case of fully dry materials [35, 56, 61–63, 77, 87]. The influence of the roughness on the capillary effects and the mechanical behavior in unsaturated conditions has been instead mainly introduced and studied for a two grains configuration [51, 55, 64]. Rough grains and particle size distribution effects on the mechanical behavior of unsaturated granular materials are also an interest of this study and will be discussed in chapter 5.

1.2.2 Effective stress concept in unsaturated soils

The concept of effective stress has been introduced by Terzaghi [86]. Terzaghi has defined the stress of a porous medium filled with a single fluid (fully dry or fully saturated). In the case of dry soil the effective stress is:

$$\sigma' ij = \sigma_{ij} \tag{1.2}$$

In the case of fully saturated soils, the effective stress was defined as follows:

- All measurable effects of a change of stress of the soil, that is compression, distortion,

change of shearing resistance, are exclusively due to changes in effective stress σ' .

- σ' is defined by:

$$\sigma'_{ij} = \sigma ij - p_w \delta_{ij} \tag{1.3}$$

p_w is the pore water pressure , δ_{ij} is the Kroenecker's delta that is equal to 1 when $i = j$ and 0 when $i \neq j$, and σij is the total external applied stress. This expression has been proved to be experimentally true.

Based on Terzaghi's definition, the stress state is only represented by the effective stress. The effective stress can be then defined as the stress depending on the strain of the skeleton. In elasticity:

$$\dot{\varepsilon}^e_{ij} = C^e_{ijkl} \dot{\sigma'}^e_{kl} \tag{1.4}$$

$\dot{\varepsilon}^e_{ij}$ is the rate of the elastic strain of the solid skeleton and C^e_{ijkl} is the drained elastic compliance matrix and $\dot{\sigma'}^e_{kl}$ the rate of change of the effective stress.

Since the introduction of this concept, it has been widely used in geotechnical engineering applications.

The water in nature does not exist only in fully saturated state. The concept of effective stress must be then extended to unsaturated conditions. The work of [8] has extended the work of [86] to define effective stress as the excess of total stress over an equivalent pore pressure proportional to the matric suction $p_c = p_n - p_w$:

$$\sigma'_{ij} = (\sigma_{ij} - p_n \delta_{ij}) - \chi p_c \delta_{ij} \tag{1.5}$$

where $(\sigma_{ij} - p_n \delta_{ij})$ is the total net stress and χ the so-called effective stress parameter.

χ covers all the range of saturation and varies from 0 when the material is dry to 1 when it is fully saturated. χ was proposed to be equal to the degree of saturation by [8] and [76].

Some studies has verified the χ parameter experimentally [7, 8, 36, 95]. The experiments show evidence that the assumption of Bishop ($\chi = S_r$) is not true and the uniqueness of relationships between χ and S_r have been questioned (figure 1.8). This has been also verified by analytical averaging [31, 90].

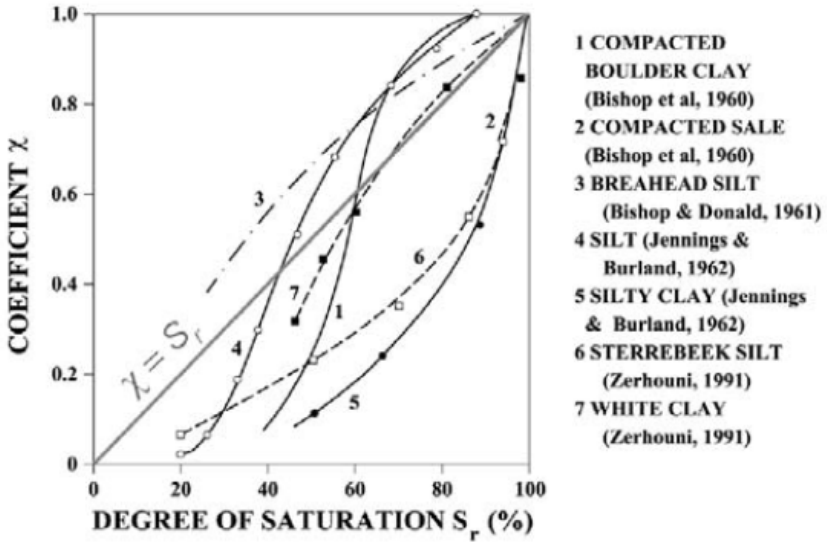

Figure 1.8 The effective stress parameter versus the degree of saturation from [95]

Since then, many authors tried to express χ in different ways that are more complex. Among the formulations we cite the one presented by [39]:

$$\chi = \frac{p_c}{p_c^e} \qquad if \quad p_c > p_c^e \qquad else \quad \chi = 1 \tag{1.6}$$

p_c^e is the air entry pressure.

Limitations of the effective stress concept

Before the 90's, the effective stress formulation for unsaturated soils was limited to elastic conception. This limitation has raised many questions on the validity of this concept for unsaturated soils. The validity of the formulation presented by [8] was criticized [36], considering that it does not allow the explanation of the collapse phenomenon in unsaturated granular materials. The fully reversible elastic concept is then not enough. A complete elastic plastic framework is then developed afterwards.

In addition, it has been shown by [39] that there isn't any single relationship between the effective stress parameter χ and the degree of saturation. To overcome these difficulties, the use two independent stress variables was proposed [9, 10]. But It is shown by [92] that the mechanical variables are not enough to describe the behavior of unsaturated soils, but it is important to consider the structure change of the soil as well. In fact, the limitation

of the single effective stress in the study of the strength and deformation behavior is that it is considered as the only and exclusive control variable. All the other factors related to the micro structure of the soils, environmental and geological conditions,... are either neglected or involved in the parameters rather than being considered independent variables, which is not sufficient in unsaturated conditions, where comes the importance of other stress frameworks.

Other stress frameworks

In order to build a proper stress framework, other frameworks have been proposed.

Works like [10, 92] have proposed to use unified forms of Bishop's type effective stress combined with another stress variable (the suction). But these variables also do not govern all the factors that influence the behavior of unsaturated granular materials.

The thermodynamic approaches is another approach which incorporate also the effects of the interfaces separating the phases that are present in unsaturated materials [19, 30, 33, 57, 58, 58] . The advantage of these proposed stress framework is including the interfaces energy based on the knowledge of the water retention curve and simplifying the modeling of bonding. As a consequence, the hydraulic hysteresis is put in evidence naturally in the effective stress. In the thermodynamic approach the environmental factors such as temperature, PH, salinity are also taken into account naturally.

[19] is one of the works who considered interfacial effects in the free energy of the skeleton and wrote the effective stress as the following:

$$\sigma'_{ij} = \sigma_{ij} - p_n \delta_{ij} + \pi_{ij} \tag{1.7}$$

where π_{ij} is the equivalent pore pressure defined as:

$$\pi_{ij} = S_r p_c \delta_{ij} - \eta \frac{\partial E_{cap}}{\partial \varepsilon_{ij}} \tag{1.8}$$

E_{cap} being the term associated the energy of the interfaces, η refers to porosity.

In [30] and [33] authors have also proposed Bishop's type equation including interfacial effects. The work of [33] does not agree with the experimental data because of the lack of proper hydro-mechanical coupling, while the work of [30] lacks accounting for bonding effects.

In [58] and [57] a new equation for the effective stress tensor is presented including the energy of the interfaces and assuming that the wetting-non wetting interface changes with

the deformation, while the others remain constant in the case of rigid grains. This hypothesis is questioned later on. The formula suggested by [57] is:

$$\sigma' = (\sigma - p_n I) + S_r p_c I - a_{wn}\Gamma_{wn}\frac{\partial U_{wn}}{\partial \varepsilon} I \tag{1.9}$$

where Γ_{wn} is the interface mass density, U_{wn} the free energy density of the wetting-non wetting interface and a_{wn} the amount of the wetting-non wetting interface.

The work of [57] also introduced the $p_c - a_{wn} - S_r$ curve. The projection of this curve on the $p_c - S_r$ plane gives the collection of all $p_c - S_r$ curves (primary, main, scanning, etc.).

The validity of the formula suggested by [57] is compared to the experimental results of [40] and others and the results seem to fit quite well. However the amount of interfaces was not measured experimentally but calculated by fitting the drying and wetting experimental data of the soils. The formula was not validated in the pendular regime (figure 1.9).

There is still a lack in the measurement of the interfaces experimentally in order to validate these formulas.

In DEM simulations, the effective stress is defined by many authors [28, 37, 71, 74] as the averaged contact stress initially introduced for dry granular media by [16, 42, 48, 91]. This stress was found in [75] to follow a unique Coulomb's friction criterion for the dry case or in unsaturated/saturated conditions at the peak for shear strength.

However, the context of peak shear strength must not be forgotten and this averaged contact stress based on Love-Weber formula should be tested for other aspects of the mechanical response.

1.3 Compaction of proppant region.

Hydraulic fracturing is a technique that consists on fracturing rock formation by a pressurized liquid. It is mainly used to improve the process of energy production. The injection of pressurized liquid creates cracks and fractures in the rock formations. The creation of a fracture will provide a conduit for the transport of the resource provided the fracture can be maintained in an open condition. But those created fractures underground will close if there wasn't anything to keep them "propped" open. The procedure that is used to accomplish this objective is to introduce a mixture of granular materials with the fracturing fluids which will accumulate at the fracture zone and increase the permeability of the rock formation and facilitate the extraction of hydrocarbons. This granular mixture (proppants) can vary from

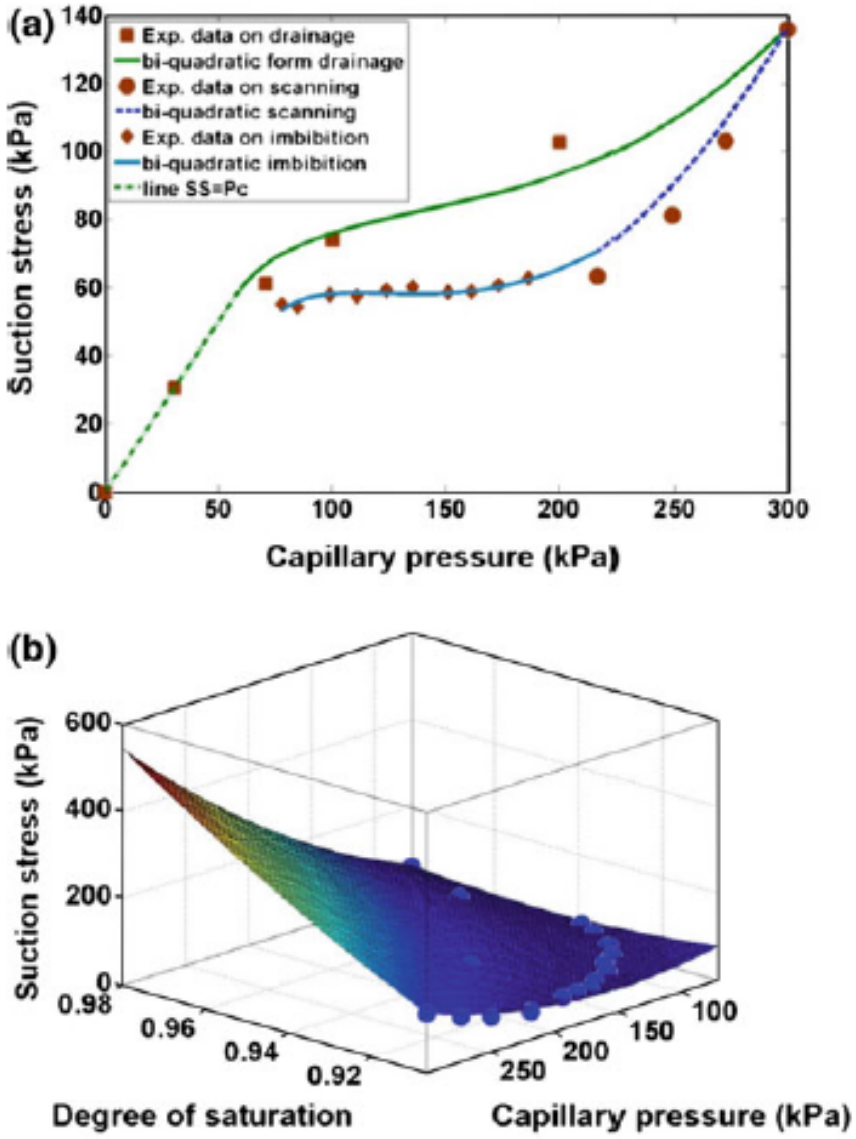

Figure 1.9 (a) 2D plot of the wetting and drying paths and (b) 3D plot of suction stress for Buffalo dam clay (the experimental data is from [40]). The figure is from [58]

sand to manufactured polymer beads that can be coated with resins,... The proppants play an important role in the energy industry because without proppants oil and/or gas production from shales would not be feasible.

When the pressures exerted by the fracturing fluids are reduced to the value present in the geofluids, the geostatic stresses will induce closure of the fracture and the proppant is expected to maintain the fracture in an open condition. The opening of the fracture will increase its fluid conductivity of the fracture and thus permit easier extraction of the resource.

When fluid pressure is applied to a pre-fractured interface, the zone of separation will be finite provided the pressurization is applied over a finite region and the total load is finite. In other words, the pressurization of the pre-fractured medium cannot occupy an infinite extent.

The effective permeabilities of the fractures can be then determined as a function of this finite fracture opening. The deformed fracture configuration is related to the elasticity characteristics of the rock formation domains and the primary properties of the proppant, including particle size distribution, elasticity of particles, interface frictional characteristics....

Hence it is very important to examine the mechanics of the interaction between the granular proppant region and the "elastic domains" that contribute to compression of the proppant and determine the final configuration of the proppant region and the deformed shape of the fracture in terms of extent and aperture.

This problem has been an interest in many studies, mainly analytic results [78–80]. These analytic solutions has been developed as function of the elastic domain properties in the case of rigid shaped inclusion or a specific force distribution. All these studies lack the real stress distribution induced by a granular proppant on the rock formation, which might change significantly the fracture shape and the fracture extent. The particle-fracture wall interaction to determine the stress ditribution induced by the particles on the wall and the geometry of the fracture is the main interest of this study.

Chapter 2

DEM modelling of unsaturated soils

2.1 Introduction

This chapter is devoted to the description of the numerical model that has been inspired by the work of [75] and re-implemented in the open source code YADE. The model aims to simulate a three-phase granular matter in the pendular regime (limited to low saturations that do not exceed 5 percent).

The final algorithm is detailed. In the pendular regime disconnected water bridges are formed between soil particles. The geometry of the bridges including all the interfaces that are present in the sample, and the forces applied on the particles are calculated based on the assumptions made in the model. The influence of the roughness of the grains on the capillary forces is discussed, and finally the limitations of the model are presented.

2.2 Discrete element method

The numerical modeling that is based on the discrete element method is very efficient to study the influence of the local interactions and phenomena on macroscale behavior of granular materials.

This method consists on integrating movement of the grains and are divided into two main families:

- The non smooth DEM approach that treats particles as rigid bodies and does not allow deformation in the contact region of the particles. This approach is based on the contact dynamics method introduced by [53]. The interactions in this case are

described as collisions. The resolution of the problem is based on an implicit scheme for the dynamics equations and the inter-granular relations.

- The smooth-DEM approach that accounts for the deformability of the grains.

  The smooth-DEM are based on molecular dynamic (MD) approach. This was initiated by [18]. In this method the interactions between the grains are explicitely presented as function of the relative displacement, using simplified interaction laws. This approach is more general and easier to implement.
  YADE (Yet Another Dynamic Engine), the open source C++ framework that is used for developments and simulations in this study is based on this approach. It allows the development of three dimensional numerical models. The open source licensing allows the contribution of the users and development of their own models.

2.2.1 Computational cycle

A DEM simulation is started by first generating a model, which results in spatially positioning all particles and assigning initial velocities. The forces which act on each particle are computed from the initial data and the relevant physical laws and contact models.

The method consists in two main steps: the computation of the grains positions and the computation of the forces. At each time step, knowing the position, orientation and shape of the grains, the interaction list is defined. In the case of dry granular medium made of spheres, two spheres interact when the distance separating their centers is less than the sum of their radii. The forces acting on the particles once identified by the interaction laws, the forces are applied on the grains and the new positions of the grains are identified.

If the grain motion in an oriented space of two or three dimensions (i=1,2 or 1,2,3) is characterized by its position x_i, its translational and rotational velocities $\dot{x}_i$ and $\dot{\omega}_i$, the translational and rotational velocities follow Newton's second law of motion:

$$\ddot{x}_i = F_i/m \tag{2.1}$$

$$\ddot{\omega}_i = M_i/J_i \tag{2.2}$$

where m is the mass of the particle, J its moment of inertia and F_i and M_i the forces and moments applied on the particle.

The evolution of the whole system is computed by updating the positions of the grains at each time step Δt. The velocities of the grains are calculated by integrating the accelerations

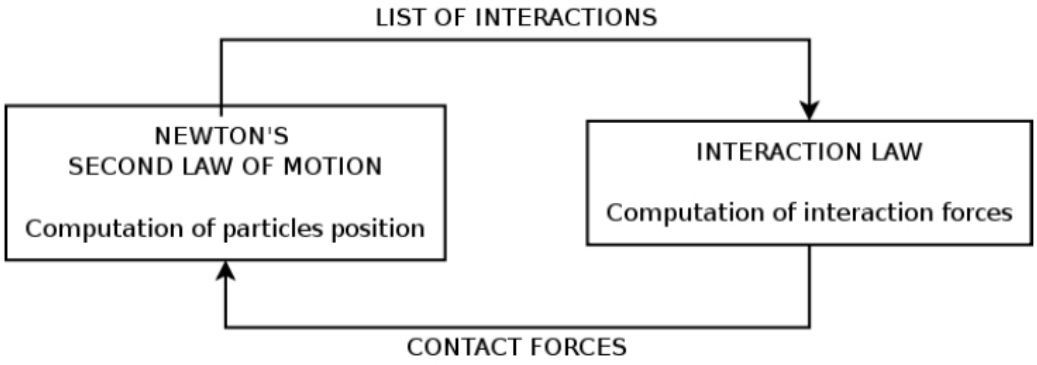

Figure 2.1 Computational cycle of a DEM model.

according to a second-order centered finite difference scheme at $[t+\Delta t/2]$:

$$\dot{x}_i^{[t+\Delta t/2]} = \dot{x}_i^{[t-\Delta t/2]} + \ddot{x}_i^{[t]}\Delta t \tag{2.3}$$

$$\dot{\omega}_i^{[t+\Delta t/2]} = \dot{\omega}_i^{[t-\Delta t/2]} + \ddot{\omega}_i^{[t]}\Delta t \tag{2.4}$$

The positions of the grains at $[t+\Delta t]$ are then determined by integrating the translational velocity:

$$x_i^{[t+\Delta t]} = x_i^{[t} + \dot{x}_i^{[t+\Delta t/2]}\Delta t \tag{2.5}$$

After determining the positions of all the particles at $[t+\Delta t]$, the list of interactions is updated and the new interaction forces are recomputed.

2.2.2 Interaction law

The contact law is the cornerstone of DEM, as it dictates the local and global behavior of an assembly.

Each contact in the assembly is defined by normal and tangential stiffnesses and an inter-granular friction angle ϕ_c (figure 2.2).

The action of one grain on the other in the assembly is defined by an interaction force and a moment. The contact force can be divided into a normal and a tangential force by considering the plane that is tangent to the grain.

For two grains in interaction, we assume that the relation between the contact force

and the relative displacement is linear elastic-plastic. The normal component of the contact force F_n is related to the normal relative displacement u between the grains by the normal stiffness k_n, and the tangential component of the force F_t is related to the relative tangential displacement v by the tangential stiffness k_t (figure 2.3).

The normal and tangential stiffnesses are proportional to the size of the grains. The normal stiffness k_n is then defined as a function of a global young modulus E_{global} introduced by the user and the harmonic mean of interacting spheres radii R_1 and R_2.

$$k_n = 2E_{global} * \frac{R_1 R_2}{R_1 + R_2} \tag{2.6}$$

The intoduction of E_{global} allows the homogenization of the elastic behavior at the scale of an assembly, and ensure the independence of their global stiffness with the size of the particles.

The shear stiffness k_t is related to the normal stiffness through a coefficient α such as:

$$k_t = \alpha k_n \tag{2.7}$$

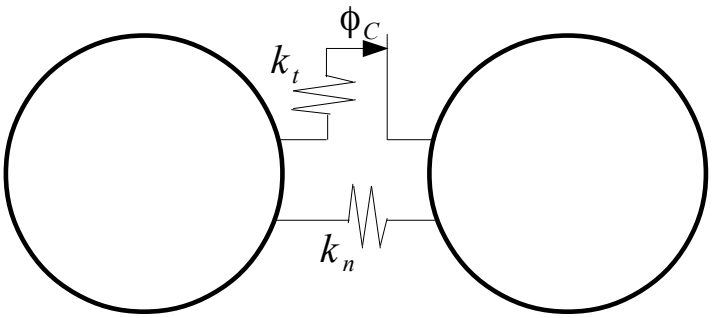

Figure 2.2 Contact variables: stiffnesses and friction angle

Note that E_{global} defined in the code is proportional to the Young modulus of an assembly of particles, but it is not the same. The Young modulus of an assembly must be calculated by subjecting the packing to elastic deformation. α is proportional to the Poisson's ratio of the assembly.

The normal force acting on the particles in interaction is:

$$F_n = k_n u \qquad if u \leq 0, \qquad else \qquad F_n = 0 \tag{2.8}$$

The increment of tangential force is given as:

$$\Delta F_t = k_t \Delta v \tag{2.9}$$

The interaction between the particles follows Coulomb friction law, then the tangential force is limited to a maximum absolute value of $\mid F_t \mid \leq F_n \quad tan\phi_c$ (figure 2.3).

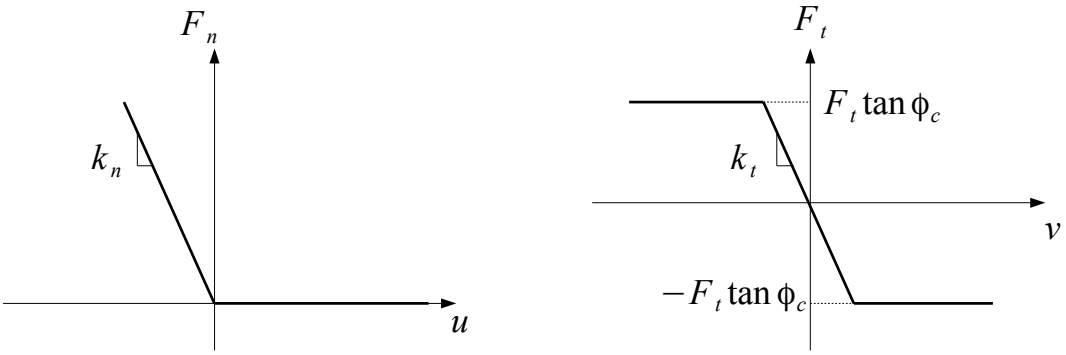

(a) (b)

Figure 2.3 Elastic contact law for normal interaction and elastic-plastic tangential interaction.

The elastic energy of contact is defined as:

$$E_{el} = 0.5 k_n u^2 + 0.5 k_t v^2 \qquad if u < 0 \qquad else \qquad E_{el} = 0 \tag{2.10}$$

An inter-granular adhesion can be also added to the contact law. The simplist case is that this cohesion generates a normal resistance to the traction when the grains are in contact.

2.2.3 Critical time step

The stability of an oscillating spring-mass system is function of the natural period of the system. This period is determined at each iteration for all the degrees of freedom for each

particle. It is expressed as:

$$T = \sqrt{m_i / K_i^j} \tag{2.11}$$

where m_i is the mass of the particle i and K_i^j an equivalent stiffness that is evaluated considering all the contacts of one particle for each degree of freedom j.

The critical time step is the smallest obtained value:

$$\Delta t_{cr} = min(i, j)(\sqrt{m_i / K_i^j}) \tag{2.12}$$

2.3 Numerical model: the pendular model

2.3.1 Assumptions for the numerical model

At low saturations, menisci are formed between particles and the regime is called pendular. The additional capillary force acting on the spheres can be linked to the geometry of the grains and to the capillary pressure inside the medium. The shape of the meniscus is determined by Young Laplace equation that relates the curvature of the bridge C to the capillary pressure p_c through the surface tension acting on the wetting/ non-wetting interface.

$$p_c = \gamma_{wn} C \tag{2.13}$$

Young-Laplace equation, even if it seems simple, is very difficult to solve. To simplify the problem, several assumptions are made:

- The bridges are formed between stiff spherical particles in perfect wetting conditions (wetting angle=0).
- The effect of the gravity is not taken into account, hence the form of the bridge is axisymmetric since the gravity forces do not alter its shape. This has been proved to be realistic by [65] if the bond number is much smaller than 1.

$$B_0 = \frac{L^2 \Delta \rho g}{\gamma_{wn}} << 1 \tag{2.14}$$

[74] has shown that if the wetting liquid is water, for assemblies of mean grain radii of 1 mm, the bond number is equal to 0.13. The effect of the surface tension dominates the effect of the gravity and the results of the simulations are realistic.

- The simulations are performed in quasi-static conditions, the viscous effects of the fluid is negligible. To satisfy this condition, the capillary number introduced by [49] must be smaller than 10^{-3} [25]

$$C_a = \frac{\nu \vartheta}{\gamma_{wn}} < 10^{-3} \tag{2.15}$$

  where ν is the viscosity of the wetting liquid, ϑ is the relative velocity of the grains.

One of the originalities of this model is that it takes into account the roughness of the grains to simulate the behaviour of the liquid with irregular grain surfaces. The effect of the roughness on the capillary force is in direct relationship with the water volume of the menisci [2].

- If the volume of water is quite small, only several micro-capillary bridges form between the asperities. This regime is called asperity regime in which the roughness has a great impact on the capillary force. This should not be mistaken with the hygroscopic regime in which the water is adsorbed; in this case the amount of water is quite small with respect to the asperities size that it does not allow to form one single meniscus connecting the grains. This case is mainly studied in the case of micro/nanoscale roughness, as it is of great importance in the study of fine powders behavior and in technology of micro/nanoelectro mechanical systems [68, 88, 89].

- For higher water volumes, one meniscus connects the particles, but the volume of the wetting liquid is still not very high to neglect the effect of the asperities surrounding the grain, the capillary force is proportional to the volume of water, and the regime is called roughness regime.

- Finally, when the volume of water is high enough to neglect the size of the asperities of the grains, we have the spherical regime. In this case, if the particles are in contact, the capillary force becomes almost independent of the volume of the menisci. However, in this case, if the grains are not perfectly spherical (macro irregular asperities or grains with plane surfaces) the effect of the roughness is still visible even for high volumes of liquid. It all depends on the relation volume of water-size of the asperities/shape of the grains.

- The numerical model developed by the author is valid for the roughness and spherical regimes.

The different roughness regimes and the dependency of the capillary force on the volume for the different regimes are presented in figure 2.4.

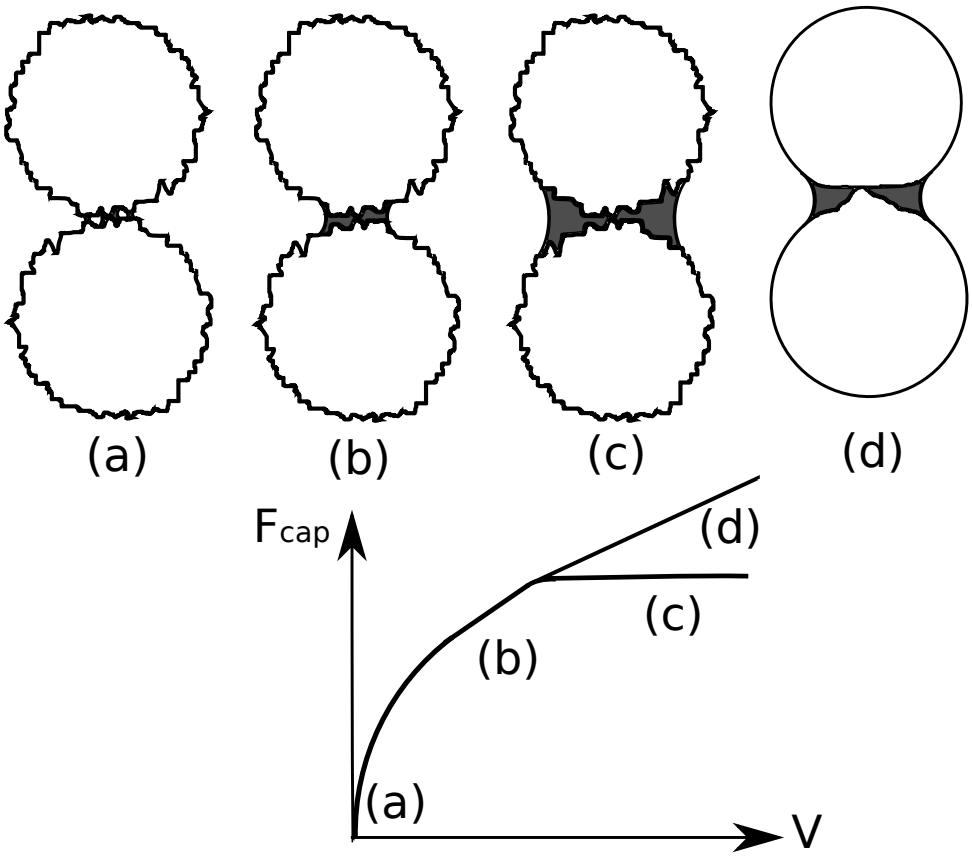

Figure 2.4 Illustration of different roughness regimes and the dependency of the capillary law on the volume of the wetting liquid.

2.3.2 Young-Laplace equation

We consider two stiff spherical particles of radii R and r respectively, connected by a liquid bridge in perfect wetting conditions. R is the radius of the bigger grain (figure 2.5). The shape of the bridge is determined by Young-Laplace equation that relates the curvature of the bridge C to the capillary pressure p_c through the surface tension.

$$p_c = \gamma_{wn} C \tag{2.16}$$

or a dimensionless form

$$p_c^* = C^* \tag{2.17}$$

with $C^* = CR$, and $p_c^* = \frac{p_c R}{\gamma_{wn}}$

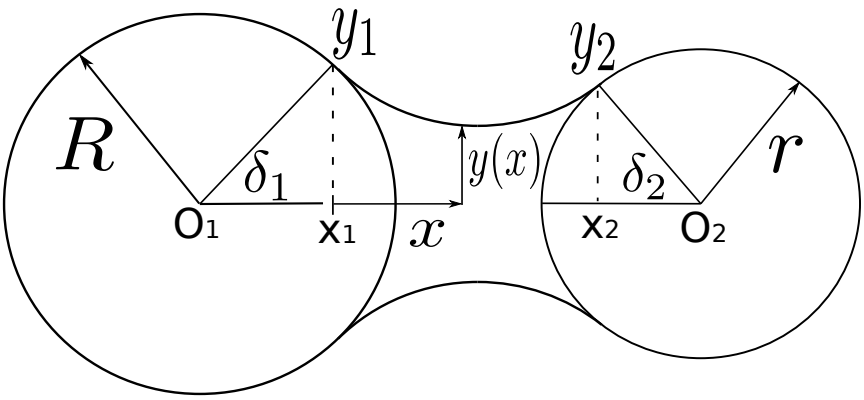

Figure 2.5 Illustration of a liquid bridge connecting two particles.

In the case of spherical grains and in axisymmetric conditions, the curvature of the bridge is defined as:

$$C^* = \frac{-1}{Ry^*\sqrt{1+y'^{*2}}} + \frac{y''^*}{R(1+y'^{*2})^{\frac{3}{2}}} \tag{2.18}$$

$y^* = y^*(x^*)$ defines the profile of the bridge.

with $x^* = x/R$, $y^* = y/R$.

Replacing C in equation (2.17), and rearranging yields:

$$p_c^* y^* + \frac{(1+y'^{*2}) - y^* y''^*}{(1+y'^{*2})^{\frac{3}{2}}} = 0 \tag{2.19}$$

The capillary force a is constant function of x and can be calculated at any section for any value of x and is given by:

$$F_{cap}^* = \frac{F_{cap}}{\gamma_{wn} R} = \pi p_c^* y^{*2} + \frac{2\pi y^*}{\sqrt{1+y'^{*2}}} \tag{2.20}$$

Note that the capillary force is only a normal force: [84] and [70] have proved experimentally that the inter-granular coefficient of friction is independent of the presence of the water. The capillary effect is not then introduced in the frictional tangential law.

It can be also verified that calculating $\frac{dF_{cap}}{dx}$, knowing that $y = y(x)$, yields to equation 2.19.

This equation is a first order differential equation that can be written as:

$$y'^{*} = \sqrt{\frac{y^{*}}{2\pi F^{*}_{cap} + p^{*}_{c} y^{*2}} - 1} \tag{2.21}$$

Solving equation (2.21) allows to calculate also the values of the geometric properties of the meniscus. The equation is solved numerically using Runge-Kutta 4 method, and the boundary conditions are determined by the filling angles δ_1 *and* δ_2.

$$y^{*}_{1} = sin(\delta_1) \tag{2.22}$$

$$y^{*}_{2} = \frac{r}{R} sin(\delta_2) \tag{2.23}$$

$$y^{'*}_{1} = -arctan(\frac{\pi}{2} - \delta_1) \tag{2.24}$$

$$y^{'*}_{2} = arctan(\frac{\pi}{2} - \delta_2) \tag{2.25}$$

y_1 and y_2 are the initial and the final components of the profile of the bridge.

The volume of the meniscus is:

$$V^{*} = \frac{V}{R^3} = \int_{x_1}^{x_2} \pi y^{*2} dx^{*} - V^{*}_{1} - V^{*}_{2} \tag{2.26}$$

V^{*}_{1} *and* V^{*}_{2} are the normalized volumes of the spherical caps covered respectively by the filling angles δ_1 *and* δ_2

The wetting-non wetting interface is (figure 2.6):

$$A^{*}_{wn} = \frac{A_{wn}}{R^2} = \int_{x_1}^{x_2} 2\pi y^{*} \sqrt{1 + y'^{*2} dx^{*}} \tag{2.27}$$

The solid-wetting interface is (figure 2.6):

$$A^{*}_{sw} = \frac{A_{sw}}{R^2} = 2\pi(\frac{r}{R})^2(1 - cos(\delta_2)) + 2\pi * 1^2(1 - cos(\delta_1)) \tag{2.28}$$

The solid-non wetting interface is (figure 2.6):

$$A^{*}_{sn} = \frac{A_{sn}}{R^2} = 2\pi(\frac{r}{R})^2(1 + cos(\delta_2)) + 2\pi * 1^2(1 + cos(\delta_1)) \tag{2.29}$$

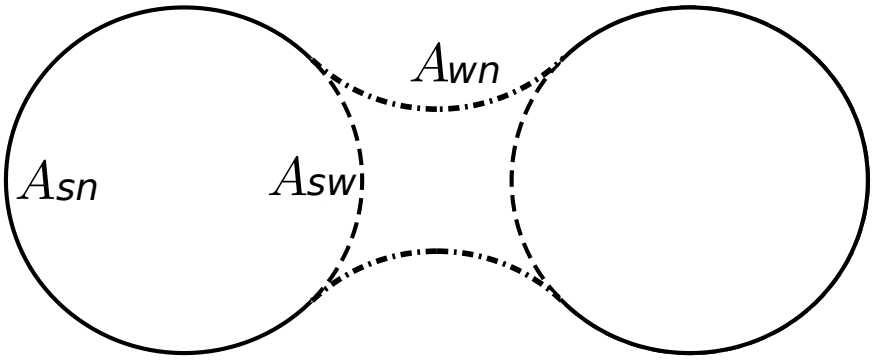

Figure 2.6 Illustration of the three interfaces.

The inter-granular distance is calculated using the positions and the radii of the grains:

$$D^* = \frac{D}{R} = \frac{O_1O_2}{R} - 1 - \frac{r}{R} \tag{2.30}$$

Plotting the variables (F^*_{cap},V^* and δ_1) as function of the inter-granular distance D^* for various values of capillary pressure, we notice that it is possible to have two different solutions of Laplace-Young equation for the same inter-granular distance (figure 2.7).

Only one solution is stable for each value of D^* and it corresponds to the minimum value of the energy of interfaces present in the system. The total interfacial energy for two grains connected by a water bridge is:

$$E^*_{cap} = \gamma_{wn}(A^*_{wn} - A^*_{sw}) \tag{2.31}$$

Further details on the calculation of the energy of interfaces are given later in chapter 3 section 3.2.2.

Figure 2.8 shows the possible solutions of the energy of the interfaces as function of the inter-granular distance for different values of suction. The stable solutions corresponds to the minimum energy of interfaces. Hence the set of stable solutions for the same suction values is plotted in figure 2.9. These are the solutions implemented in the capillary law in YADE.

Both stable and unstable solutions converge to the same value at the maximum possible inter-granular distance for which there is still a bridge. This is the rupture distance of the bridge D_{rupt} that is determined automatically when there is no possible physical solution for Laplace equation.

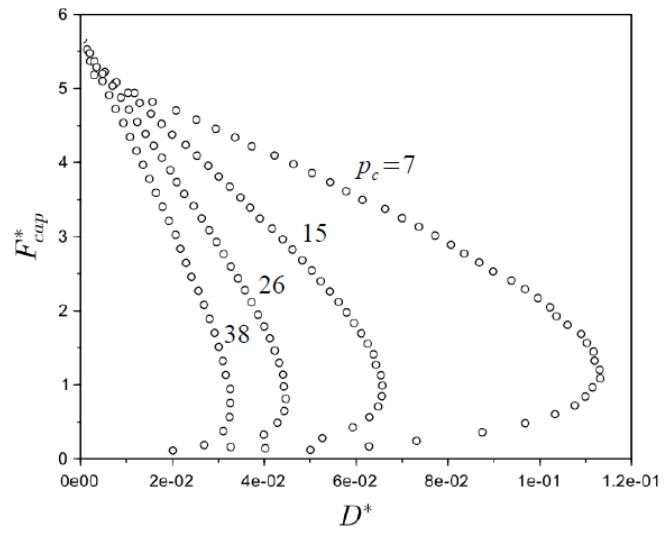

(a)

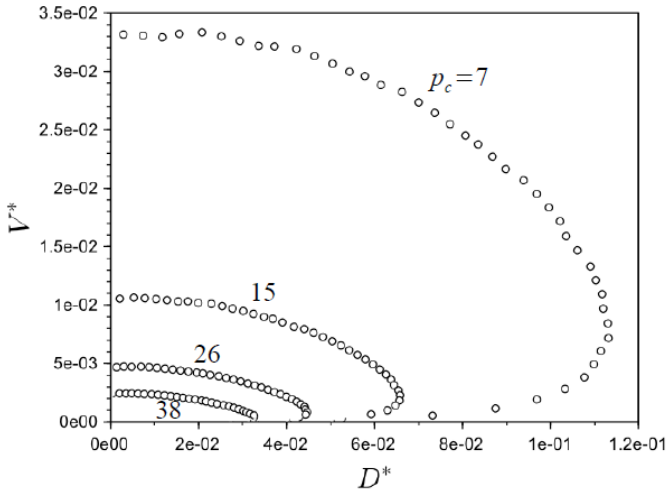

(b)

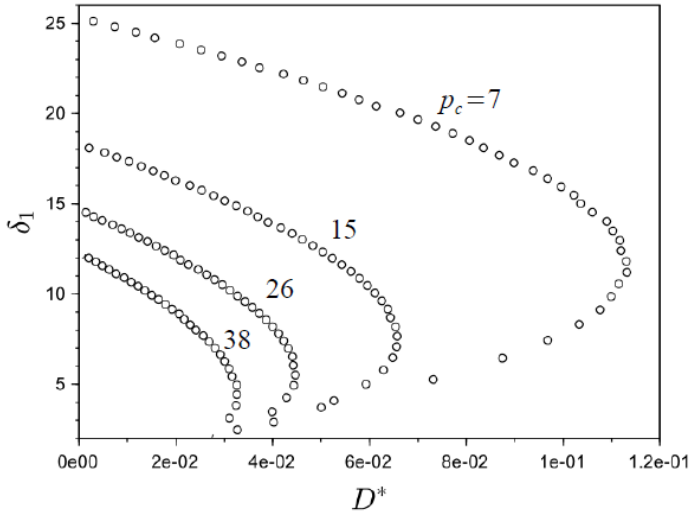

(c)

Figure 2.7 Output variables of Young-Laplace equations for different suction values.

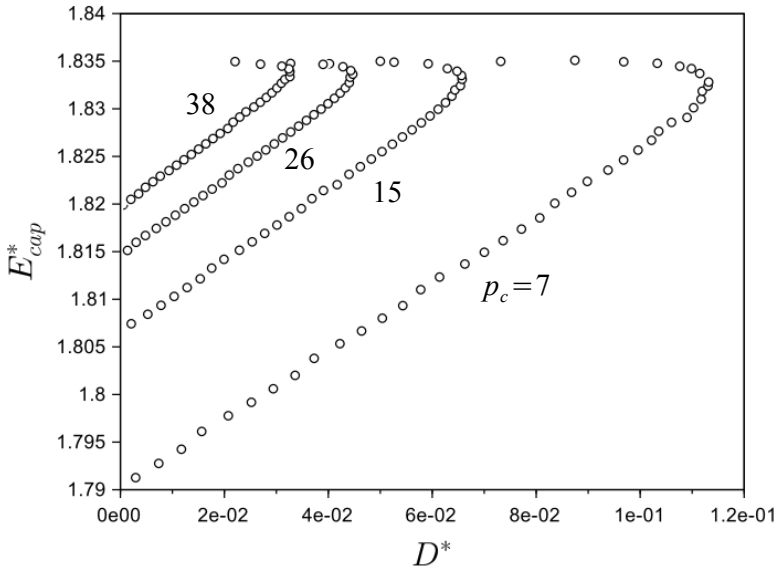

Figure 2.8 The energy of interfaces corresponding to the solutions of Laplace-Young equation for various suctions.

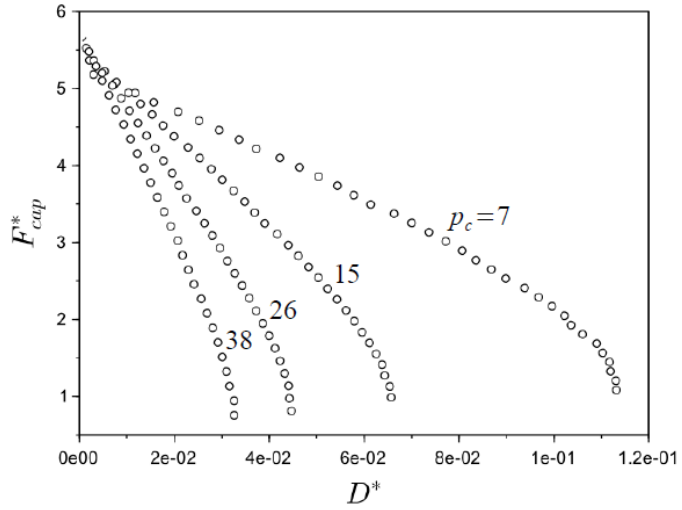

(a)

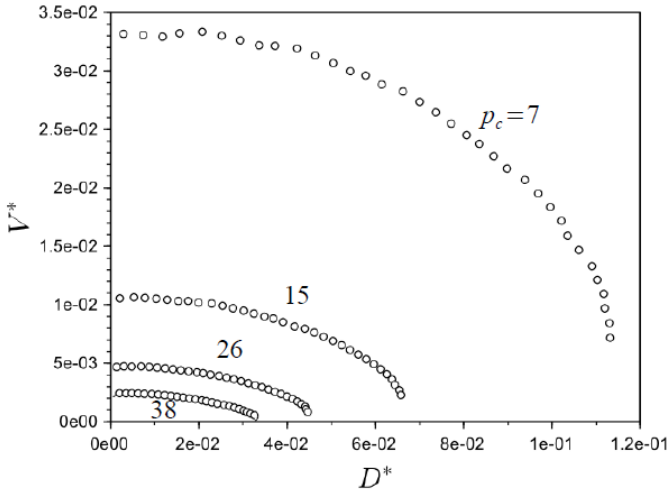

(b)

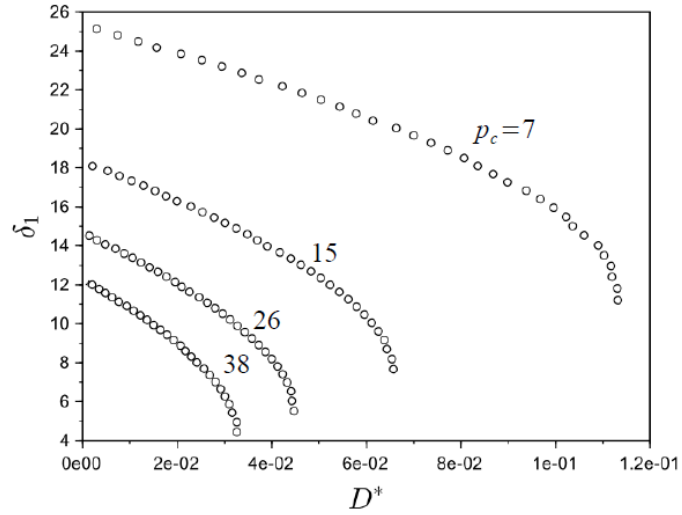

(c)

Figure 2.9 The identified stable solution of Laplace-Young for various suction values.

2.3.3 Roughness of the grains

Another aspect added to the capillary law in YADE is the roughness of the grains. The roughness aspect helps representing the real shape of the grains and the dependence of the capillary effect on that.

The first to take into account the effect of the roughness of the grains was [64] by considering a separation $2s$ between two smooth idealized spheres. This approach has been used by many authors afterwards [50, 51, 55]. The same approach has been used in our model by considering not only positive but also negative separation. The model is based on the work of [50]. The roughness is represented by considering that the meniscus is formed between spherical grains slightly smaller or bigger than the grains for the contact law. The roughness can be then either positive or negative. In the case of positive roughness, the grains are touching through asperities (figure 2.10 b). When the roughness is negative, the sphere has some plane surfaces, and it's volume is smaller than the sphere used for the capillary law(figure 2.10 a). The model is not able to describe the behavior of quite angular grain shape, since the shape of the rough grain in the code is estimated to be spherical. If the grain is too angular the approximation becomes viral.

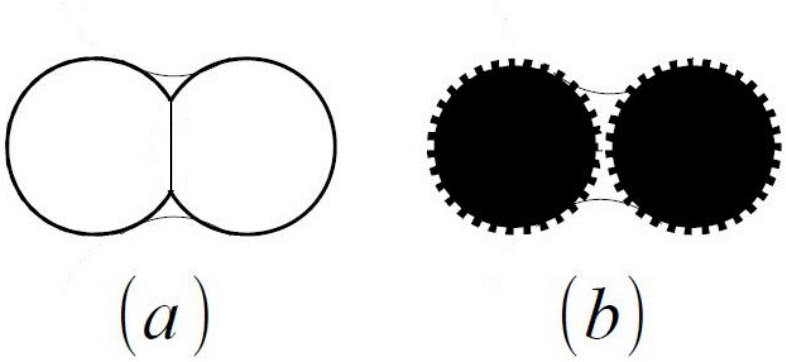

Figure 2.10 Illustration of particles with (a) negative and (b) positive roughness.

The value κ of the roughness is taken into account for each grain as following:

$$r_{rough} = r(1-\kappa) \tag{2.32}$$

The way the roughness is taken into account in the DEM code is represented in figure 2.11.

The impact of the roughness on the capillary force is shown in figure 2.12. The capillary force of a meniscus connecting rough grains is calculated using Young-Laplace equation considering that the radii of the grains used in the pendular law are (r_{rough} and R_{rough}) instead of the ones used in the contact law (r and R).

It is noticed that for smooth grains in contact, the force is almost constant with the change of suction (perfect spherical regime). For positive roughness, the capillary force decreases with increasing suctions. The negative roughness instead increases the value of the capillary force with increasing suction.

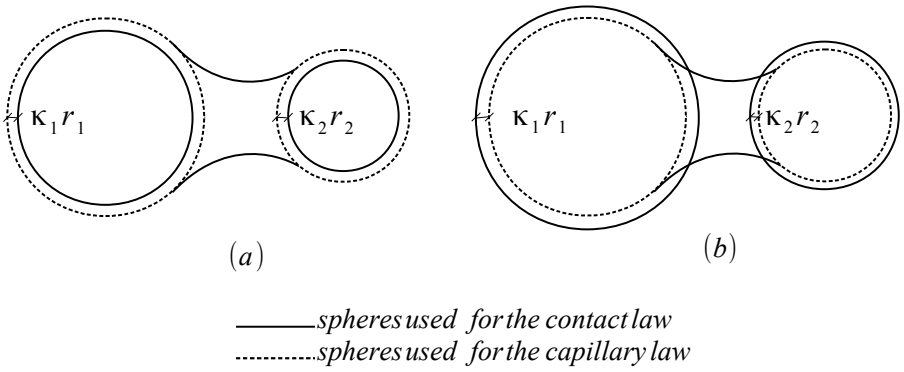

Figure 2.11 (a)Negative and (b)Positive roughness as taken into account in the numerical model.

In the case of a packing of grains, a mean value of the roughness κ_m and the value of the dispersion from the mean value $(\kappa_{max} - \kappa_m) = (\kappa_m - \kappa_{min})$ are defined in such a way to have a uniform distribution of the values of roughness.

Each grain is characterized by a value of roughness. A capillary bridge can form then between 2 grains of different roughnesses (both positive, both negative or one positive and one negative depending on the choice of κ_m, κ_{max} and κ_{min}).

$$\kappa_{min} < \kappa_m < \kappa_{max} \tag{2.33}$$

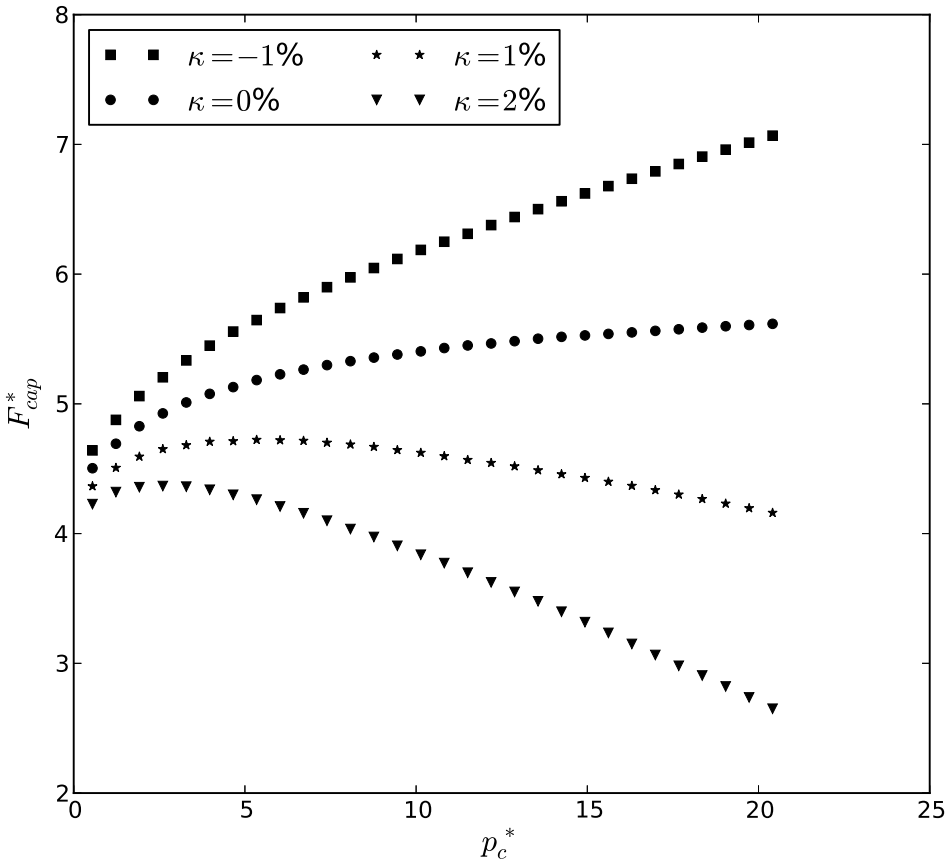

Figure 2.12 Influence of the suction change on the capillary force for various values of roughness for two grains in contact.

2.4 Capillary Interaction Law: look up table

The look up table methods is used during the simulations to determine all the variables related to the presence of the water. The method consists in creating a data file that replaces the runtime computations and makes the calculations much faster.

Many discrete configurations for Laplace equation are then solved for different ratios of radii r/R and saved in text files.

The values of the imposed input values cover all the possible range of solution. r/R varies from 0.1 to 1 to allow simulating different particle size distribution in the packing, D^* cover the range of distance from the formation to the rupture of the bridge, and the suction varies from 0 to very high suction values($p_c^* = 200$). δ varies from 0 to 90 degrees.

During the simulations, there are two possible options:

- Simulation at constant suction: The distribution of the volume with the displacement of the grains connected by a bridge, is such that the suction (p_c) remains constant.
- Simulation at constant volume: The volume of the bridge remains constant when the grains connected by a meniscus are moving.

During the simulation at imposed suction, the size of the particles, their positions are known. The trio (r/R,D^*,p_c^*) can be deduced. The discrete set of solutions in the text files is triangulated using Delaunay triangulation, and the capillary force applied to the particles and the other variables are obtained by interpolation. S_{p_c}, the set of solution corresponding to the trio (r/R,D^*,p_c^*)is:

$$S_{p_c}(r/R, D^*, p_c^*) = (F_{cap}^*, V^*, \delta_1, \delta_2, A_{wn}^*, A_{sw}^*, A_{sn}^*) \tag{2.34}$$

This interpolation is called the P-Based interpolation and is used to simulate drained quasi-static simulations.

During simulation at imposed volume, the V-Based interpolation is introduced. The input variables for this interpolation are (r/R,D^*,V^*) and the same procedure is repeated with different triangulation set.

S_{p_c} is the set of solution corresponding to the trio (r/R,D^*,V^*).

$$S_V(r/R, D^*, V^*) = (F_{cap}^*, p_c^*, \delta_1, \delta_2, A_{wn}^*, A_{sw}^*, A_{sn}^*) \tag{2.35}$$

In the case of rough grains, the radii of the grains used in the pendular capillary law are the one used in the interpolation.

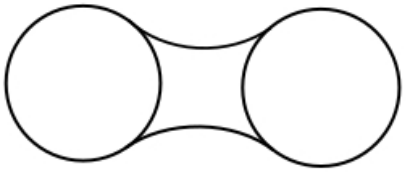

Random Configuration

$p_c = cte$	$V = cte$
$S_{p_c}(r/R, D, p_c) = (F_{cap}, V, \delta_1, \delta_2, A_{wn}, A_{sw}, A_{sn})$	$S_V(r/R, D, V) = (F_{cap}, p_c, \delta_1, \delta_2, A_{wn}, A_{sw}, A_{sn})$
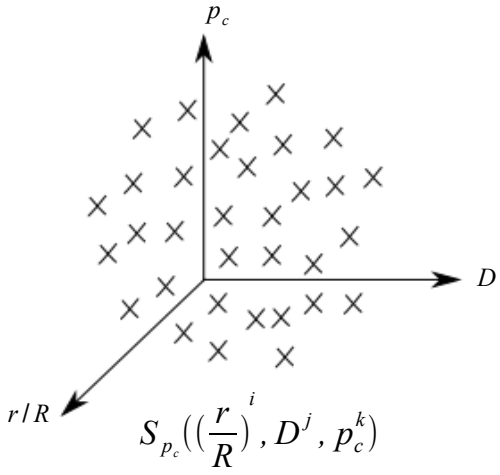	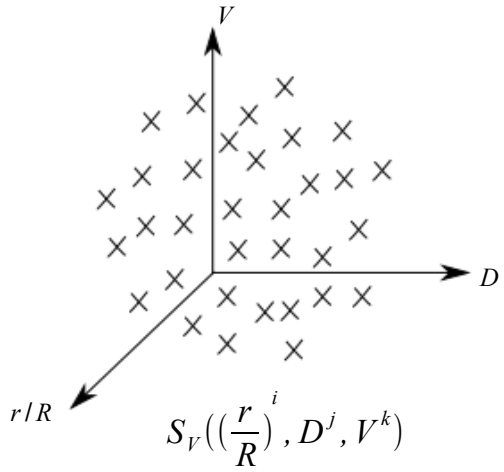
$S_{p_c}((\frac{r}{R})^i, D^j, p_c^k)$	$S_V((\frac{r}{R})^i, D^j, V^k)$

Interpolation scheme for: $S_x((\frac{r}{R}), D, x)$ $\quad x = p_c, V$

Step 1

$$(\frac{r}{R})^{i-1} < (\frac{r}{R}) < (\frac{r}{R})^{i+1}$$

$$S_x((\frac{r}{R}), D, x) = S_x((\frac{r}{R})^{i-1}, D, x) + \frac{(\frac{r}{R}) - (\frac{r}{R})^{i-1}}{(\frac{r}{R})^{i+1} - (\frac{r}{R})^{i-1}} * (S_x((\frac{r}{R})^{i+1}, D, x) - S_x((\frac{r}{R})^{i-1}, D, x))$$

Step 2

$$(D)^{j-1} < (D) < (D)^{j+1}$$

$$S_x((\frac{r}{R}), D, x) = S_x((\frac{r}{R}), D^{j-1}, x) + \frac{D - D^{j-1}}{D^{j+1} - D^{j-1}} * (S_x((\frac{r}{R}), D^{j+1}, x) - S_x((\frac{r}{R}), D^{j-1}, x))$$

Step 3

$$(x)^{k-1} < (x) < (x)^{k+1}$$

$$S_x((\frac{r}{R}), D, x) = S_x((\frac{r}{R}), D, x^{k-1}) + \frac{x - x^{k-1}}{x^{k+1} - x^{k-1}} * (S_x((\frac{r}{R}), D, x^{k+1}) - S_x((\frac{r}{R}), D, x^{k-1}))$$

Figure 2.13 Interpolation scheme for a random configuration from the look up table discrete solutions, in the case of suction and volume control

The values obtained from the interpolation in the text files are normalized, and need to be re-upscaled to the real particles size distribution present in the sample during the simulation.

Simulations are done on two grains connected by a water bridge and the variation of the force and the geometric properties of the meniscus are plotted as function of the distance separating the grains in the case of constant suction and constant volume interpolations (figure 2.14).

We observe from the simulation that for the capillary force and interfaces, the results are the same for grains moving at constant suction or constant volume of water up to a critical value ($D^* = 0.03$ in this case) before they start diverging.

At constant suction the volume of the bridge decreases until the meniscus is broken. When the volume of water is kept constant, the suction increases slightly in the beginning and then decreases almost linearly until rupture.

It is also noticed that the rupture distance of the bridge in the case of grains that moves at constant volume is higher than in the case of constant suction. The value of the capillary force is also higher if the volume of the bridge is kept constant during the movement of the grains.

2.5 Limitation of the model

When the saturation increases in the granular material, the volumes of the bridges increase, until some start to overlap. In reality, the bridges overlapping, transform into one meniscus in fusion with complex geometry to minimize the energy of the interfaces which result in diminishing the capillary force that becomes smaller than the sum of the forces of both overlapping bridges. The determination of the force is then quite complex. At this stage, the pendular model is not anymore valid.

The overlapping of the bridges is tested in the code by a hypothesis based on the filling angles (figure 2.15). If the angle $O_1O_2O_3$ is smaller that the sum of both filling angle the menisci $\delta_{12} + \delta_{23}$ are overlapping.

The fusion of the menisci can be tested systematically in the code to make sure that the simulation is still realistic.

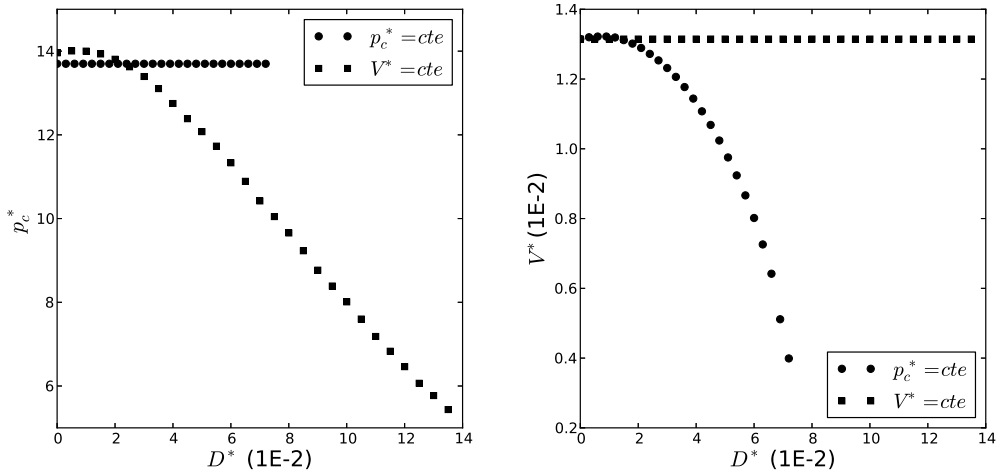

(a) (b)

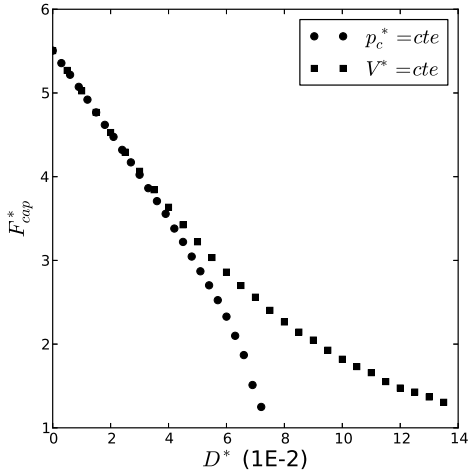

(c)

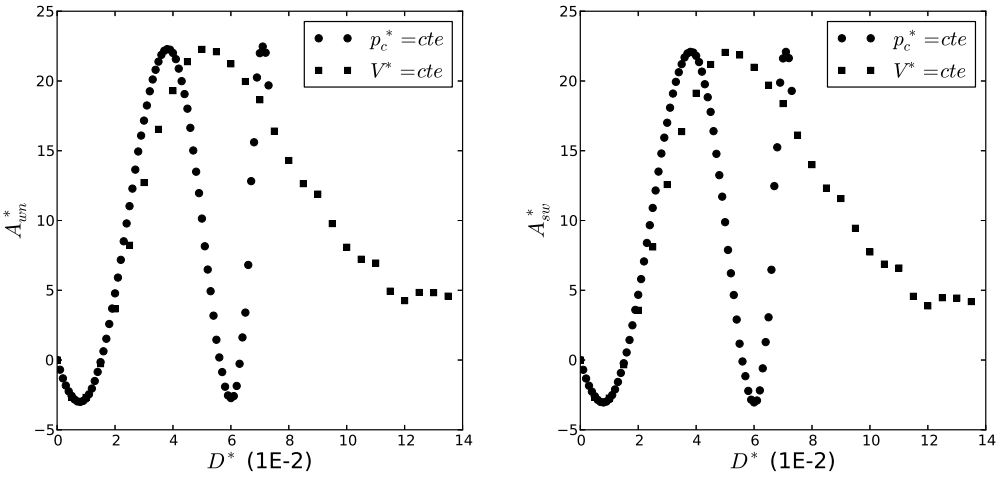

(d) (e)

Figure 2.14 Comparison between the suction and volume control for a random configuration showing the variation of suction, volume, force and interfaces with the distance between the grains.

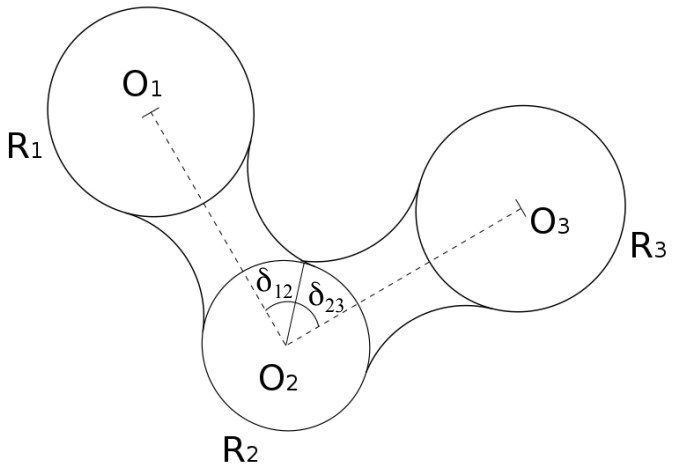

Figure 2.15 Illustration of menisci starting to overlap.

2.6 Conclusion

In this chapter the numerical tool YADE is briefly presented. The pendular capillary interaction law is also introduced taking into account the capillary effects in the pendular regime.

The assumptions taken into account in the numerical modeling of the liquid bridges are presented. Based on these assumptions the exact numerical solution of Young-Laplace equation is solved. The resolution of Young-Laplace, in both suction and volume control cases, allows to calculate the forces acting on the grains, the volume of liquid in the ring and the amount of the interfaces that separate the three phases present in the granular media which is a novelty of this model. These interfaces are used in the following chapters to calculate the internal energy component related to these terms and verify that the model is consistent from a thermodynamic point of view and comment on the role they can play in the behavior of unsaturated materials.

The roughness of the grains taken into account in the capillary interaction law is another novelty of this model. The influence of the roughness on the capillary force evolution is presented and is shown to be significant. The roughness influences significantly the value

of the capillary forces but also qualitative influence on the sign of evolution of the capillary force with positive and negative roughness is shown. Finally the limitations of the numerical model are discussed.

Chapter 3

Energetic study of three phase systems

3.1 Introduction

This chapter aims to bridge the DEM simulations and the thermodynamic vision of multi-phase materials by checking if the numerical model is consistent from an energetical point of view. To accomplish this purpose and make the discussion easier, a thought experiment inspired by [54] on a two-grain system is generalized to moving grains. It provides a simple test case for the model verification: The external work in the case of an open or closed system, and the internal energies including the energies of the interfaces separating the different phases in the granular material are calculated and the energy balance of the system is then verified. In the second part of the chapter, the energy balance for a packing of grains is also verified.

3.2 Energy balance of a two-grain system

In [54], the energy balance is written for a system of two immobile rigid grains subjected to changes of matric suction. In this chapter, the system is extended to moving particles.

The system is represented in figure 3.1. It is a model system of two solid grains, bridged by a wetting fluid (w-phase) and otherwise surrounded by another non-wetting fluid (the n-phase). The solid phase is represented by two spherical grains of radii R and r. The wetting fluid can leave or enter the bridge through a passage into one of the particles. We assume perfect wetting conditions, consequently the change in the volume of the wetting phase and surface areas is assumed to be reversible. The walls of the pistons have no contribution to the energy of the interfaces and the movement of pistons occurs in a way to keep equilibrium

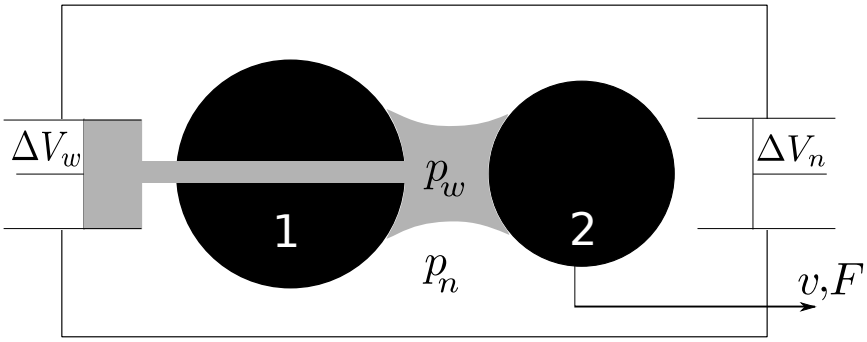

Figure 3.1 Idealized system inspired by the work of Morrow (1970) [54]

in the sample. The piston of the non-wetting phase moves in a way to keep the pressure of the phase p_n constant (i.e. $\Delta V_w = -\Delta V_n$).

The original system of Morrow is extended by considering a possible movement of particle 2. This movement is ensured by attaching particle 2 to a movable axe at constant velocity v. The particle 1 remains fixed.

We assume no energy dissipation in the system, then there is only the first law of thermodynamics to be verified. For the first law of thermodynamic to be verified, the sum of all the internal energies of the components of the system must be equal to the external work supplied to the system.

3.2.1 External work

The external work supplied to the system going from an arbitrary state A to another state B is calculated as the sum of 2 components; a part related to the work done on the system by moving the piston connected to the bridge to provoke a change in the volume of the wetting liquid dV_w and one related to the displacement of grains.

$$W_{ext}^{A\to B} = \int_A^B F du + \int_A^B p_w dV_w + \int_A^B p_n dV_n \tag{3.1}$$

$dV_w = -dV_n$ that implies that $\int_A^B p_w dV_w + \int_A^B p_n dV_n = -\int_A^B (p_n - p_w) dV_w$, W_{ext} can be then written as following:

$$W_{ext}^{A\to B} = \int_A^B F du - \int_A^B p_c dV_w = \int_A^B (F_n + F_{cap}) du - \int_A^B p_c dV_w \tag{3.2}$$

F is the total force applied externally on particle 2 and keeping it in equilibrium. It is the

sum of the contact force and the capillary force resulting from the presence of ring. Note that the contact does not necessarily exist in all cases. If the grains are distant, the capillary force remains the only force acting on the particles.

W_{ext} is the total external work, p_c is the matric suction, V_w is the volume of meniscus, F_n is the normal contact force , F_{cap} the capillary force and u is the normal relative displacement between the grains:

$$u = O_1O_2 - R - r, \tag{3.3}$$

with O_1 and O_2 the centers of the particles 1 and 2 respectively; R and r their radii.

We denote for the following W_c the work done by the contact force and W_γ the work corresponding to the presence of the fluid.

$$W_c = \int_A^B F_n du \tag{3.4}$$

$$W_\gamma = \int_A^B F_{cap} du - \int_A^B p_c dV_w \tag{3.5}$$

W_{ext} is the sum of W_c and W_γ.

3.2.2 Internal energies

The change in the total internal energy of the system is divided into 6 components, the change in the energies of the three phases and of the three interfaces present in the system.

$$\Delta E_i = \Delta E_s + \Delta E_w + \Delta E_n + \Delta E_{wn} + \Delta E_{sw} + \Delta E_{sn} \tag{3.6}$$

s denotes for solid, *w* for wetting, *n* for non wetting, *wn* for wetting-non wetting, *sn* for solid -non wetting and *sw* for solid-wetting.

The pressure of the non wetting liquid is kept constant which means that the change in its potential is null. The change in the internal energy of the wetting liquid is also null as it is considered an incompressible fluid.

The internal energy change of the solid phase is equal to the elastic energy change in the system. We neglect the energy of deformation of the grains due to the surface tension and fluid pressure exerted on their surface. This is justified by the assumption that the area of the solid contacts is much smaller than the area covered by the pendular bridge, leading to dominant energy terms from the former. We assume a linear elastic contact behavior in

compression and no traction, hence the energy of deformation in the system is defined as:

$$E_S = E_{el} = 0.5k_n u^2 + 0.5k_t v^2 \qquad if\, u < 0 \qquad else \qquad E_{el} = 0 \tag{3.7}$$

k_n and k_t are respectively the contact normal and shear stiffnesses; u and v are the relative displacements in both normal and shear directions between the grains if the grains are in contact.

For the moment, only normal displacement is applied($\Delta v = 0$). In these conditions the integral of equation 3.4 is explicitely given by assuming that the contact is persistent for the sake of simplicity:

$$W_c = \Delta^{A\to B} E_{el} = 0.5k_n \Delta^{A\to B} u^2 \tag{3.8}$$

The change in the interfacial energy is:

$$\Delta E_{cap} = \gamma_{wn}\Delta A_{wn} + \gamma_{sw}\Delta A_{sw} + \gamma_{sn}\Delta A_{sn} \tag{3.9}$$

The equilibrium at contact line gives a relationship between the wetting-non-wetting surface tension γ_{wn}, the solid-wetting surface tension γ_{sw} and the solid-non-wetting surface tension γ_{sn}.

$$\gamma_{wn} cos\theta = \gamma_{sn} - \gamma_{sw} \tag{3.10}$$

In the case of perfect wetting condition $\theta = 0$ and this relationship is:

$$\gamma_{wn} = \gamma_{sn} - \gamma_{sw} \tag{3.11}$$

thus,

$$\Delta E_{cap} = \gamma_{sw}(\Delta A_{sw} - \Delta A_{wn}) + \gamma_{sn}(\Delta A_{sn} + \Delta A_{wn}) \tag{3.12}$$

Two assumptions can be made to calculate the change of the total capillary energy in the system:

case a: The surface of the grain that is not wetted by the meniscus is totally dry.

- $A_{wn} = A_1$
- $A_{sn} = A_2$
- $A_{sw} = A_3$

where A_1, A_2 and A_3 are indicated in figure 3.2.

$$\Delta E_{cap} = \gamma_{sw}(\Delta A_3 - \Delta A_1) + \gamma_{sn}(\Delta A_2 + \Delta A_1) \tag{3.13}$$

For stiff particles $\Delta A_3 = -\Delta A_2$; Replacing it in equation (3.31), the total change in capillary energy is:

$$\Delta E_{cap} = (\gamma_{sn} - \gamma_{sw})(\Delta A_1 - \Delta A_3) = \gamma_{wn}(\Delta A_1 - \Delta A_3) = \gamma_{wn}(\Delta A_{wn} - \Delta A_{sw}) \tag{3.14}$$

case b: The particles are surrounded by a water film:

- $A_{wn} = A_1 + A_2$
- $A_{sn} = 0$
- $A_{sw} = A_2 + A_3$

When the particles are covered by a film, the solid-non wetting interface doesn't exist and the change in the solid-wetting interface is equal to zero ($\Delta A_{sw} = \Delta A_2 + \Delta A_3 = 0$); that leads to:

$$\Delta E_{cap} = \gamma_{wn}(\Delta A_1 - \Delta A_3) \tag{3.15}$$

Both assumptions lead to the same result. Therefore, the presence of the film around the particles or its absence has no influence on the energy balance of the system. In the following we take into account the case of the dry particles bonded by wetting liquid menisci.

If the wetting liquid is water and the non wetting liquid is gas the surface tension γ_{wn} is equal to 0.073 N/m.

Hereafter, all quantities are given in dimensionless forms.

$$p_c^* = \frac{p_c R}{\gamma_{wn}} \tag{3.16}$$

is the normalized capillary pressure.

For the 2 grains system, the internal energies and external work are normalized by $\gamma_{wn} * R^2$. R is the radius of the bigger grain.

$$\Delta W_{ext}^* = \frac{\Delta W_{ext}}{\gamma_{wn} R^2} \tag{3.17}$$

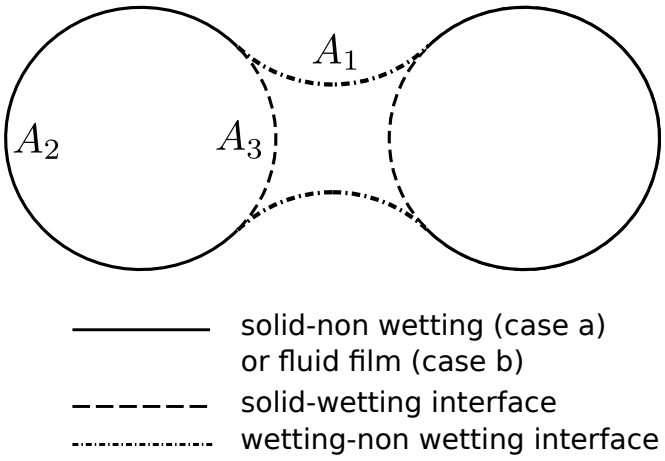

Figure 3.2 Illustration of the three existing interfaces

$$\Delta E^*_{el} = \frac{\Delta E_{el}}{\gamma_{wn} R^2} \tag{3.18}$$

$$\Delta E^*_{cap} = \frac{\Delta E_{cap}}{\gamma_{wn} R^2} = \Delta E^*_1 - \Delta E^*_3 \tag{3.19}$$

where $E_1 = \gamma_{wn} \Delta A_1$ and $E_3 = \gamma_{wn} \Delta A_3$.

3.3 Model verification

3.3.1 External work input

To check the energy balance of the system, DEM simulations are performed.

Different loading paths leading to some external works are applied to the system of figure 3.1 either by imposing a constant velocity v to particle 2 (keeping the suction constant) or by changing the matric suction in the medium (keeping both grains fixed).

The grains are initially in contact. Displacement at constant positive velocity is applied in the first path and the suction is kept constant (A→B). The second path is applied by fixing displacement and changing suction (B→C). Negative velocity is then applied to make the grains back in contact (C→D). The grains fixed again, the suction is decreased to the initial value(D→E)(figure 3.3).

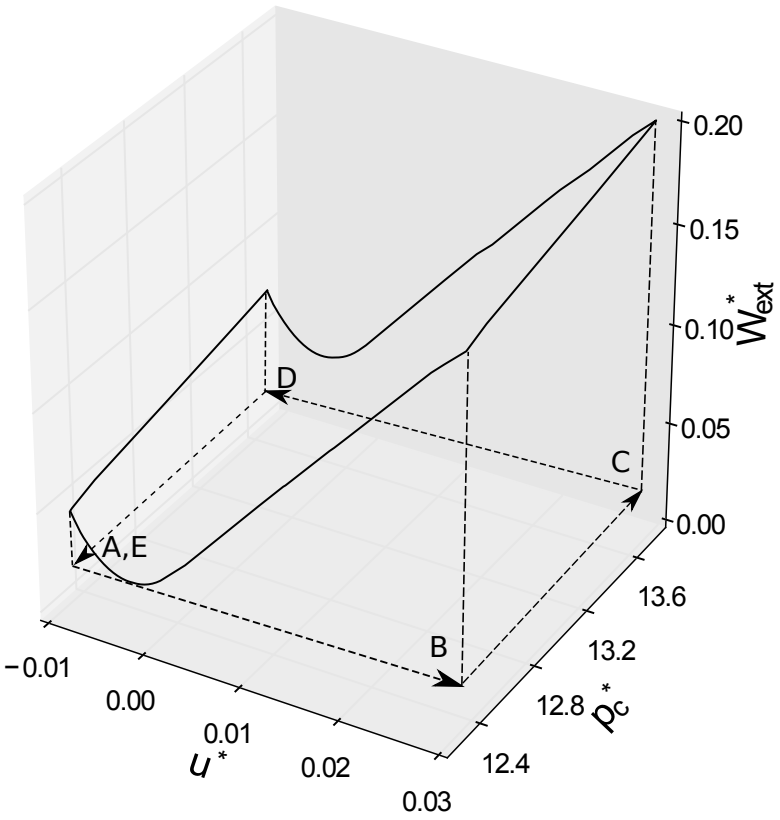

Figure 3.3 The path of the external work applied to the system as function of the suction and the relative displacement

Figure 3.3 shows the plot of the external work per volume integrated in time using equation 3.2, as function of the normalized suction and the relative displacement of the grains($u^* = u/R$), and the different paths applied to the system.

There is no energy dissipation in the system, in this case all paths are reversible and the total energy supply to move the system from a state to another is path independent ($E \equiv A$). Therefore it must be possible to define a formulation for the stored energy depending only on the current configuration.

3.3.2 Internal free energy

The internal energy components (ΔE^*_{el} and ΔE^*_{cap}) and the total internal energy change (ΔE^*_i) of the system are plotted in figure 3.4. When the grains are in contact, the internal energy is the sum of both elastic and capillary energy. When they are distant, the elastic energy is null and the only component that remains is the energy of interfaces.

It is found that the interfacial energy changes by the combined effects of p_c and u, whereas the solid free energy depends on u only (as a result of the contact model assumptions), thus

$$E_i = E_i(u, p_c) = E_{el}(u) + E_{cap}(u, p_c) \tag{3.20}$$

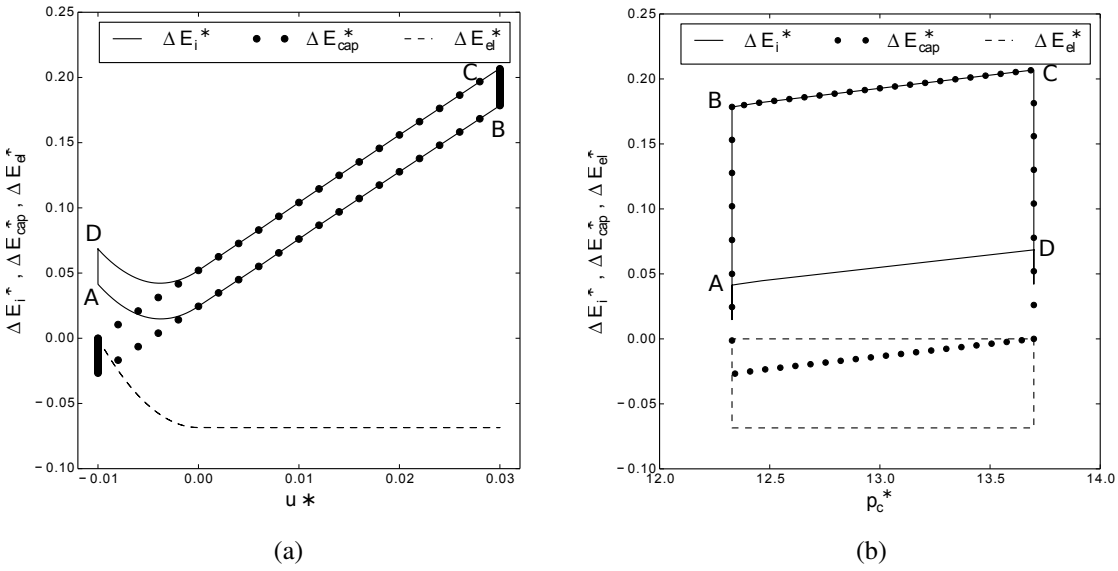

(a) (b)

Figure 3.4 The change of elastic energy , interfacial energy and total internal energy as function of(a)relative displacement and (b) suction.

ΔE_1^* and ΔE_3^* are plotted as function of suction and displacement in figure 3.5. It is noticed that in the pendular regime, both components vary in the same direction. A growth in the wetting-non wetting interface is accompanied by a growth in the solid -wetting interface and vice-versa.

$$sign(\Delta E_1^*) = sign(\Delta E_3^*) \tag{3.21}$$

The plots also show that the difference ($\Delta E_{cap}^* = \Delta E_1^* - \Delta E_3^*$) that is equal to the total interfacial energy is much smaller than the value of each component taken separately. Therefore, neglecting the change of one of the interfaces in the system (keeping only the interfaces between fluids, typically) would lead to a large error in the evaluation of internal free energy.

3.3.3 Energy balance

The first law of thermodynamics implies that the sum of the change in all internal free energies is equal to the total external work supplied to the system:

$$W_{ext} = \Delta E_i \tag{3.22}$$

This requirement provides an efficient verification test for the numerical model. The computed change of internal energy and the external work are plotted as function of displacement and suction in figure 3.6. The plots show that the energy balance is verified. The error does not exceed 1%.

The numerical error is caused by the estimation of interfacial areas and it is acceptable. Note that both ΔE_1^* and ΔE_3^* are large, but cancel out partly resulting in much smaller amplitude of ΔE_{cap}^*, hence a maximization of the numerical errors.

Employing the previous decompositions,

$$W_c + W_\gamma = \Delta E_{el} + \Delta E_{cap} \tag{3.23}$$

where, by definition, $W_c = \Delta E_{el} = \Delta(k_n u^2)$. Hence we have also $\Delta E_{cap} = W_\gamma$, which expands to

$$\int F_{cap} du - \int p_c dV_w = \gamma_{wn}\Delta A_{wn} + \gamma_{sw}\Delta A_{sw} + \gamma_{sn}\Delta A_{sn} \tag{3.24}$$

i.e. the change of interfacial energy correspond to the sum of the work done by the capillary force in the displacement u and of the work input necessary to change the volume of the

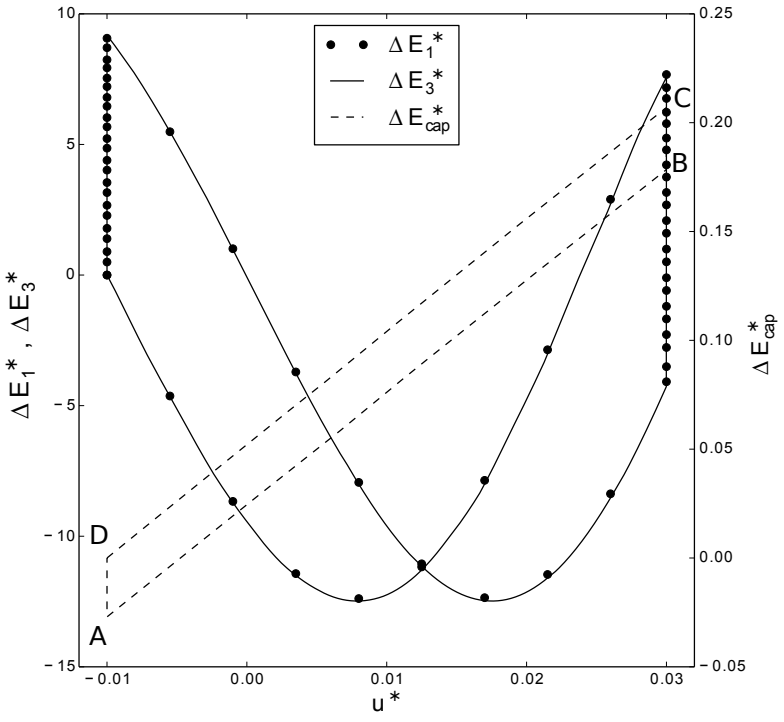

(a)

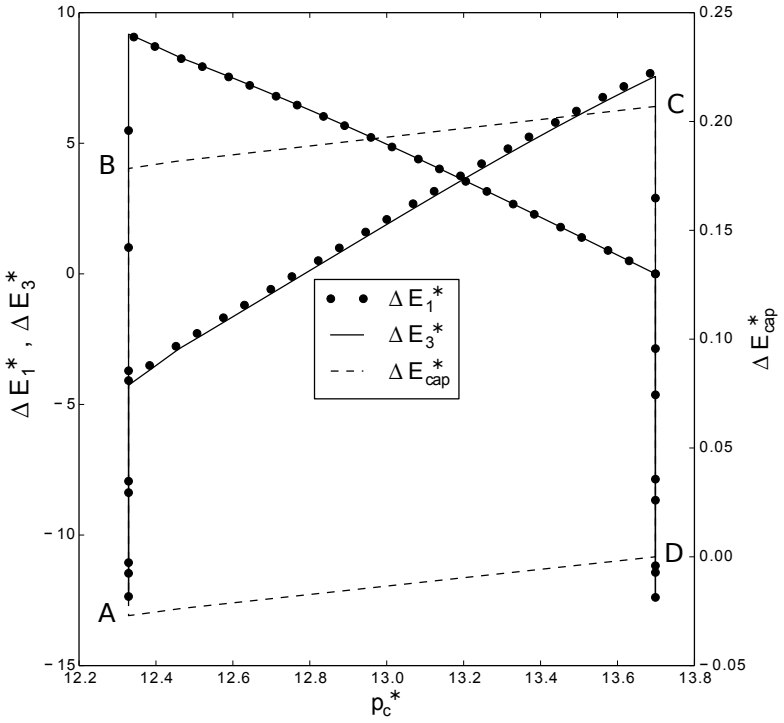

(b)

Figure 3.5 The energy change of each interface and the total capillary energy change as function of (a) relative displacement and (b) suction.

w-phase, and we have namely:

$$F_{cap} = \frac{\partial E_{cap}}{\partial u} \tag{3.25}$$

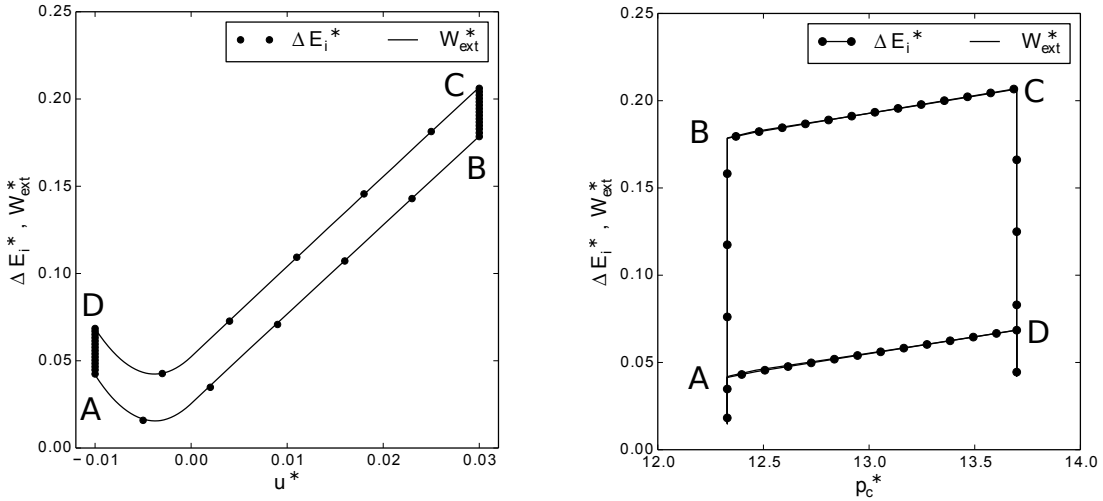

(a) (b)

Figure 3.6 The energy balance of the system as function of (a) relative displacement and (b) suction

3.3.4 Movement at constant suction or constant volume

The movement of the grains in the previous section was conducted at constant suction. The same simulations can be repeated in the case of constant volume control. The particle 2 moves then while the volume of the ring is kept constant.

We represent here the path (A→B). In this case, the system is closed and the liquids do not leave or enter the system. The term $\int_A^B p_c dV_w$ of the external work is equal to zero:

$$W_{ext}^{A\to B} = \int_A^B F du \tag{3.26}$$

Figure 3.7 show that the external work and total internal energy change is the same until it starts diverging after a certain value of displacement (as a result of figure 2.14 in chapter 2). It is also noticed that the work supply needed to move the particle at constant suction is higher than the work needed to provoke the movement at constant volume of wetting liquid.

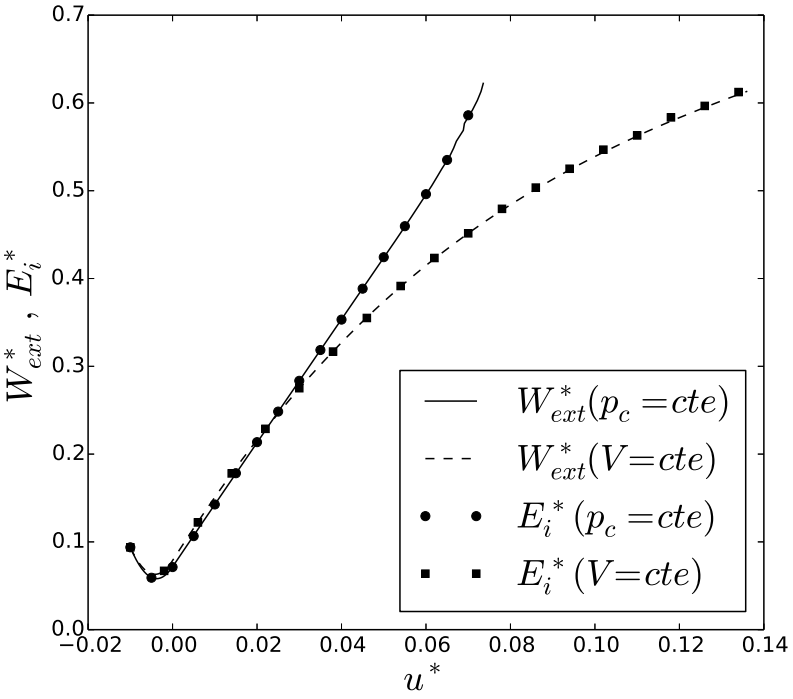

Figure 3.7 Energy balance for the path A $\rightarrow$ B for suction and volume control cases.

If we compare the capillary force evolution with the inter-granular distance in chapter 2 (figure 2.14), in the case of suction and volume control, we notice that F^*_{cap} is lower in the case of suction control. Then:

$$\int_{A(p_c=cte)}^{B} F du < \int_{A(V=cte)}^{B} F du \tag{3.27}$$

But the term $-\int_A^B p_c dV_w$ that is positive in the case of suction control since the volume decreases with increasing inter-particle distance, increases the value of the external work in the case of suction control. And even if the value of the interfaces in the case of volume control is higher, it is the difference $(\Delta A_{wn} - \Delta A_{sw})$ that matters in the calculation of the internal energy.

3.4 Energy balance of a packing

3.4.1 Sample preparation

The energy balance is now examined for a simulated random packing of grains.

For a given particle size distribution, the grains are randomly distributed in a cubic volume. The inter-granular friction angle is fixed. Lower it is, denser the packing is. It allows the grains to rearrange in the sample to have a lower porosity. Once the packing is compacted until the desired initial isotropic confinement is reached, the final angle of friction is set to 30 degrees.

The compaction occurs with periodic boundary conditions. Periodic boundary conditions are helpful to simulate large or infinite systems from a unit cell.

The numerical samples used to verify the energy balance are composed of 1000 spherical grains with periodic boundary conditions. The granulometry is tightly graded and the dispersion from the mean radius (0.1 mm) is 10 percent. The initial isotropic confinenemt is 1 KPa.

Once the dry packing compacted, the capillary forces are added while no macro deformations occur. The inital saturation in the sample is 0.01.

The final packings are subjected to small isotropic deformation at constant suction. We find that during the loading the dissipated energy is negligible. It remains smaller than 0.1 % of the value of the total work applied on the sample. The number of menisci also remains constant, there isn't any energy loss or gain due to the breakage or formation of menisci.

3.4.2 Energy balance

Since free energy is additive, the total free energy is simply the sum over all grain pairs of the free energies defined previously:

$$\Delta E_i = \Delta E_{el} + \Delta E_{cap}. \tag{3.28}$$

ΔE_{el} and ΔE_{cap} now denote the changes of the total elastic free energy and of the total interfacial energy respectively:

$$\Delta E_{el} = \sum_{s \in \mathscr{S}} \Delta E_{el}^s \tag{3.29}$$

$$\Delta E_{cap} = \sum_{s \in \mathscr{S}} \Delta E_{cap}^s \tag{3.30}$$

with $\mathscr{S}$ the set of interacting pairs.

The external work in the infinitesimal strain approximation is

$$dW_{ext} = V\boldsymbol{\sigma} : d\boldsymbol{\varepsilon} - p_c dV_w \tag{3.31}$$

Here $\boldsymbol{\sigma}$ is the total Cauchy stress and $d\boldsymbol{\varepsilon}$ is an increment of the macroscopic strain corresponding to the deformation of the periodic space. V_w is the volume of water in the sample, and V the volume of the sample. In the numerical model $d\boldsymbol{\varepsilon}$ is imposed by deforming the periodic cell. $\boldsymbol{\sigma}$ is evaluated using the expression of total stress of [75], i.e.

$$\boldsymbol{\sigma} = \frac{1}{V}\sum_{s\in\mathscr{S}} (F_c^s + F_{cap}^s) \otimes l^s \tag{3.32}$$

l^s is the branch vector joining reference points attached to the interacting particles.

In this sum F_c is null for the pairs where a pendular ring is bridging grains without contact, and V is the total volume of the packing.

As in [75], we may note $\boldsymbol{\sigma}_{cont}$ and $\boldsymbol{\sigma}_{cap}$ the stresses obtained by summing separately the contact forces and the capillary forces in equation 3.32.

$$\boldsymbol{\sigma}_{cont} = \frac{1}{V}\sum_{s\in\mathscr{S}} F_c^s \otimes l^s \tag{3.33}$$

$$\boldsymbol{\sigma}_{cap} = \frac{1}{V}\sum_{s\in\mathscr{S}} F_{cap}^s \otimes l^s \tag{3.34}$$

For the packing, the external work can be divided into 2 components (for the following):

$$dW_{el} = V\boldsymbol{\sigma}_{cont} d\boldsymbol{\varepsilon} \tag{3.35}$$

$$dW_{cap} = V\boldsymbol{\sigma}_{cap} d\boldsymbol{\varepsilon} - p_c dV_w \tag{3.36}$$

For the following, W_{el}, W_{cap} and the energy components are normalized by γ/R_m^2, where R_m is the mean radius of the grains in the packing.

The first law of thermodynamics is tested for the sample subjected to small isotropic elastic volumetric deformation of $3e-4$.

$$W_{ext} = \Delta E_i \tag{3.37}$$

Figure 3.8 shows that the energy balance is also verified for the packing of grains sub-

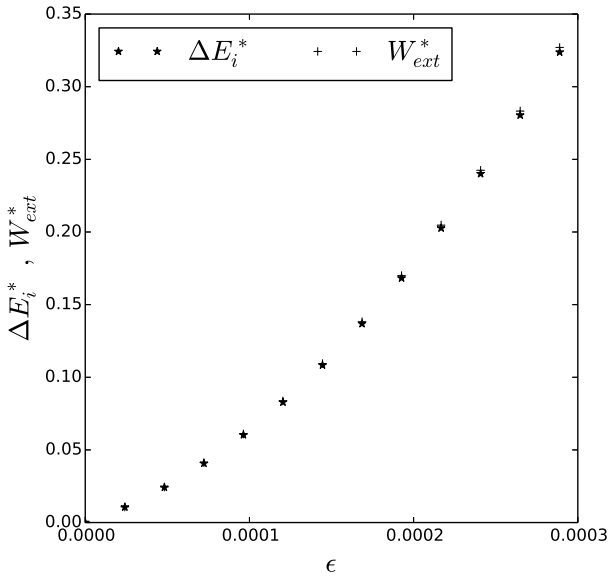

Figure 3.8 Energy balance verification for a packing

jected to deformation. The error margin is about 1%. Again, this numerical error can be explained by the fact that the change of interfacial energy is the difference of two changes which take comparable values but have same signs (see section 3.3.3).

3.5 Energy balance: Energy loss/gain and plasticity

The energetic validation of the model in the previous sections has been done only in the elastic regime and when the number of menisci is constant during the loading. But when a granular medium is deformed, or when drainage and imbibition occur energy loss/gain in unsaturated soils will result from the breakage or the formation of menisci. When plastic deformation takes place, there is also plastic dissipation to take into account.

3.5.1 Two grains system: breakage or formation of a meniscus

When a meniscus is formed because two grains come in contact or broken when the distance separating them surpasses the rupture distance of the meniscus, there is volume and interfaces added to or lost from the system. This provokes a jump in the value of the internal

energy and the external work. We remind that the external work is:

$$W_{ext}^{A\to B} = \int_A^B F\,du - \int_A^B p_c dV_w \tag{3.38}$$

The jump in the external work is caused by the sudden change in the value of volume of water and the loss of the capillary force between the particles.

The internal energy is:

$$\Delta E_i = \Delta E_{el} + \Delta E_{cap} \tag{3.39}$$

The jump in the internal energy terms is caused by the sudden change in the value of the wetting - non wetting and wetting-solid interfaces.

The jump in both cases is not the same which means that the formation of the bridge requires external energy supply and the breakage of a menisci is accompanied by energy loss.

To calculate this energy loss when the meniscus is broken, we use the same configuration as in the system of morrow, and we subject particle 2 to a constant velocity until the distance is high enough to break the meniscus. The energy balance is plotted in figure 3.9, and is verified until the meniscus is broken.

The energy balance is then written as:

$$\int_A^B F\,du - \int_A^B p_c dV_w = \Delta E_{el} + \Delta E_{cap} + \Delta e \tag{3.40}$$

Δe is the energy loss or supply. The value of this energy (gained or lost) is equal to the difference between both the jumps of the external work and the internal energy.

$$\Delta e = p_c dV_w - \Delta E_{cap} \tag{3.41}$$

3.5.2 Energy balance for a packing

The energy balance for a packing is also verified when energy loss and gain occur. To accomplish this purpose, triaxial shear test is performed on a packing of grains.

The energy balance writes as following:

$$W_{ext} = \Delta E_{el} + \Delta E_{cap} + \Delta E_p + \Delta e + E_p + E_{kin} \tag{3.42}$$

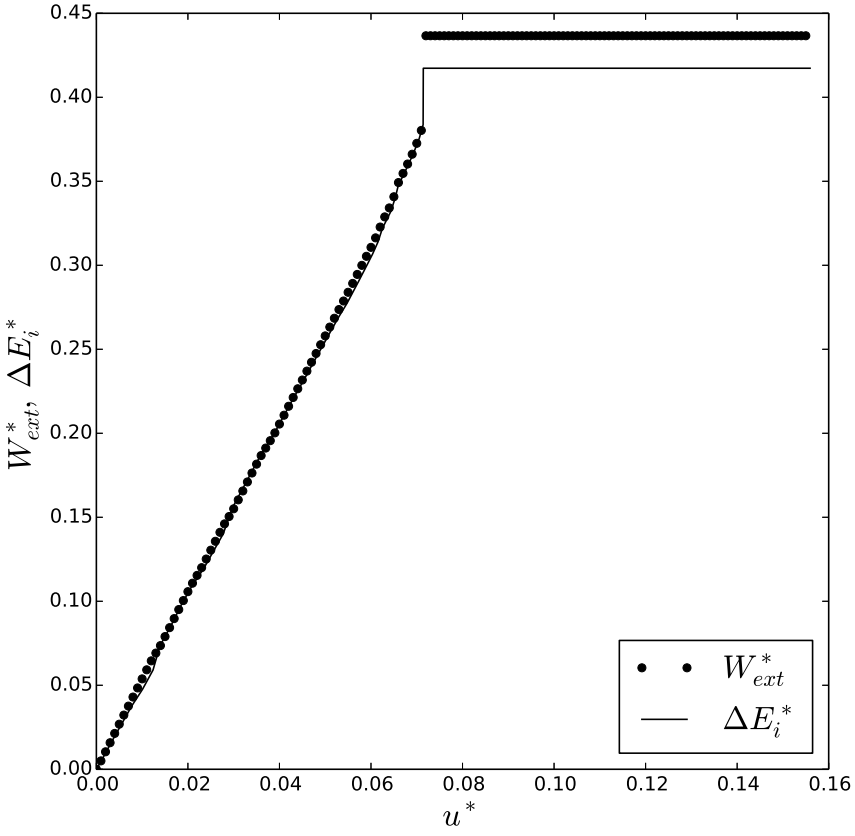

Figure 3.9 The energy balance showing the energy loss when the meniscus is broken

E_p is the plastic dissipation energy, E_{kin} the kinetic energy and Δe is the energy change due to breakage or formation of menisci:

$$\Delta e = \Sigma_{s \in S}(p_c dV_{w,s} - \Delta E_{cap,s}) \tag{3.43}$$

where S is the group of menisci that are lost or added to the sample.

The loading is quasi-static, the kinetic energy then is negligible.

Figure 3.10 shows the deviatoric stress as function of the axial deformation. All the internal energy terms are also plotted during the loading. The energy balance is verified.

3.6 Conclusion

The external work and the internal energy of a system of two grains connected by a liquid bridge are calculated. The energy balance of the system with no energy dissipation in the case of suction and volume control is verified for a system inspired by the work of [54] extended to moving particles, by applying a random external work path.

The importance of the interfaces in the energy balance of unsaturated soil is also highlighted. It has been shown that all the interfaces present in the unsaturated medium contribute in the calculation of the interfacial energy, and neglecting one of them will lead to an important error in the energy balance of the system.

Finally the energy balance for a packing of grains is also verified in elastic and plastic regime.

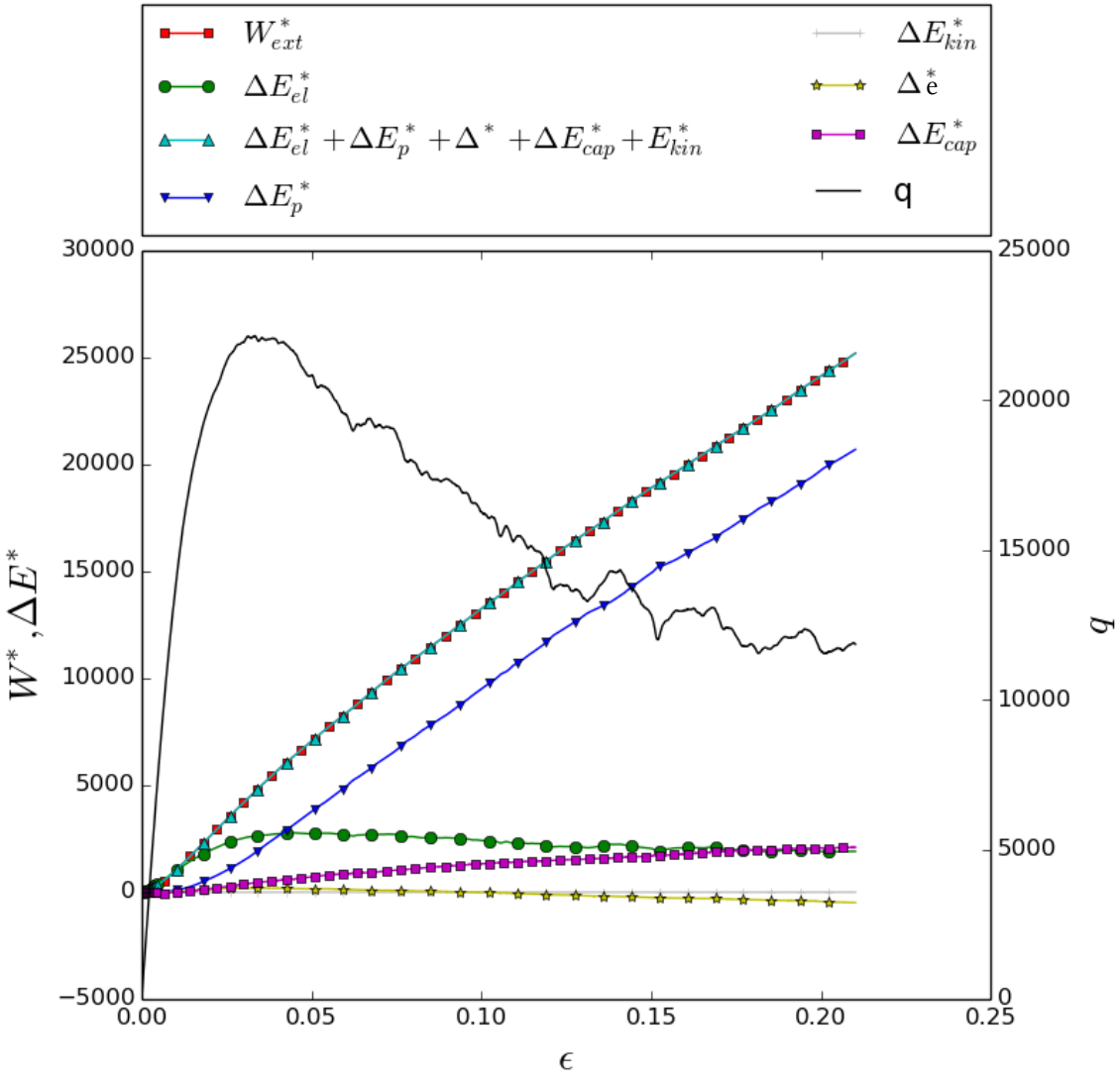
W^*_{ext}
ΔE^*_{el}
$\Delta E^*_{el} + \Delta E^*_p + \Delta^* + \Delta E^*_{cap} + E^*_{kin}$
ΔE^*_p
ΔE^*_{kin}
Δ^*_e
ΔE^*_{cap}
q
$W^*, \Delta E^*$
q
ϵ
30000
25000
20000
15000
10000
5000
0
−5000
25000
20000
15000
10000
5000
0
0.00
0.05
0.10
0.15
0.20
0.25

Figure 3.10

Chapter 4

Effective stress in three phase granular materials

4.1 Introduction

The deformation and strength of granular matters occupied by two fluid phases is dependent on the interactions between phases at the micro scale, yet the conventional methods in engineering need constitutive models at the macro-continuum scale. Hence the need for homogenized variables to describe, namely, the state of stress of granular media with multiphase pore fluids.

Constitutive relations at the continuum scale generally employ the so-called *effective stress*, a stress variable that is supposed to govern the deformation of the solid skeleton.

The concept of effective stress has been introduced by Terzaghi for water saturated soils [86]. For an incompressible pore fluid, the effective stress σ' is defined as:

$$\sigma' = \sigma - p_w I \tag{4.1}$$

where σ is the total (Cauchy's) stress tensor and p_w is the pressure of the pore fluid.

This relation is extended to unsaturated conditions [8] as:

$$\sigma' = (\sigma - p_n I) + \chi(p_n - p_w)I \tag{4.2}$$

χ is the so-called Bishop parameter that is considered to be function of the saturation and varies from 0 to 1 to cover the whole range of saturation from dry to fully saturated. χ often taken equal to the degree of saturation [8, 76].

This generalization to two-phase fluids has been a controversial topic for decades. Various alternative definitions of σ' have been introduced heuristically, and attempts to justify them empirically can be found.

Alternatively, derivations have been proposed based on thermodynamic principles. An interest of such studies is that they introduce explicit assumptions on the different components of the unsaturated medium. Namely, the importance of interfaces has been highlighted in different works [19, 30, 33, 57, 58, 58] which considered free energy terms associated to the interfaces (referred to as interfacial energy in the following).

Independently, numerical simulations based on the discrete element method (DEM) have been conducted to study granular media. The models are usually restricted to low water contents at which the wetting phase is only present in the form of pendular bridges between grain pairs [28, 37, 71, 74]. Therein, the modeling is based on expressions of forces exerted by the pendular bridges on the particles. The static analysis of such systems is now relatively common, but no attempt have been made to interpret the results with energetical points of view, that is the aim of this chapter.

In this chapter, the changes of free energy components are tracked in deforming granular systems simulated with the discrete element method. Simulations of regular and random packings are presented to check the Love-Weber expression of average stress in granular materials.

The changes of internal energy components are also evaluated with the change of saturation and the energy separation assumptions are checked.

4.2 Effective stress in the pendular regime in granular materials subjected to small deformation

The effective stress is defined as the derivative of the elastic energy with respect to the deformation of the skeleton:

$$\sigma' = \frac{1}{V}\frac{dE_{el}}{d\varepsilon} \tag{4.3}$$

This definition of the effective stress as function of the elastic energy has been used widely by many authors such as [19, 30, 33, 57, 58] that based their work on this definition to suggest Bishop's type effective stress which incorporate the effects of the interfaces separating the phases that are present in unsaturated materials. The advantage of these proposed stress framework is including the interfaces energy based on the knowledge of the water

retention curve. As a consequence, the hydraulic hysteresis is put in evidence naturally in the effective stress.

4.2.1 Contact stress

One of the definitions of the effective stress in the granular system is the one based on the micro-scale quantities. Initially introduced for dry materials, the *contact stress* [16, 42, 48, 91] in a volume V reads

$$\sigma_{cont} = \frac{1}{V}\sum_k F_{c,k} \otimes l_k \tag{4.4}$$

where k loops over all contacts, with l_k the branch vector joining reference points attached to the interacting particles.

For three-dimensional unsaturated sphere packings in triaxial compression, [75] found that the contact stress at peak was following a unique Coulomb's friction criterion be it for the dry case or in unsaturated/saturated conditions. It was then suggested as a possible micromechanical expression of the effective stress with respect to shear strength.

Since then, the above decomposition has been used by many authors in relation with analytical averaging or to study the anisotropic features of σ_{cap} (see e.g. [31, 90]). Worth noting, the initial context of peak shear strength has been often forgotten by subsequent authors who assumed (explicitely or not) that the contact stress (eq. 4.4) was the relevant stress for every aspects of the mechanical response (even though its range of applicability have been questioned [15]). It would imply namely, in the elastic regime,

$$\sigma_{cont} = \frac{1}{V}\frac{\partial E_{el}}{\partial \varepsilon} \tag{4.5}$$

.

This has been proved to be true for dry materials by [14].

In the following sections the above relationship is compared with numerical results, for a regular cubic array of spheres first, then for a random packing in unsaturated conditions in the elastic regime. The samples are subjected to small deformations,so that the response of the sample remains elastic. The solid skeleton deformation is then completely reversible. The number and the distribution of the menisci in the sample remain also invariant with respect to the deformation, which means that there is no energy dissipation due to breakage or formation of liquid bridges.

4.2.2 Regular packings

We consider a regular cubic packing of grains in unsaturated condition connected by water bridges, of $N \times N \times N$ particles of radius R with periodic boundary conditions. The packing is subjected to a macroscopic deformation defined by the strain tensor $\varepsilon = \varepsilon I$.

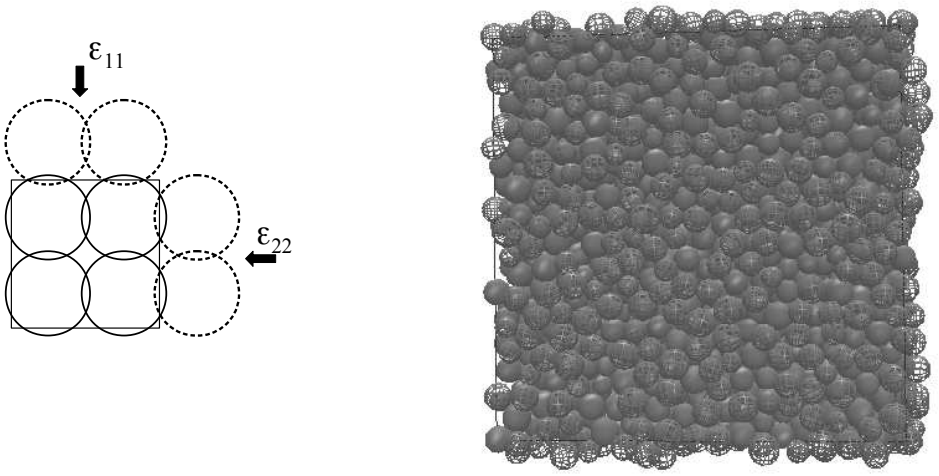

(a) (b)

Figure 4.1 (a)-Illustration of regular cubic packing and (b)- random packing with periodic boundary conditions

The contact stress tensor is calculated as following:

$$\sigma_{cont} = \frac{1}{V} \sum_{s \in \mathscr{S}} F_n^s \otimes l^s \tag{4.6}$$

$\mathscr{S}$ is the set of interacting pairs of grains.

In the case of regular packing in periodic boundary conditions the number of contacts in each direction of loading is N^3 and $l^s = 2R$

$$\sigma_{cont} = \frac{1}{V} 2N^3 F_n R I \tag{4.7}$$

F_c is the contact force (equal at each contact in the regular isotropic case).

$$\sigma_{cont} = \frac{1}{V} 2N^3 (2k_n R\varepsilon) R = \frac{1}{V} 4N^3 k_n R^2 \varepsilon \tag{4.8}$$

On the other hand the total elastic energy in the packing is:

$$E_{el} = 0.5N^3 k_n u^2 = \frac{1}{V} 0.5N^3 k_n (2R\varepsilon)^2 \tag{4.9}$$

$$E_{el} = 2N^3 k_n R^2 \varepsilon^2 \tag{4.10}$$

$$\frac{1}{V}\frac{dE_{el}}{d\varepsilon} = \frac{1}{V} 4N^3 k_n R^2 \varepsilon \tag{4.11}$$

It is hence shown that for regular packing, the contact stress is equal to $\sigma' = \frac{1}{V}\frac{dE_{el}}{d\varepsilon}$, which is equal to the effective stress.

Love-Weber formula is then able to describe the behavior of regular packing in unsaturated conditions.

$$\sigma_{cont} = \frac{1}{V}\frac{dE_{el}}{d\varepsilon} = \sigma' \tag{4.12}$$

4.2.3 Random packings

The same samples generated in the chapter 3 to verify the energy balance of a packing of grains are used in the following: one dense with an initial porosity of 0.37 and one loose sample with an initial porosity of 0.49.

The samples are subjected to small increments of isotropic deformation. The external work and the internal energy and their components are plotted as function of volumetric strain in figure 4.2. The plots show that the value of W_{el} is higher than the change of elastic energy ΔE_{el}:

$$W_{el} = V\sigma_{cont} : d\varepsilon > \Delta E_{el}, \tag{4.13}$$

i.e. the contact stress overestimates the magnitude of the effective stress. In the case of a dense packing of a porosity of 0.37, the difference is around 15 percent. When the porosity is higher ($n = 0.49$), the difference between effective stress and contact stress gets higher and the difference is larger than 66 percent.

The variation of the derivatives of internal energies with the saturation are plotted for dense and loose packings in figure 4.3.

The variation of the difference between effective and contact stress with the saturation is also plotted in figure 4.4. For dense packings, the difference is between 14 and 19 percent. It decreases until 2 percent of saturation and then reaches a constant value for higher satura-

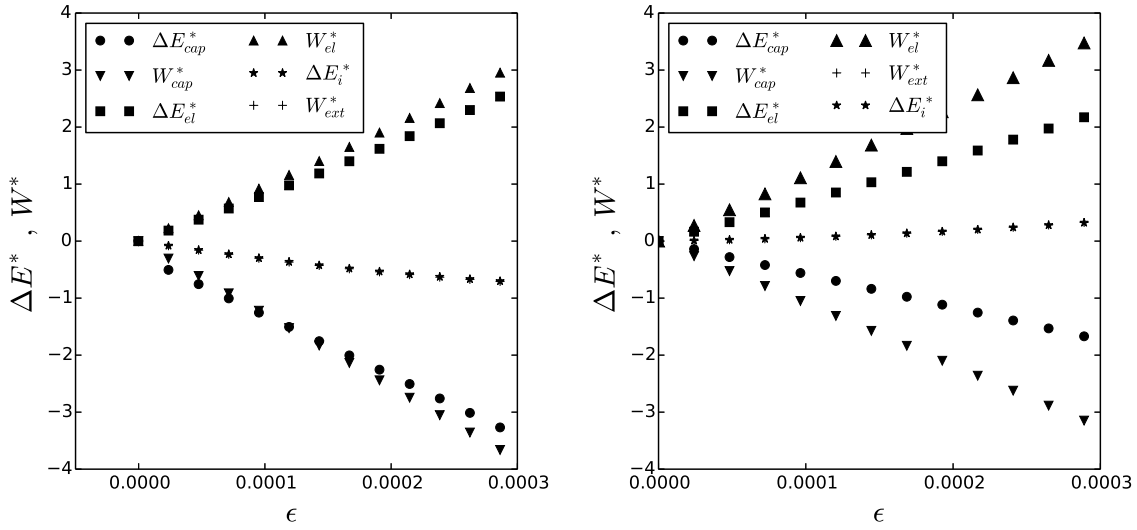

Figure 4.2 The components of external work and internal energy for wet packing in the case of isotropic compression for (a)-dense packing and (b)-loose packing

tion. For loose packing, the difference continues to decrease with increasing saturation and the curve tends to be linear on average. However the difference is always significant (larger than 40 percent) in the pendular regime.

The same simulation is repeated in undrained local condition where each meniscus keeps its volume constant until rupture.

Both cases (drained: deformation at constant suction and local undrained) can illustrate different loading rates in a packing of grains related to both different mechanisms that leads to the redistribution of water in the medium. At low rates, the suction will have the time to reequilibrate and will be uniform in the medium, which corresponds to deformation at constant suction. For grains of 1 mm diameter, the time needed is about 5 minutes which corresponds to loading rates smaller than $10^{-2}s^{-1}$ [44].

If the loading is sufficiently fast, we have local undrained conditions where the water will not have the time to transfer from a bridge to another, and all the bridges will keep their volume constant until rupture. The same situation can occur in the absence of films, when the bridges are truly disconnected.

However, it is noticed that in the case of local undrained conditions, the results do not change much. The difference in elastic energy between the local undrained and the drained case is less than 1 percent. This can be explained by the fact that 85 to 90 percent of the dis-

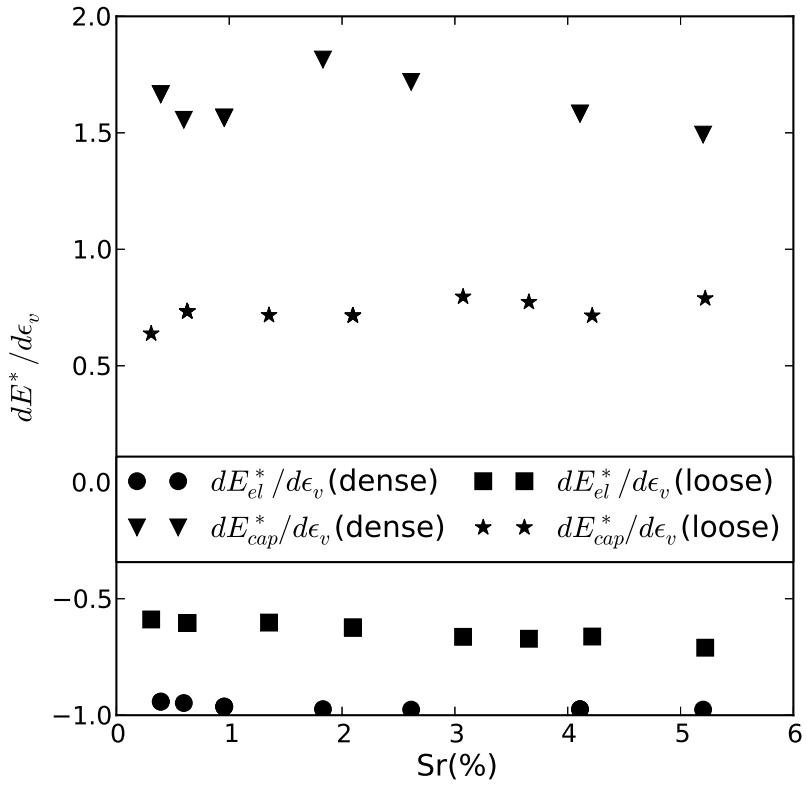

Figure 4.3 The variation with the degree of saturation of the derivative of internal energies for a dense and loose packing

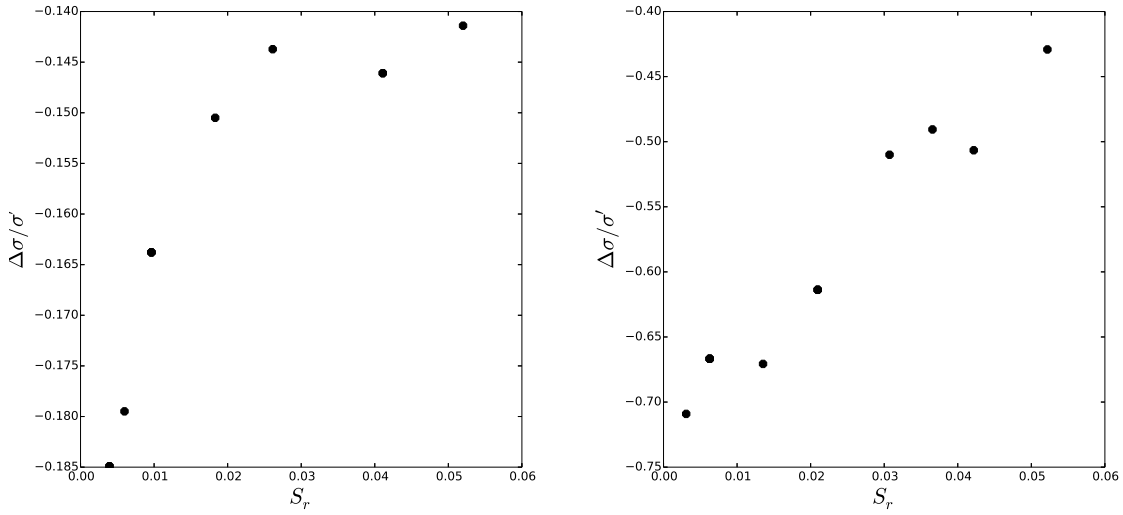

(a) (b)

Figure 4.4 The variation of the difference between effective and contact stress with the degree of saturation in pendular regime for (a)dense packing and (b)loose packing

tances separating the grains in the packing stay in the range where the forces and interfacial energies are the same for grains moving at constant suction or constant volume.

The difference between the contact stress and effective stress can be explained by the force distribution inside the sample in the presence of water. Probability density functions (PDF) of normal and shear forces normalized by the average normal force in the dry case are plotted in figure 4.6 for both dry and wet dense samples ($n = 0.37$). The plots of PDF for dry packing are in agreement with the results of [69]. The shape of the curve is characterized by an exponential falloff for large forces:

$$PDF = e^{-\beta f_n/<f_n>} \tag{4.14}$$

$Log(PDF)$ is then a linear function of $(f_n/ < f_n >)$ for large forces as shown in figure 4.5.

$$Log(PDF) = -\beta f_n/ < f_n > \tag{4.15}$$

β is equal to 0.75 in the dry sample and equal to 0.91 in the case of the wet sample.

If $\sigma_{cont} = \sigma'$, σ_{cont} should remain independent of the capillary forces added to the sample as long as no deformation occurs at the macro scale; but the PDF functions show that the

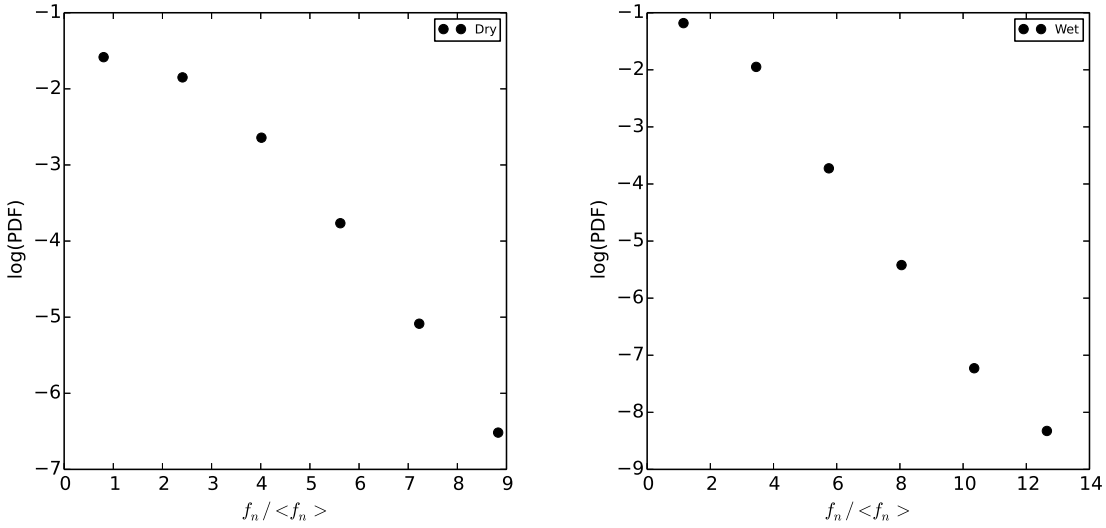

(a) (b)

Figure 4.5 The logarithmic distribution of the PDF of the normal forces for (a)-dry and (b)-wet dense samples.

presence of water bridges changes the distribution and the values of the forces which leads to a different value in the contact stress.

The normal forces are subjected to changes. We also observe a considerable increase in the value of the shear forces in the wet sample.

The change in the forces is accompanied by a change of the micro structure and thus in the displacements of the grains u while the total deformation is equal to 0. If we fix the macro deformation and we add the meniscii, local deformation occurs and the grains are rearranged which leads to a change of the contact stress (shear forces and normal forces) and of the elastic free energy. u is then not only function of deformation but also function of the suction p_c.

In dry conditions, the displacement u_k of a grain labeled k is only function of the total macro deformation, and the contact stress is equal to the derivative of elastic energy with respect to the macro deformation [14].

$$u_k = f_k(\varepsilon) \text{ for all } k, \tag{4.16}$$

hence

$$E_{el} = E_{el}(\varepsilon) \tag{4.17}$$

and

$$\sigma_{cont} = \frac{1}{V}\frac{dE_{el}}{d\varepsilon} \tag{4.18}$$

In unsaturated conditions, we show that the elastic energy is not only function of the deformation but also function of the distribution of phases and interfaces.

The results shown previously for the pendular regime and the PDF show that even if the macro deformation is equal to zero the capillary forces change the distribution of forces. The contact stress in the sample after the addition of menisci is not equal to the contact stress in the dry sample. As a consequence the contact stress does not reflect accurately the effective stress that control the deformation at macro scale.

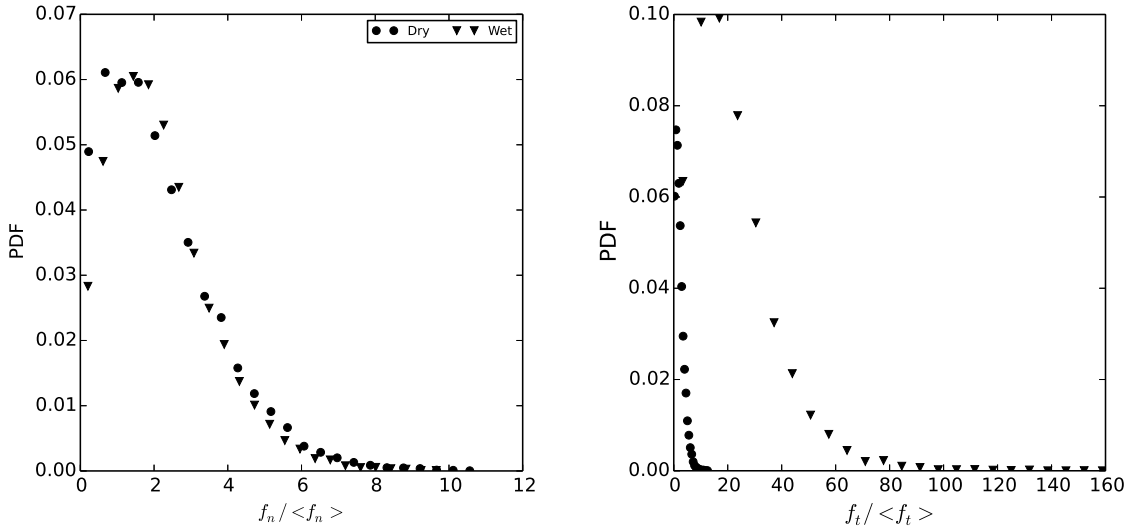

(a) (b)

Figure 4.6 The probability density functions of (a) normal forces and (b) shear forces in dry and wet dense samples .

4.3 Conclusion

This chapter has discussed the concept of effective stress in unsaturated soil in elastic conditions. It has been shown that the Love-Weber stress,though frequently supposed to play the role of effective stress in multiphase systems, is found to be valid only for regular packings. In random packings, it does not compare consistently with the changes of elastic free energy. This result is useful to reorient researchers that are trying to find a formulation of the effective stress using Love-Weber contact stress. The effective stress depends very much

of the amount of interfaces present in the medium and the distribution of all phases and interfaces in the sample.

Chapter 5

Roughness and particle size distribution effects on the shear strength properties of unsaturated granular material in the pendular regime

5.1 Introduction

Although defined by many as the micromechanical effective stress in unsaturated soils, it has been shown in the previous chapters that the averaged Love-Weber stress is not suitable to describe the deformation and behavior of unsaturated granular materials in the elastic regime. It is shown to be not equal to the effective stress defined through the change of the energy of deformation ($\sigma' = dE_{el}/d\varepsilon$).

There are cases, however, where this assumption is valid. If we review the results of [74], this averaged contact stress seems to be a good approximation and describes well the behavior of unsaturated soils at the peak for shear strength.

It has been shown in [74] that when the rupture states for various saturation and for the dry granular sample are plotted in the (p_{cont}, q_{cont}) plane, we obtain a unique Mohr-Coulomb envelop (figure 5.1). Hence the contact stress can be defined as a possible micromechanical effective stress formula with respect to shear strength.

This result is only valid at the peak for the shear strength and the results of [74] were

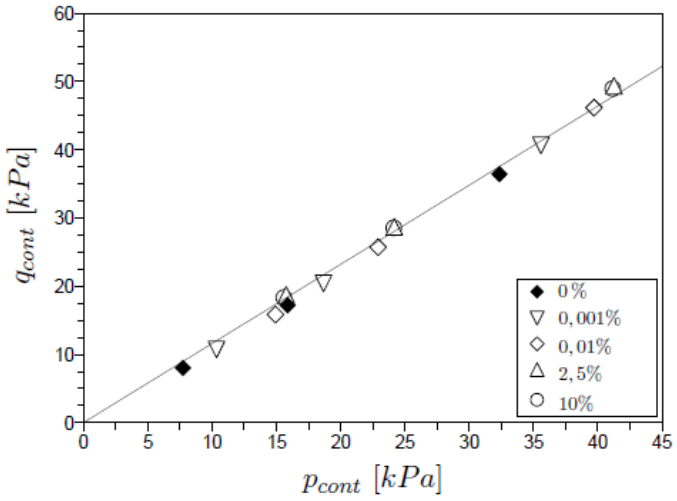

Figure 5.1 Unique rupture envelop obtained by the intergranular contact stress for various saturations from [74]

tested for smooth grains and in the case of tightly graded particle size distributions.

In this chapter, the validity of this assumption is the case of rough grains and different particle size distributions is discussed, and the influence of these parameters on the shear strength and the capillary stress is evaluated.

5.2 The roughness of the grains

To test the effect of the roughness of the grains, triaxial shear tests are performed on a sample of 10000 spherical grains of tightly graded particle size distribution (the dispersion from the mean radius is 1 %). The tests are repeated for various saturations and several values of initial isotropic confinement pressure in order to plot the Mohr-Coulomb envelop for different values of roughness ($\kappa = 0, -1$ and 2 %).

The results show that the Mohr-Coulomb criterion is verified, with a friction angle around 28 degrees (figure 5.2).

When plotted in the (p, q), the effect of the roughness is visible (figure 5.2). The presence of grains with positive roughness decreases the shear strength of unsaturated materials in pendular regime and negative roughness values lead to an increase in the shear strength value of these materials.

This result is consistent with the observations of the evolution of the capillary force with the roughness in chapter 2(figure 5.3). For the same suction value, for grains in contact, the force in the case of negative roughness is higher than the force for two smooth grains that is higher than the force in the case of positive roughness. This difference increases with the increase of suction.

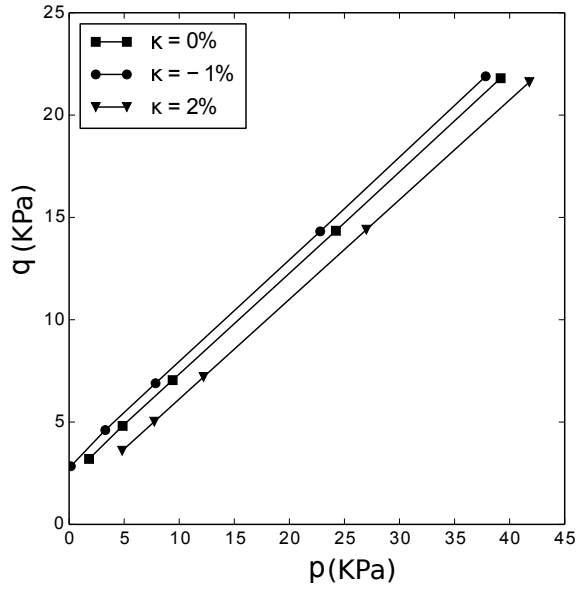

Figure 5.2 Mohr-Coulomb envelops for different roughness values ($\kappa = 0, -1, 2$ %) for $S_r = 0.01$

Mohr-Coulomb envelops are plotted in figure 5.4 for different saturation values to evaluate the evolution of the cohesion with the saturation for $\kappa = 0, -1$ and 2 % (figure 5.5).

The plot of the cohesion (figure 5.5) for smooth grains is consistent with the results of [71]. The cohesion increases with the saturation and then reaches a constant maximum value for a saturation of 3%.

The plot of the cohesion follows the same trend for a positive roughness but the value of the cohesion is lower and the change with the saturation is more important than in the case of smooth grains. The results in the case of negative roughness are completely different. The cohesion decreases with the increase of the saturation and reaches a minimum value afterwards for a saturation around 4%. The minimum value remains higher than the maxi-

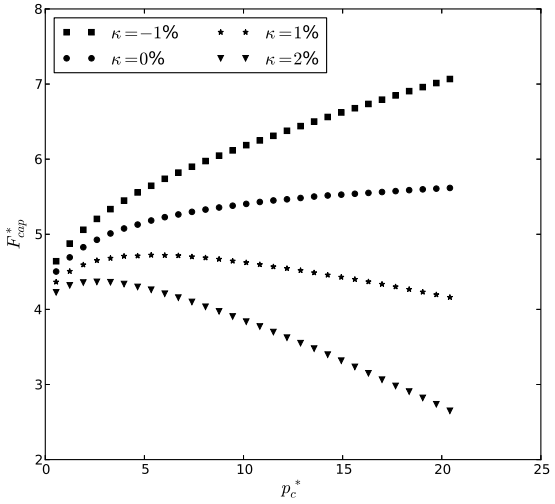

Figure 5.3 The evolution of the force with the suction for various roughness values ($\kappa = 0, -1, 2$ %) in the case 2 grains in contact.

mum value for smooth grains.

Several works like [71] proposed analytic formula of the cohesion in partially saturated media in the pendular regime. This allows to track the evolution of the shear strength in unsaturated granular materials for various degrees of saturation.

Another and a simpler way to track the evolution of shear strength in unsaturated granular materials is to determine the evolution of $q_{cap} = (\sigma_{cap,1} - \sigma_{cap,3})/2$ and $p_{cap} = (\sigma_{cap,1} + \sigma_{cap,2} + \sigma_{cap,3})/3$ with the saturation. Knowing both values the cohesion can be deduced.

q_{cap} is plotted as function of p_{cap} for various roughness values in figure 5.6. The results show that q_{cap} is a linear function of p_{cap}.

We notice that the evolution of p_{cap} with the saturation in the case of smooth grains is small since the capillary forces remain almost constant for grains in contact with the change of the suction and 85 % of the menisci in the assembly are formed between grains in contact. The evolution of p_{cap} and q_{cap} with the saturation is much more important for rough grains.

In order to test the validity of the results obtained by [74] for rough grains, stating that the Love-Weber stress can be considered as a micromechanical definition of the effective stress, the Mohr-Coulomb envelop for the tests performed above on wet samples for different roughness values are plotted in the (q_{cont}, p_{cont}) plane together with a test performed in dry conditions in figure 5.7.

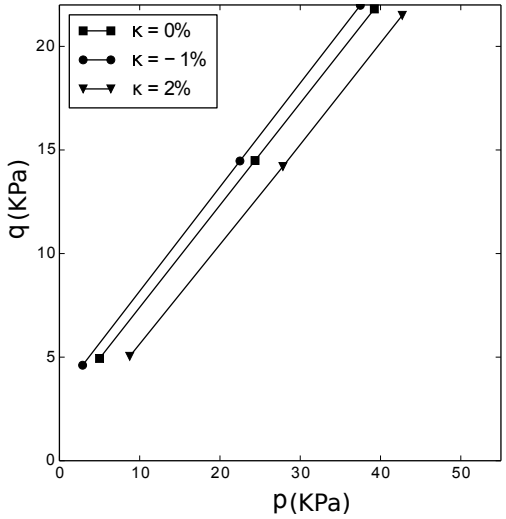

(a) $S_r = 0.004$

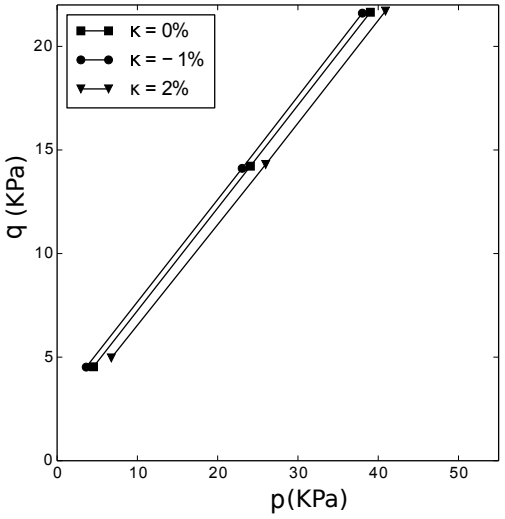

(b) $S_r = 0.02$

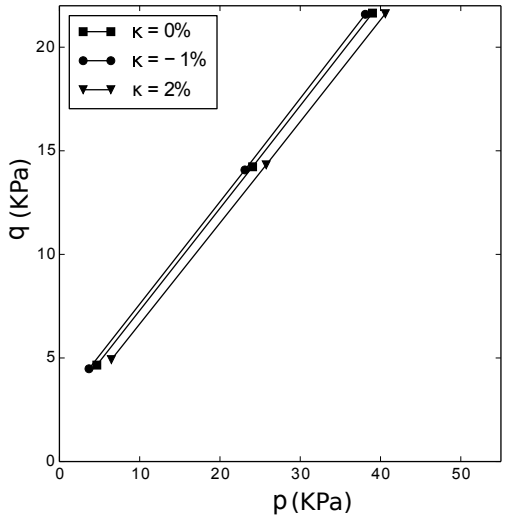

(c) $S_r = 0.03$

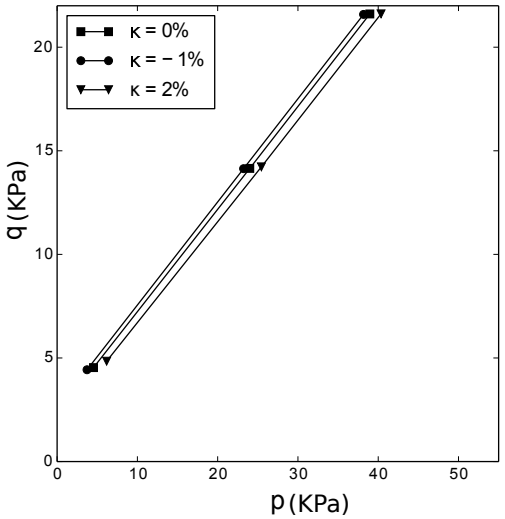

(d) $S_r = 0.045$

Figure 5.4 Mohr-Coulomb envelops for different roughness values for various degrees of saturation

These results show that a unique Mohr-Coulomb is obtained for κ=0,-1 and 2 %, which validate the validity of the averaged intergranular contact stress to describe the behavior of an assembly of rough grains at the peak for shear strength.

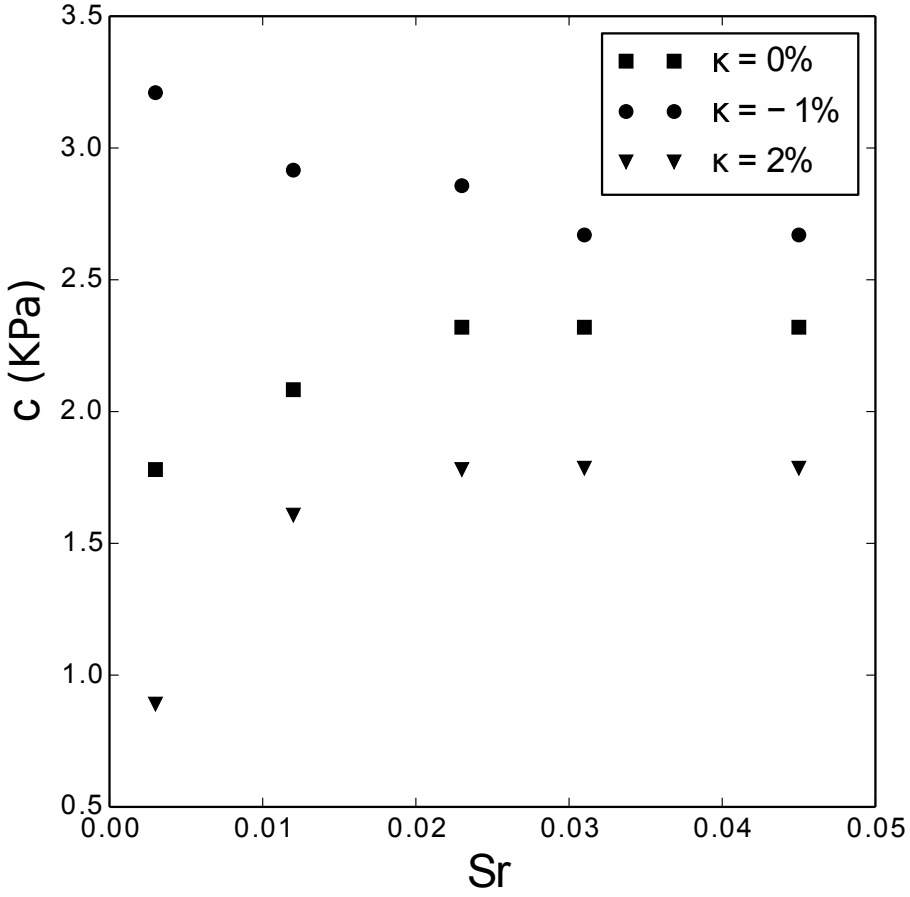

Figure 5.5 The evolution of the cohesion with the saturation for various roughness values ($\kappa = 0, -1, 2$ %)

5.3 The particle size distribution of the grains

This section investigates the influence of the particle size distribution on the capillary stress and the shear strength in unsaturated conditions.

The particle size distribution of the numerical samples is taken into account by mixing two populations of grains of different radii (R_1 and R_2 with $R_2 > R_1$) in different cumulative frequency p_p. The granulometric curve is presented in figure 5.8.

Triaxial shear tests are performed on wet samples for various proportions (p_p)and $r = (R_1/R_2)$ values. We select the values 0,0.3,0.5,0.7 and 1 for p_p and r.

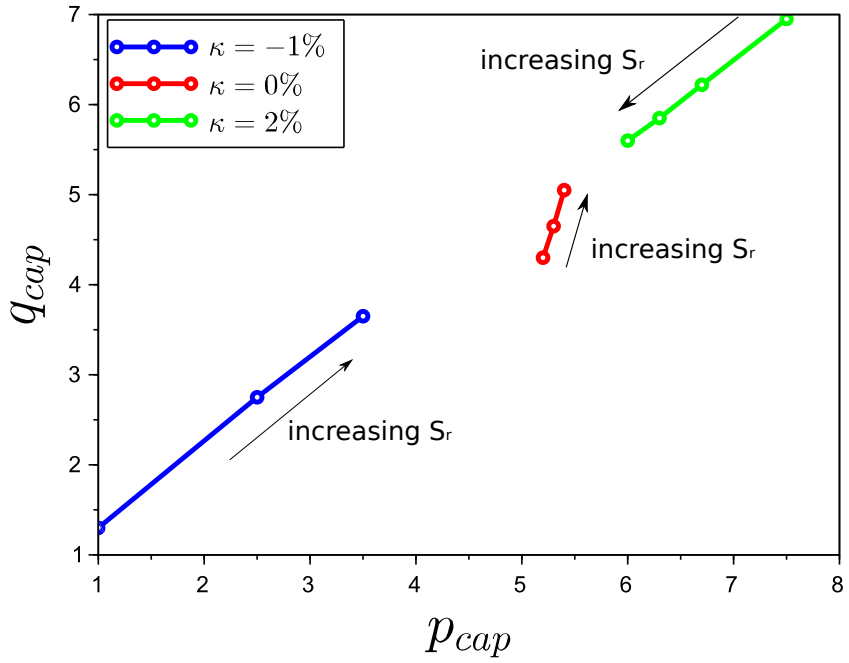

Figure 5.6 q_{cap} plotted as function of p_{cap} for different roughness values ($\kappa = 0, -1, 2$ %).

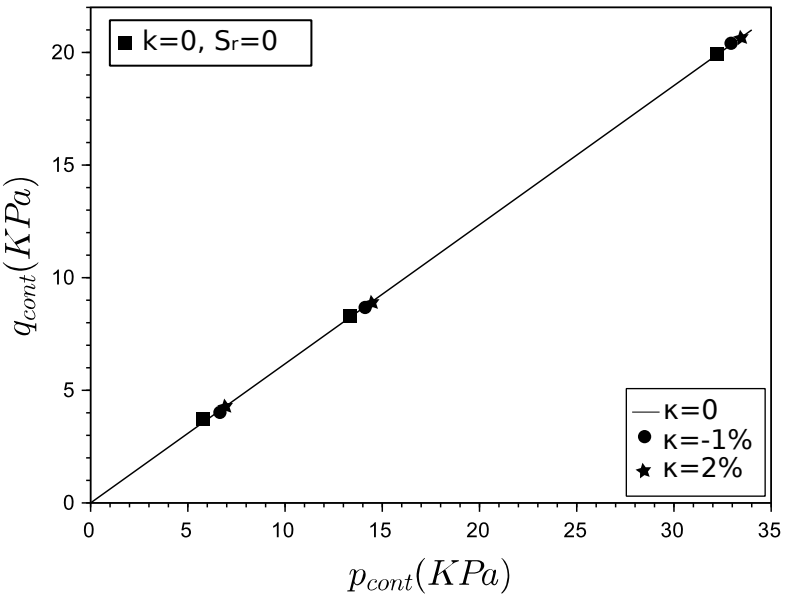

Figure 5.7 Unique rupture envelop obtained by the intergranular contact stress for various roughness values ($\kappa = 0, -1, 2$ %).

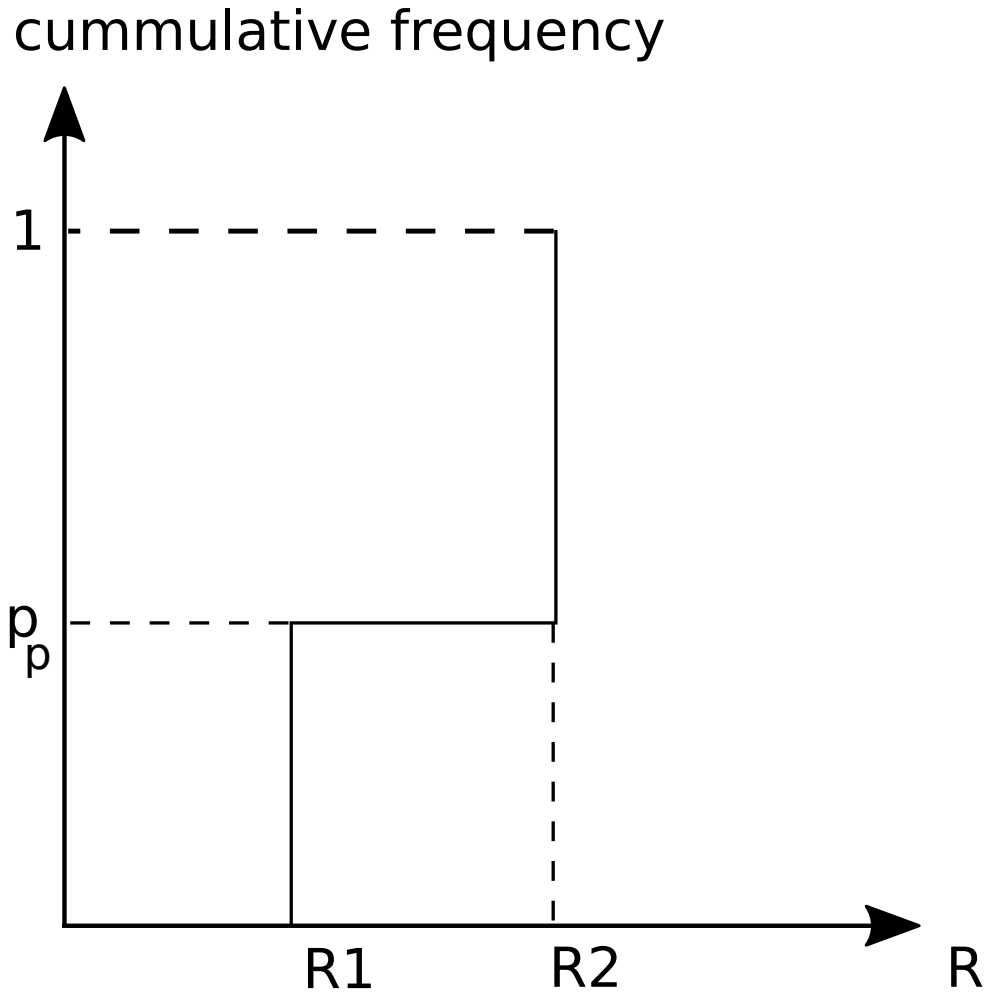

Figure 5.8 The granulometric curve as taken into account in the DEM simulations.

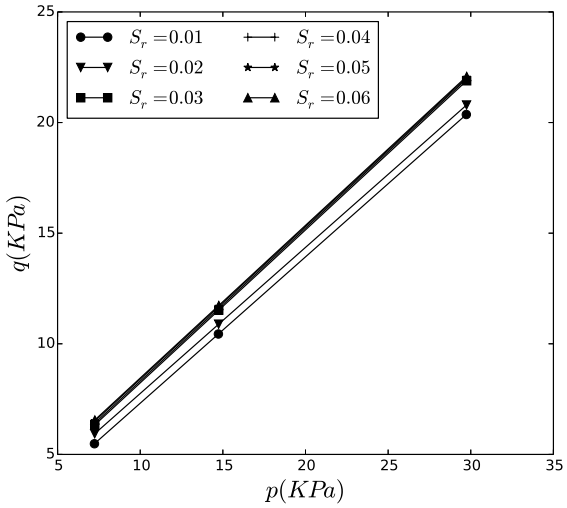

(a) $p_p = 0.3$

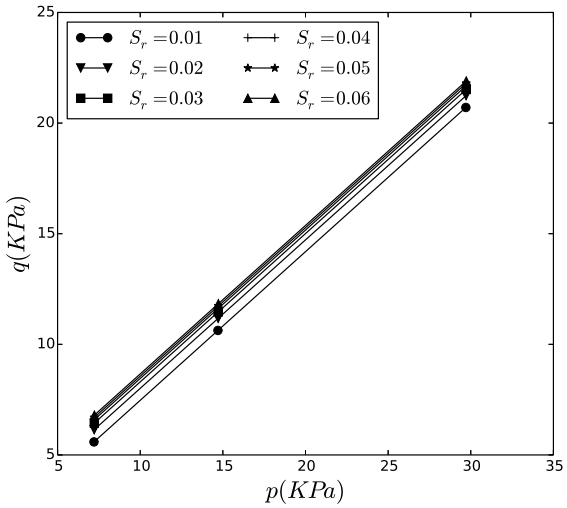

(b) $p_p = 0.5$

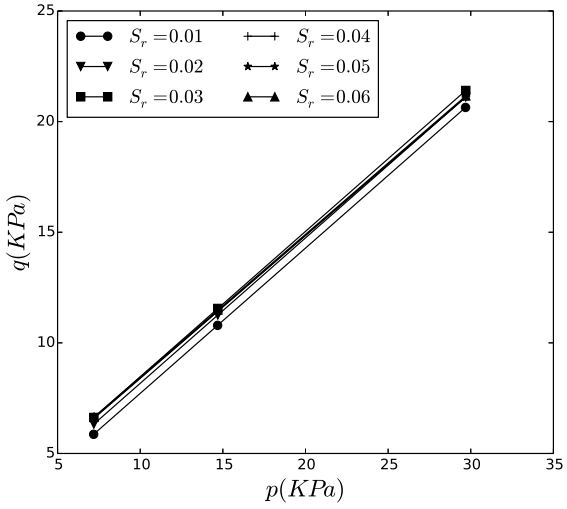

(c) $p_p = 0.7$

Figure 5.9 Mohr-Coulomb envelops for different saturation and different p_p values (r=0.5).

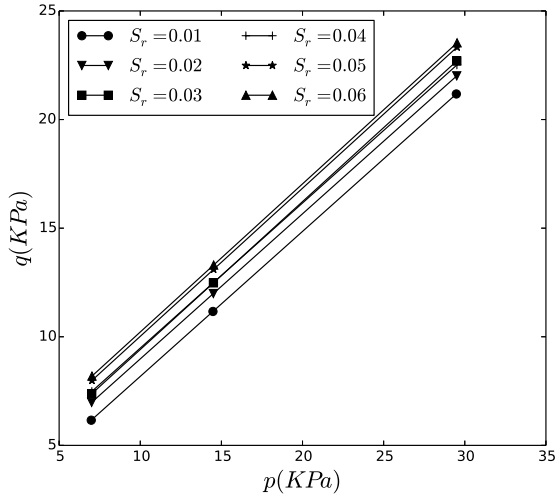

(a) $r = 0.3$

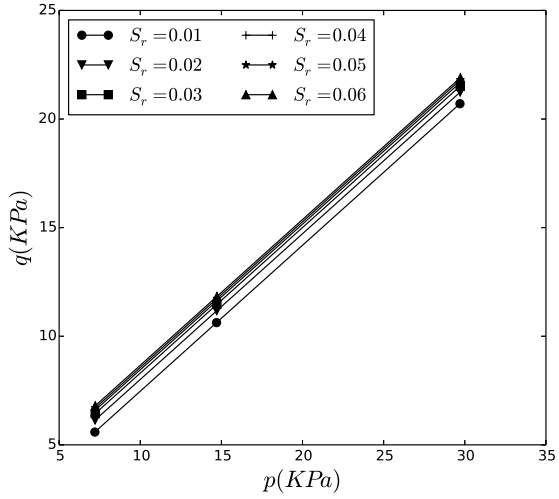

(b) $r = 0.5$

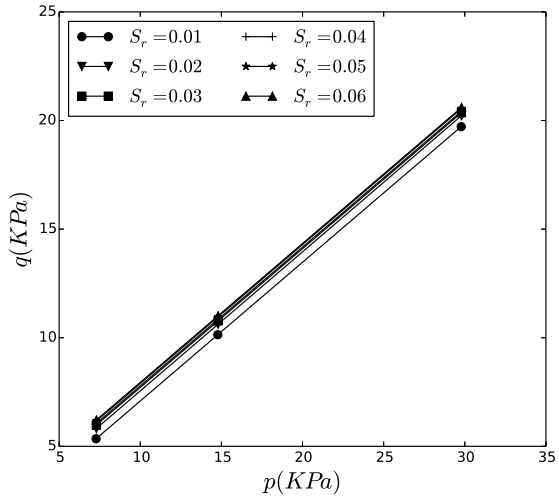

(c) $r = 0.7$

Figure 5.10 Mohr-Coulomb envelops for different saturation and different r values ($p_p = 0.5$).

The capillary effects on the shear strength of the materials for various p_p and r values are studied for various degrees of saturation. These results are presented in terms of cohesion. The Mohr-Coulomb rupture envelops are plotted for different values of saturation and the value of the cohesion is determined. The Mohr-Coulomb envelops for the simulated tests are presented in figures 5.9 and 5.10.

Figure 5.11 shows the evolution of the cohesion for different p_p values when r=0.5. The values of the cohesion for various p_p values vary always between two extreme values: the cohesion values for p_p=0 corresponding to uniform particle size distribution (PSD) of radii R_2 and p_p=1 corresponding to uniform PSD of radii R_1. The cohesion is inversely proportional to the radius of the grains. The value of the cohesion for p_p=0 is then directly proportional to the value of cohesion for p_p=1: $c_{(p_p=0)} \propto \frac{R_2}{R_1} c_{(p_p=1)}$. When the normalized cohesion $c^* = cR_m/\gamma_{wn}$ is plotted in figure 5.13, R_m being the mean radius :$R_m = (R_1 + R_2)/2$, the result show that for the uniform assemblies, the normalized cohesion is the same.

When p_p increases, the number of small particles of radii R_1 increases and the value of the cohesion increases to approach the cohesion of the uniform packing of small particles for p_p=1.

When $p_p = 0.7$ (the sample contains 70% of particles of small radii R_1), the cohesion still follows the same trend of the cohesion for uniform particle size distribution, the value of the cohesion increases with the saturation and stabilizes for $S_r = 0.03$.

When the percentage of big grains increases to p_p=0.5, the evolution of the cohesion does not stabilizes for higher saturation values but continues to increase.

This increase can be explained by the fact that, when we have two populations of grains of different radii, new menisci keep forming between the grains with the increase of the saturation, mainly between grains of different radii, while in the case of uniform PSD, the number of menisci almost stabilizes after 3%.

When p_p decreases again to 0.3, the proportion of small grains is 30 %. The value of the cohesion follows the same trend of the cohesion as for $p_p = 0.5$, but tends to stabilize faster for high degrees of saturation since it approaches more the cohesion of the uniform packing with big grains.

The evolution of the cohesion is also studied for various grain size ratio (figure 5.12). p_p is fixed to 0.5.

The values of the cohesion in this case vary also between two extreme values: the cohesion values for the uniform PSD of radii R_2 and the uniform PSD of radii $0.3R_2$. When

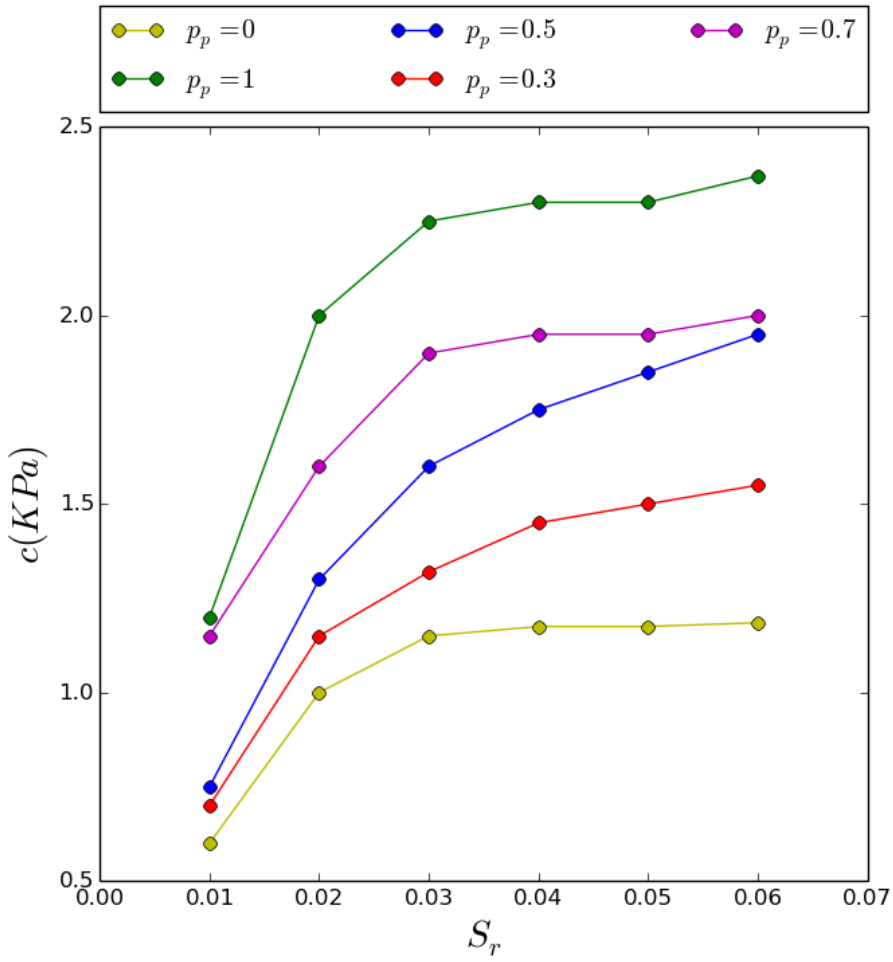

Figure 5.11 The cohesion as function of the degree of saturation for various p_p values (r=0.5).

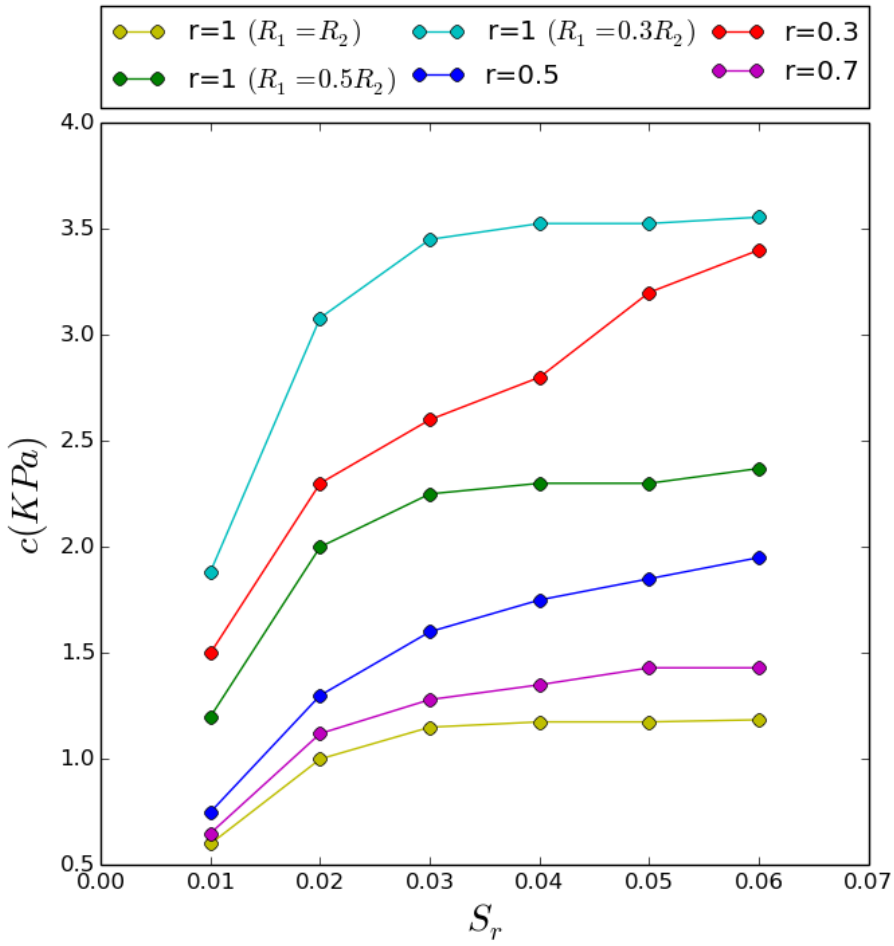

Figure 5.12 The cohesion as function of the degree of saturation for various r values (p_p=0.5).

$r = 0.7$ the particle size distribution is tightly graded and the cohesion still follows the same trend of the cohesion in the case of uniform particle. Once the gap between the grain sizes gets bigger, the trends vary and the cohesion keeps increasing for higher degrees of saturation.

Plotted as function of p_{cap}, (q_{cap}) is linear function of p_{cap} as well for various particle size distributions (figure 5.14).

5.3.1 Influence of the particle size distribution on the friction angle.

The particle size distribution has also an impact on friction angle of the sample . Mohr-Coulomb envelops for various p_p values and r values are compared and are plotted in figures 5.16 and 5.17.

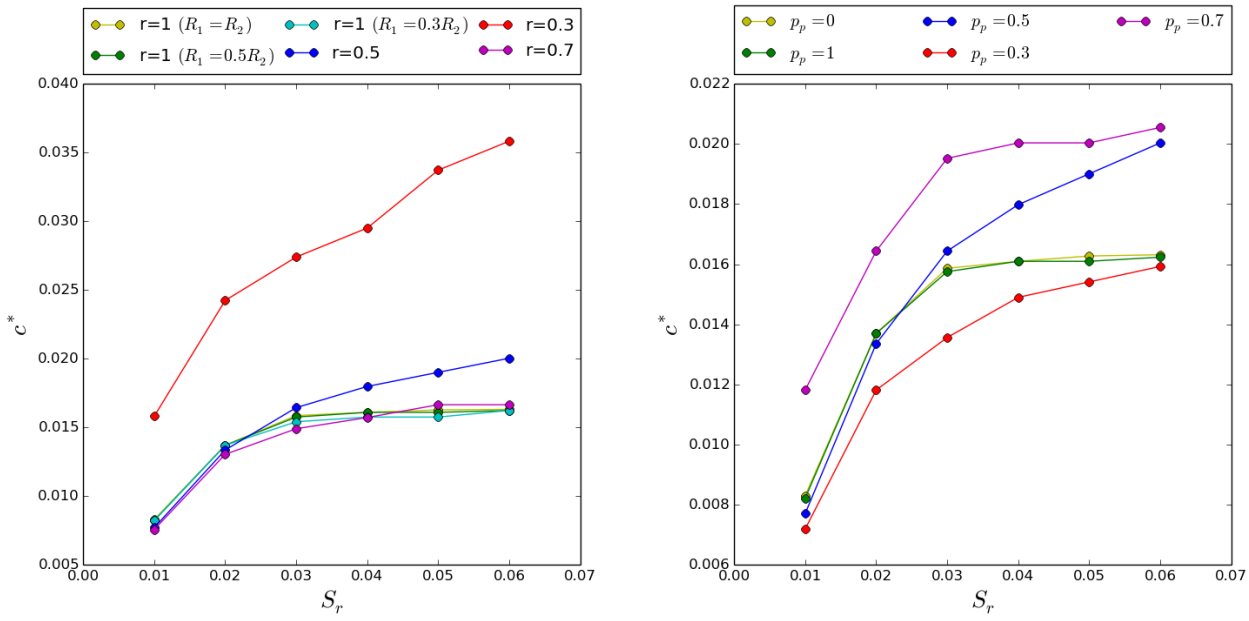

(a) (b)

Figure 5.13 The normalized cohesion as function of the degree of saturation for various (a) r (p_p=0.5) and (b) p values (r=0.5).

We observe that when the value of p_p decreases, the friction increases. From the other hand, higher this ratio $r = R_1/R_2$ is, lower is the friction angle. We also observe that the ratio r has a bigger influence on the friction angle.

5.3.2 Contact Stress vs Effective Stress

We verify again in this section if the averaged contact stress calculated through Love-Weber equation is valid to describe the behavior of partially saturated granular material at the pic for shear strength.

Mohr-Coulomb are plotted in the (p_{cont}, q_{cont}) plane. Figure 5.18 shows that we still obtain a unique envelop for dry and wet materials in the case of $p_p = 0.5$ for r= 0.3,0.5 and 0.7. When the value of r is fixed to 0.5 and the cumulative frequency of grains is changed, a unique envelop is obtained when p_p is equal to 0.5 and 0.7. When p_p=0.3, this condition is not verified anymore(figure 5.19). When the radius of small grains decreases to $r = 0.3$ ($p_p = 0.3$), this condition is not verified as well (figure 5.20).

A unique Mohr-Coulomb criterion is not obtained when the rupture envelops are plotted in (p_{cont}, q_{cont}) plane, then, the Love-Weber stress is not valid in this case to describe the

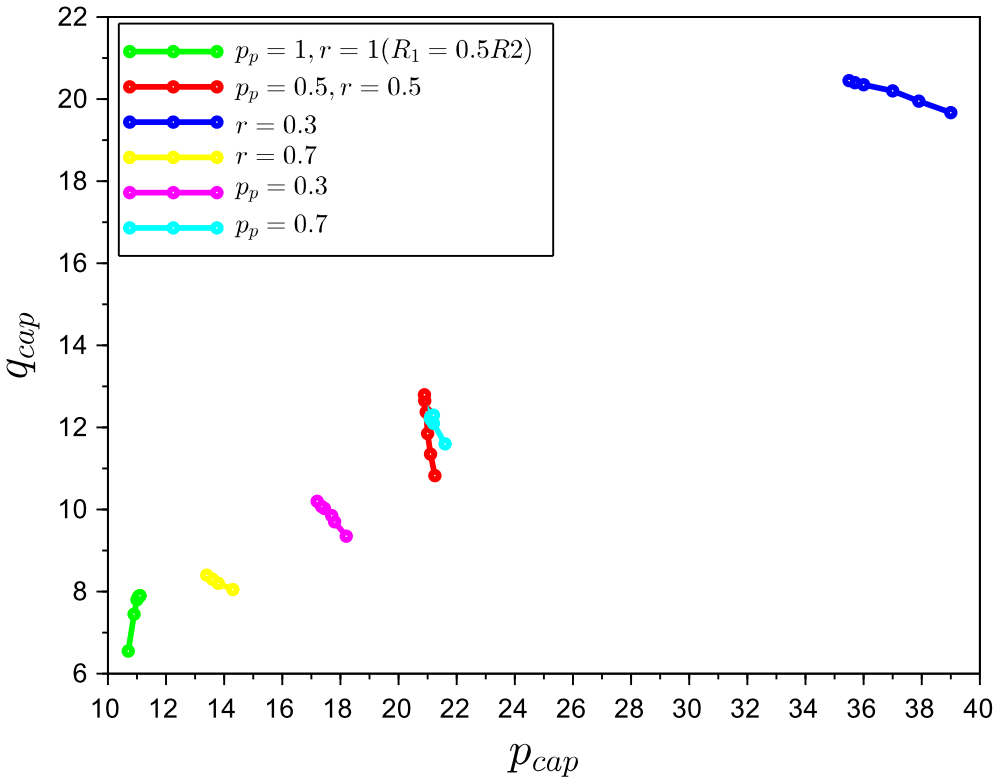

Figure 5.14 The deviatoric capillary stress q_{cap} plotted as function of the mean capillary stress p_{cap} for different particle size distributions.

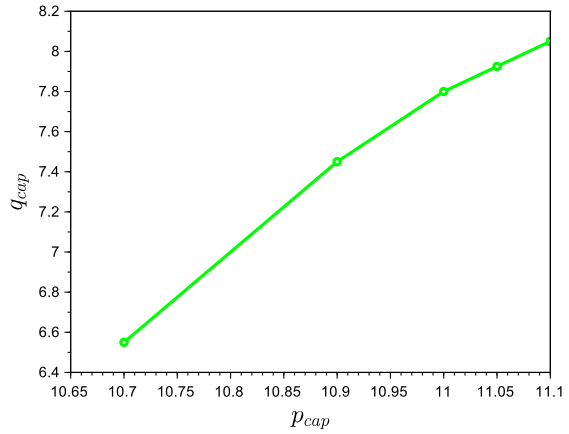

(a) $r = 1$

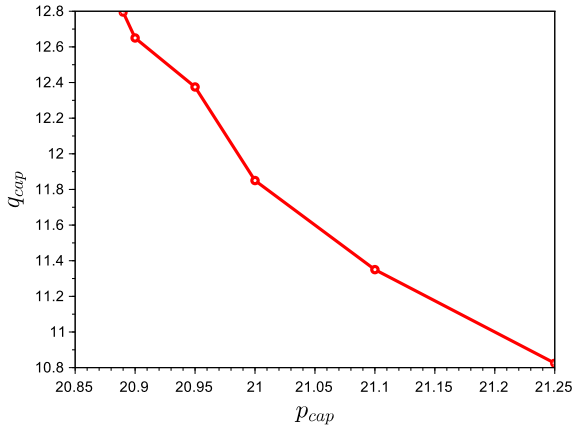

(b) $p_p = 0.5, r = 0.5$

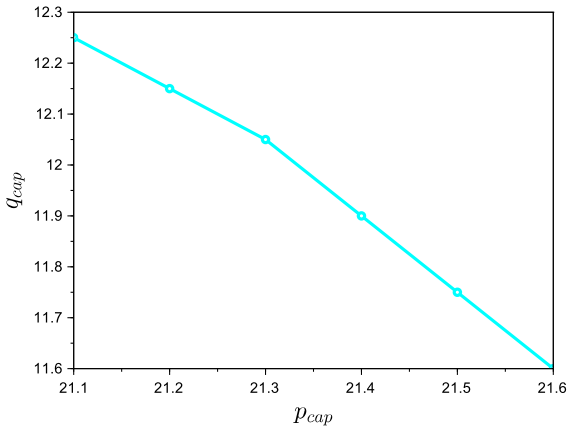

(c) $p_p = 0.7, r = 0.5$

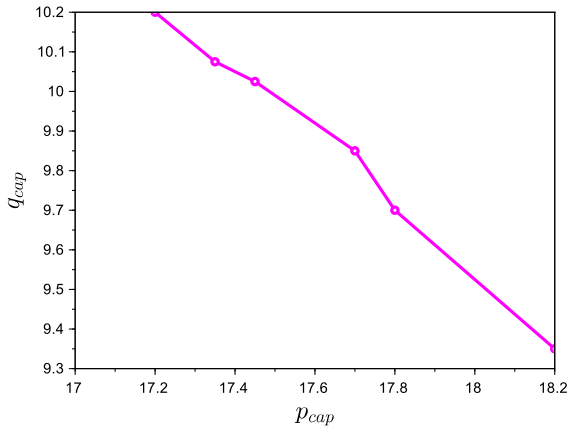

(d) $p_p = 0.3, r = 0.5$

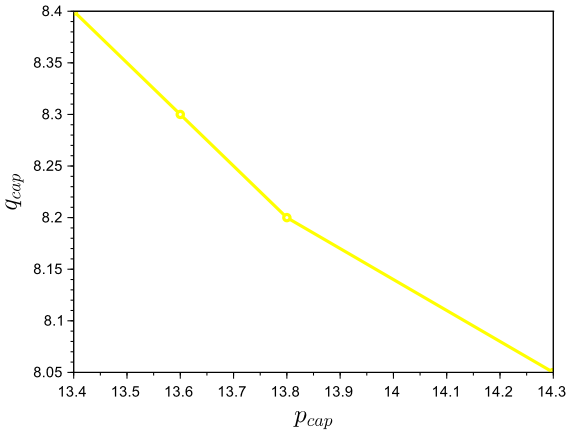

(e) $r = 0.7, p_p = 0.5$

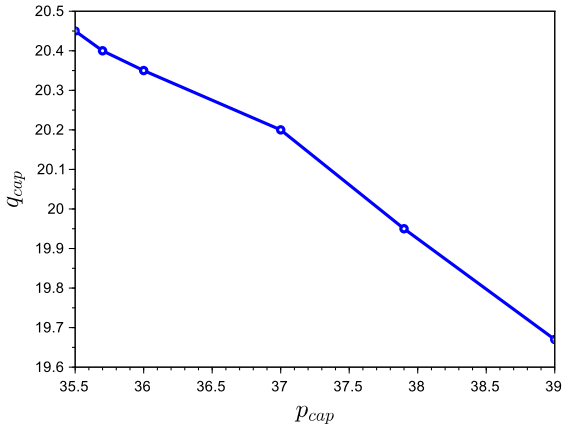

(f) $r = 0.3, p_p = 0.5$

Figure 5.15 The deviatoric capillary stress q_{cap} plotted as function of the mean capillary stress p_{cap} for different particle size distributions.

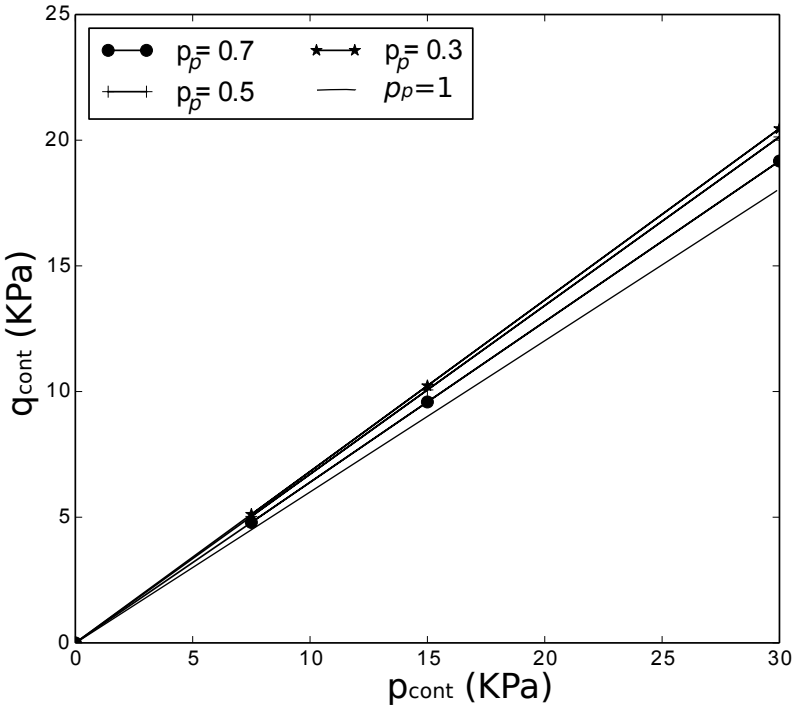

Figure 5.16 Mohr-Coulomb envelops of dry materials for $p_p = 0.3, 0.5$ and 0.7 ($r = 0.5$)

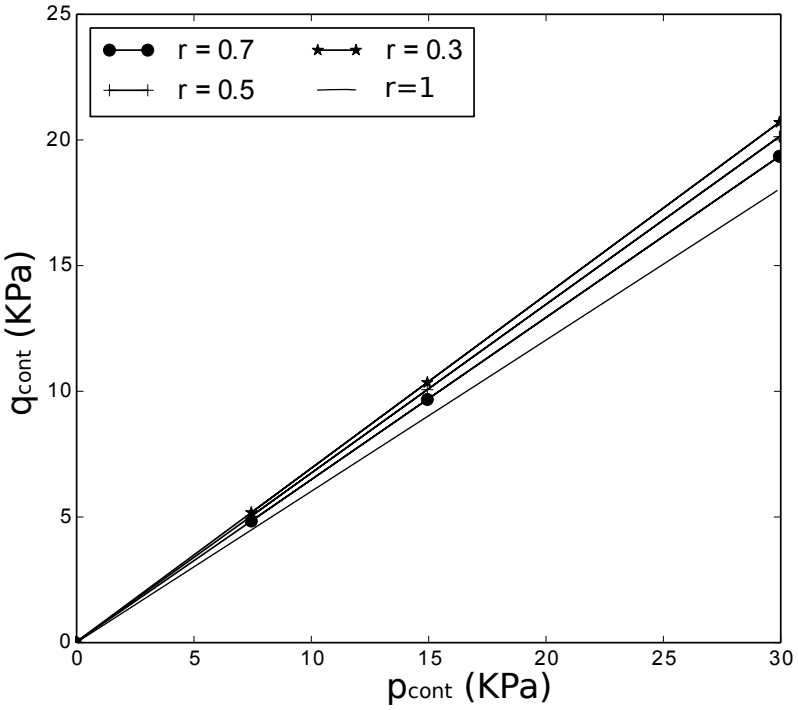

Figure 5.17 Mohr-Coulomb envelops of dry materials for $r = 0.3, 0.5$ and 0.7 ($p_p = 0.5$)

behavior of soil at rupture for shear strength.

In fact, in this case, the percentage of small grains is small and the ratio r is not big as well; the mechanical behavior is dictated by the big grains since the small grains occupy mainly the pores between the big grains, while menisci form between all the grains (small/small, small/big and big/big). During shearing, the menisci break mostly between the big grains, while the number of menisci formed between the small grains and between the grains that are small and big remain almost constant. The cohesion is then quite small compared to the value of the mean capillary stress, which makes the Mohr-Coulomb envelops of wet sample plotted in (p_{cont}, q_{cont}) different from the one of dry sample.

5.4 Conclusion

The capillary stress is found in this chapter to reflect the contribution of the capillary forces to the shear strength rather accurately in many cases, which suggest a generalization of the property found by [74]. On the other hand, we found some cases in which the (q_{cont}, p_{cont}) pairs deviate significantly from the reference (cohesionless) line. The mismatch is sufficiently large to discard the numerical errors as unique explanation.

This chapter showed that the failure of contact stress to define accurately the effective stress is not limited to the elastic behavior. With particular settings, it also fails to reflect the evolution of the shear strength. Clearly, the invariance of the constitutive relations based on the contact stress cannot be taken for granted a priori for any type of material. Unfortunately, it eliminates the opportunity to predict the mechanical response of a generic material simply by examining the distribution of pendular bridges and the associated capillary stress.

It has been also found in this chapter that the relationship between (q_{cap}, p_{cap}) is a linear relationship, which can help establishing an analytic expression of q_{cap} and p_{cap} in order to determine the shear strength and the cohesion in partially saturated conditions.

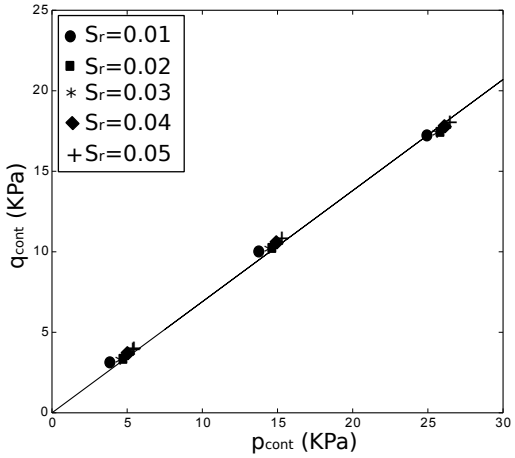

(a) $r = 0.3$

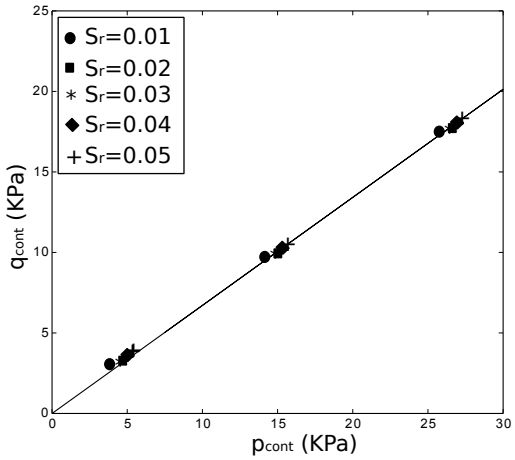

(b) $r = 0.5$

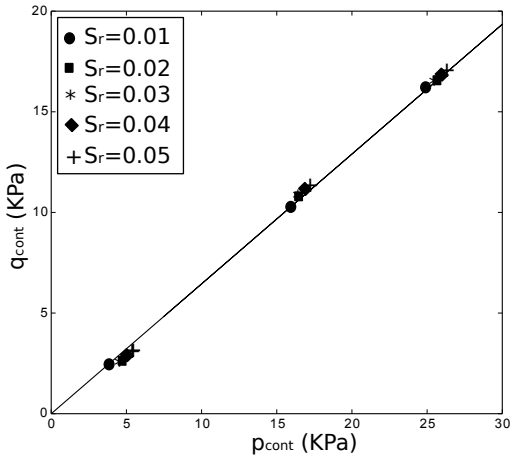

(c) $r = 0.7$

Figure 5.18 Mohr-Coulomb envelop plotted in (p_{cont}, q_{cont}) for a sample with $r = 0.3, 0.5, 0.7$ and $p_p = 0.5$

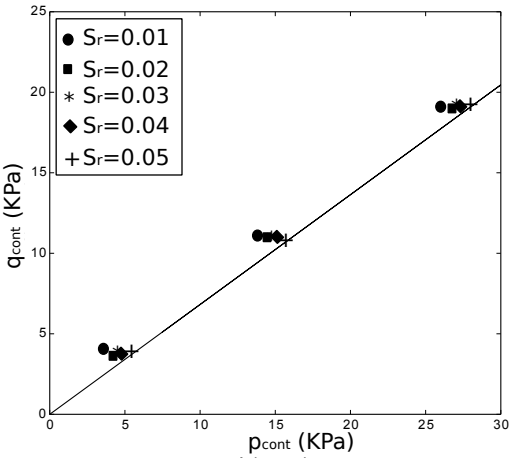

(a) $p_p = 0.3$

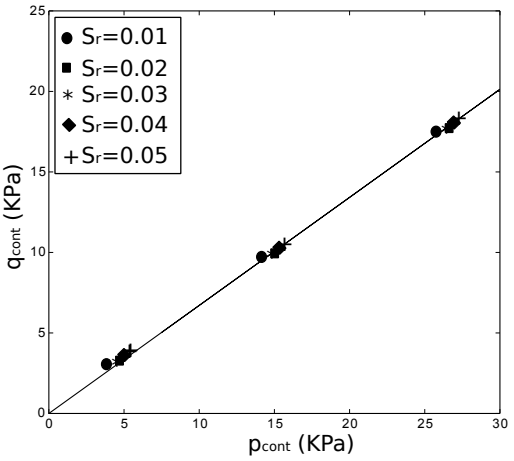

(b) $p_p = 0.5$

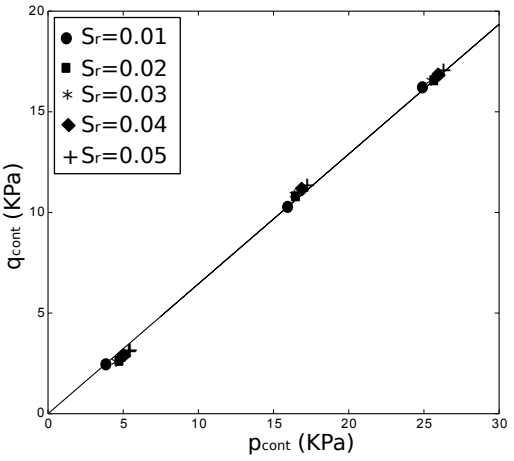

(c) $p_p = 0.7$

Figure 5.19 Mohr-Coulomb envelop plotted in (p_{cont}, q_{cont}) for a sample with $r = 0.5$ and $p_p = 0.3, 0.5, 0.7$

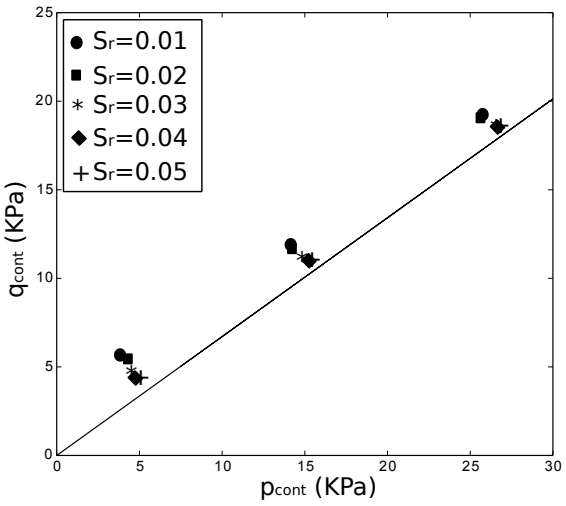

Figure 5.20 Mohr-Coulomb envelop plotted in (p_{cont}, q_{cont}) for a sample with $r = 0.3$ and $p_p = 0.3$

Chapter 6

Pore-scale simulation of drainage in granular materials: Passage from saturated to funicular to pendular regimes

6.1 Introduction

This work is in Collaboration with Chao Yuan. In this chapter the DEM-PFV model for the funicular regime introduced by Chao Yuan is combined with the pendular model, to simulate a complete quasi-static drainage process in granular materials.

When a fully saturated granular space is drained, it doesn't necessarily become fully dry when the drainage is over. Water can be kept trapped in the body pores and meniscii are left between the grains as well. The DEM-PFV model introduced by [94], is able to simulate a drainage process based on the Mayer and Stowe-Princen theory of drainage [46]. The left over menisci are added by the pendular model introduced by the author.

The influence of the additional menisci on the hydraulic and mechanical behavior of unsaturated soils is investigated and presented in this chapter.

The influence of the menisci presence on the water retention curves is presented in the first part and the comparison with the pendular model alone in terms of number and distribution of menisci is done and some assumption made at the pendular model are questioned.

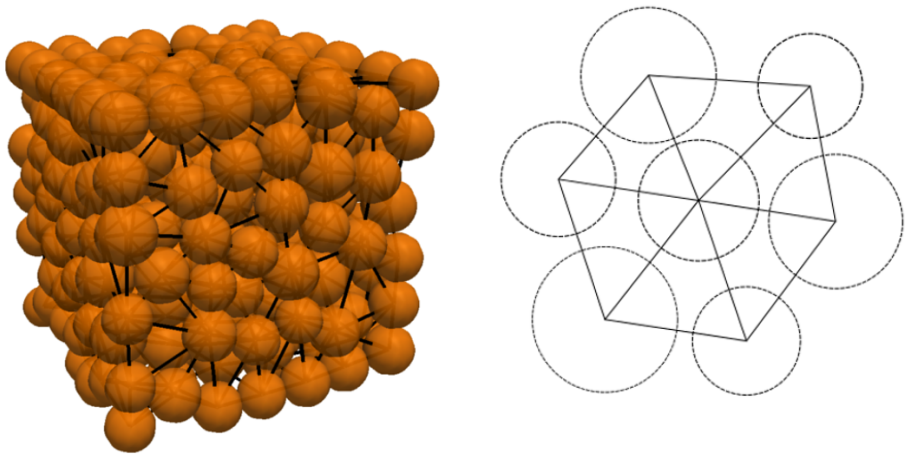

(a) 3D (b) 2D

Figure 6.1 Definition of the pore network generated by regular triangulation in 3D and 2D

The coupled DEM-PFV model is also used to predict the solid deformation in dense and loose porous medium. The drainage occurs under oedometric conditions. The deformation is then allowed in one direction. The relationship strain-saturation-capillary pressure is presented, and compared in both funicular and funicular+pendular cases in the rest of the chapter.

The effective stress parameter is also derived from microscopic and macroscopic views, and the influence of the addition of the menisci to the sample on that is presented.

6.2 DEM-PFV model

This section is a summary of the DEM-PFV model developed by Chao Yuan.

Considering a packing of polydisperse random packing generated by YADE, the pore space in the DEM-PFV model is decomposed in three dimensional space using regular triangulation implemented in YADE using CGAL libraries. Regular triangulation generalizes the Delaunay triangulation to weighted points where the weights account for the radii of the particles. Each pore space is then an irregular cavity within tetrahedron shape. The facets of the tetrahedron represent the pore throat and do not enclose any volume (interfaces).

The model follows the same hydraulic assumptions used in the pendular model implemented by the author in YADE. It assumes perfect wetting conditions. The gravity and the

viscous effects are also neglected. This implies also that the fluid pressure is uniform in the connected domains.

6.2.1 Drainage

The drainage is controlled by the capillary pressure ($p_c = p_n - p_w$). The drainage occur by increasing p_c: the fluid pressure p_w decreases and the non-wetting phase pressure p_n is kept constant.

The invasion of the pore by the non-wetting phase occurs when the imposed value of capillary pressure is higher than the capillary pressure associated to the pore throat p_c^e.

$$p_c > p_c^e \tag{6.1}$$

When the invasion starts, the saturation of the pore is binary: either fully dry or fully saturated.

The first pore throat subjected to invasion is the throat with the lowest p_c^e.

The capillary pressure at pore throat is determined using Young-Laplace equation:

$$p_c^e = \frac{\gamma_{wn}}{r_c} \tag{6.2}$$

with r_c the curvature of the wetting-non wetting interface. r_c is determined using Mayer-Stowe-Princen method in which the balance of forces on the wetting-non wetting interface is written in the unstable state:

$$F_p + F_\gamma = 0 \tag{6.3}$$

F_p and F_γ are the contributions of pressure and surface tension respectively in the total force applied on the wetting-non wetting interface:

$$F_p = p_c^e * A_{wn} \tag{6.4}$$

A_{wn} is the area of the wetting-non wetting interface.

$$F_\gamma = L_{sn}\gamma_{sn} + L_{wn}\gamma_{wn} + L_{sw}\gamma_{sw} \tag{6.5}$$

L_{wn}, L_{sw} and L_{sn} are respectively the length of the wetting-non wetting, solid-wetting and solid-non wetting contact lines.

The equilibrium at the contact line gives also a relationship between the three surface tensions. In perfect wetting conditions this relationship is:

$$\gamma_{wn} = \gamma_{sn} - \gamma_{sw} \tag{6.6}$$

The contribution of surface tension in the total force is then expressed as:

$$F_\gamma = (L_{sn} + L_{wn})\gamma_{wn} \tag{6.7}$$

The geometric properties and p_c^e can be expressed as function of r_c.

$$F_p(r_c) + F_\gamma(r_c) = 0 \tag{6.8}$$

Solving this equation determines the value of r_c. Once r_c is determined, p_c^e can be determined using the equation of Young-Laplace.

The invasion of the non wetting phase can occur successively in more than a connected pore for a single value of p_c depending on the value of p_c^e at the next throats. The value of the imposed p_c is increased only when equilibrium takes place in the sample, and no more invasions are possible.

During the drainage process, there is a possibility that the wetting phase form some disconnected clusters. The liquid trapped in these cluster is kept there. These clusters keep their p_c ultimately.

6.2.2 Forces on the particles

The total force F_k on the particle k by the wetting and non wetting phases includes the effects of the fluid pressures ($F_{p,k}$) and the effect of the surface tension($F_{\gamma,k}$).

$$F_k = F_{p,k} + F_{\gamma,k} \tag{6.9}$$

Each sphere can be either fully dry, fully wet or partially dry. The force acting on the particle due to the fluid pressures can be then written as follows:

$$F_{p,k} = \int_{S_{wet}} p_w \vec{n} ds + \int_{S_{dry}} p_n \vec{n} ds \tag{6.10}$$

Computing the integral on the spherical triangles S_{wet} and S_{dry} can be computationally

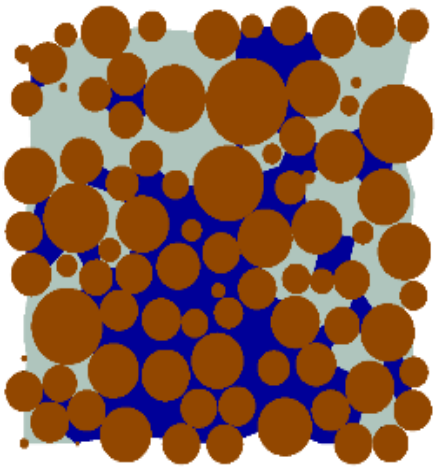

Figure 6.2 2D cut from the sample during the drainage process ($S_r = 0.23$).

expensive. The pressure is then projected on the planar parts of S_{wet} and S_{dry} corresponding to triangles $O_k O_{1k} O_{2k}$ and $O_k O_{2k} O_{3k}$ respectively in figure 6.3.

The surface tension contribution in the total force applied on the particle k is taken into account only when the particle contacts both wetting and non wetting phases (or in other terms is partially wet). The wetting-non wetting interface intersects 3 spheres. The total contribution of the surface tension $F_{\gamma,t}$ is calculated from the balance force of the wetting-non wetting interface in equilibrium.

$$F_p + F_{\gamma,t} = 0 \tag{6.11}$$

F_p can be easily estimated by projection on the facet S separating the wet and the dry pore.

$$F_p = A^*_{wn} * p_c = -F_{\gamma,t} \tag{6.12}$$

A^*_{wn} is only the fluid part of the projection of the wetting-non wetting interface on the facet S.

$F_{\gamma,t}$ is divided into 3 parts proportional to the length of the contact line with each of the spheres l_k.

$$F_{\gamma,k} = F_{\gamma,t} \frac{l_k}{\Sigma_1^3 l_k} \tag{6.13}$$

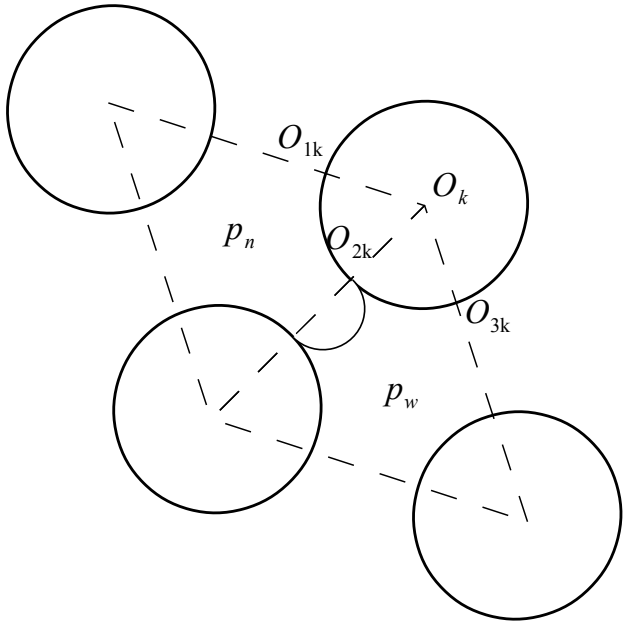

Figure 6.3 Two phase fluid pressure and the interfacial tension on the solid phase.

6.2.3 Stresses

The total stress in the DEM-PFV model is computed on the boundaries. It is equal to the sum of the averaged contact stress σ_{cont} and of fluid pressure on the boundary. Knowing the total stress at the boundaries and the contact stress calculated in the DEM code, σ_{fun} can be deduced.

$$\sigma_{fun} = (\sigma - p_n) - \sigma_{cont} \tag{6.14}$$

6.3 Pendular + Funicular model

During the drainage process, when the wetting phase leaves the pores, some water is left as form of clusters and menisci that form between particles that are distant or in contact.

The wetting phase does not leave the granular sample regularly but follows the geometry of the pore network. Besides, some water might be left trapped in some clusters during the invasion of the non wetting phase. Then, for each pair of grains (shared by several pores) in the sample, there is the possibility that it is fully wet, fully dry or partially wet.

The menisci form along the tetrahedron facet connecting the centers of the grain pairs. For the meniscus to form between two grains, the tetrahedron facet must be totally dry (figure 6.4).

For each value of imposed p_c, the sphere pairs connected by a dry tetrahedron facet in the triangulation are identified, and returned into a list employed by the pendular model to allow the formation of potential liquid bridges between these particles. If the distance between the grains is higher then the rupture distance, no meniscus will be formed (the interaction distance is set to twice the radii of the grains in these simulations to make sure that all possible menisci will form).

During the drainage process, two assumptions are possible:

- Connected phases (C): The menisci are all at equilibrium at the imposed pressure at the time: i.e. The menisci form at p_{c1} in the first step. When the pressure increases, the pre-existent menisci re-equilibrate at the new pressure value p_{c2}(the change of

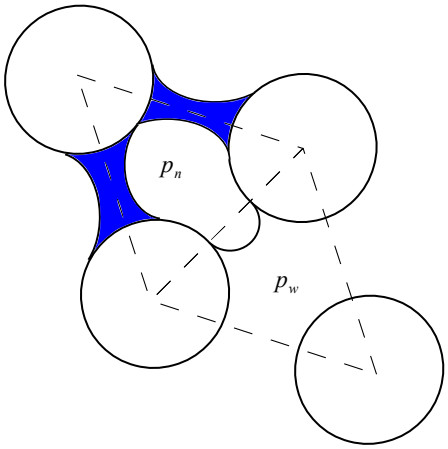

Figure 6.4 Menisci formed only along dry facets.

volume of menisci is possible in this case) and new ones are formed at the same suction(figure 6.5).

In this case, the grains are covered by a fluid film, and the drainage is sufficiently slow, the suction has the time to equilibrate in the sample, and the trapped liquid will find its path to drain out of the sample. No trapped clusters will form then and the suction is then at every step uniform all over the sample.

- Disconnected phases (DC): If the imposed suction is p_{c1} in the first step, menisci will form along the dry facets at the suction p_{c1}. These meniscii are disconnected and keep their volume constant for the rest of the drainage. In the next step, the pressure increases to p_{c2}. Only the new menisci form at the new pressure p_{c2} and so on (figure 6.5).

  This case corresponds to a drainage that is not enough slow to allow the suction to re-equilibrate in the sample. The wetting phase form clusters and menisci that keep their suction ultimately during the drainage process. The suction is then not uniform(wetting phase is trapped.).

The volume of the bridges and the forces applied on the particles are all calculated using

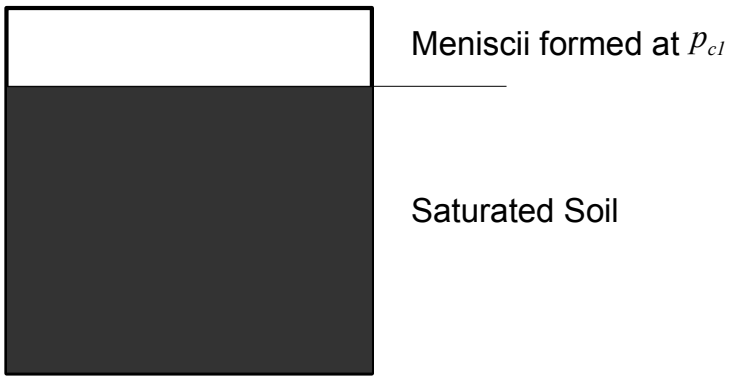

(a) Step 1

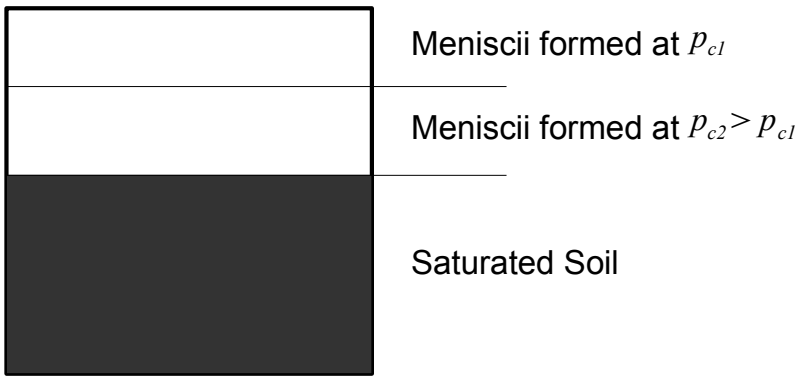

(b) Step 2 in the case of Disconnected phases

(c) Step 2 in the case of Connected phases

Figure 6.5 Simplified scheme for the addition of the meniscii in the case of connected and disconnected phases.

the pendular model as explained in chapter 2 following the exact solution of Young-Laplace equation, under the same assumptions of perfect wetting conditions and absence of gravity and viscous effects.

When the capillary bridges are added to the model, the total stress is equal to the sum of the contact stress, the funicular stress and the capillary stress.

σ_{cap} is calculated in the pendular model, hence σ_{fun} can be deduced.

$$\sigma_{fun} = (\sigma - p_n) - \sigma_{cont} - \sigma_{cap} \tag{6.15}$$

6.4 Sample Preparation

Dense and loose sphere packings of 40000 particles packed between rigid walls are used for the simulation of the drainage process. The particle size distribution for both packings is shown in table 8.1.

The initial porosity of the packing is controlled by an algorithm that can simulate the growth of spheres after random positioning. The initial inter-granular friction angle is set to 1 degree for the dense packing and 20 for the loose one in order to have different porosities. Once two packing with different porosities are obtained, the final value of inter-granular friction is set to 30 degrees.

The initial porosity of the dense packing is 0.41, and for loose packing 0.36.

Table 6.1 Particle size distribution of the granular sample

Weight(%)	Diameter (mm)
30	1-1.4
35	0.85
35	0.6

6.5 Results and discussion

6.5.1 Hydraulic behavior

Water Retention curves

The water retention curves for dense and loose packings in the case of connected and disconnected phases are presented in figure 6.6. When the suction is equal to zero, the sample

is fully saturated. When the suction increases the degree of saturation decreases until zero in the case of connected phases for the funicular model and decreases to a constant value in the case of disconnected phases, due to the presence of trapped water in the pores. The presence of the menisci in the funicular-pendular regime in both cases increases slightly the degree of saturation for the same suction for high suction values ($S_r < 0.3$).

If we compare dense and loose packings water retention curves, We notice that for the same suction, the degree of saturation is higher for the dense packing. This can be explained by the fact that in the case of dense packing more contacts are created, and the distances between the grains are smaller, which means that the curvature of the wetting-non wetting interface for the same suction is lower, then the capillary pressure (inversely proportional to the curvature) at the pore is higher, which requires higher suction to provoke the air invasion in the pore. The number of menisci is also higher for the dense packing.

Menisci distribution

During the drainage process, the menisci start to appear as soon as the degree of saturation decreases, and their number start to increase while the air phase invades the sample (figure 6.7). In the case of connected phases, in the end of the drainage process, only menisci are left over between the grains for normalized suctions that are higher than 55 ($p_c^* >= 55$). The final number of menisci in this case is equal to the number of menisci generated by the pendular model only.

However, It is noticed that the pendular model alone, allows the formation of menisci for lower suctions as well (figure 6.7), while according to the drainage model, It is not possible, the sample is either fully saturated or not well drained. This plot allows then to set a range of validity of normalized suction values for the pendular model ($p_c^* >= 55$ in this case). This range of suctions are the suction for which there are no menisci that overlap as well. Any presence of menisci for lower suction is not physically true.

If the normalized capillary stress components are plotted during the drainage, Figure 6.8 shows that the capillary stress tensor is isotropic.

During imbibition, the menisci are formed only between grains in contact, while during drainage it is possible to have distant menisci as well. Those additional distant menisci are the reason behind the presence of the hydraulic hysteresis in the pendular regime.

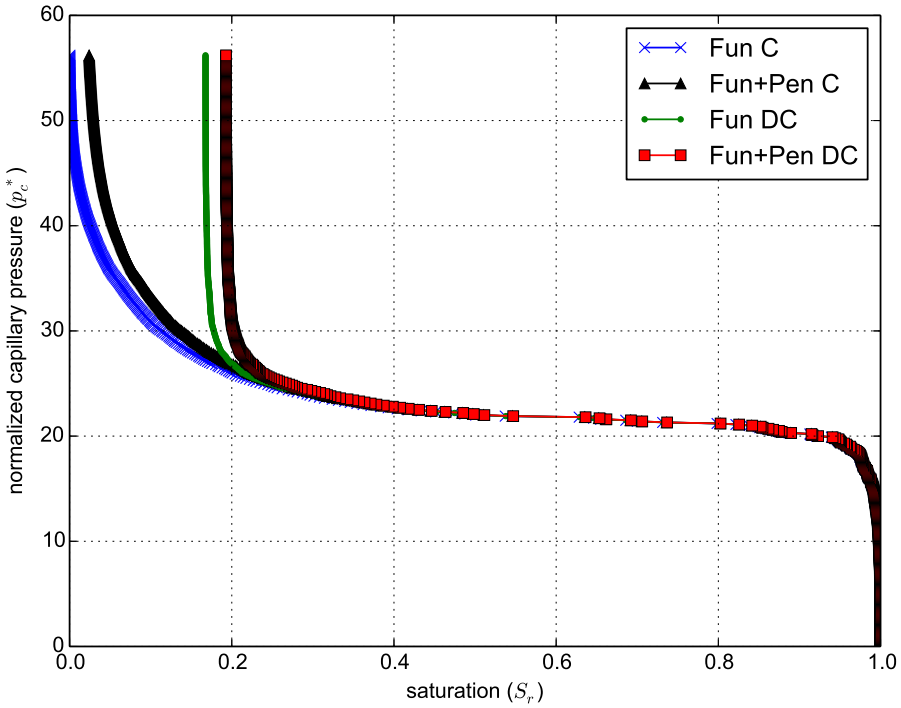

(a) Dense

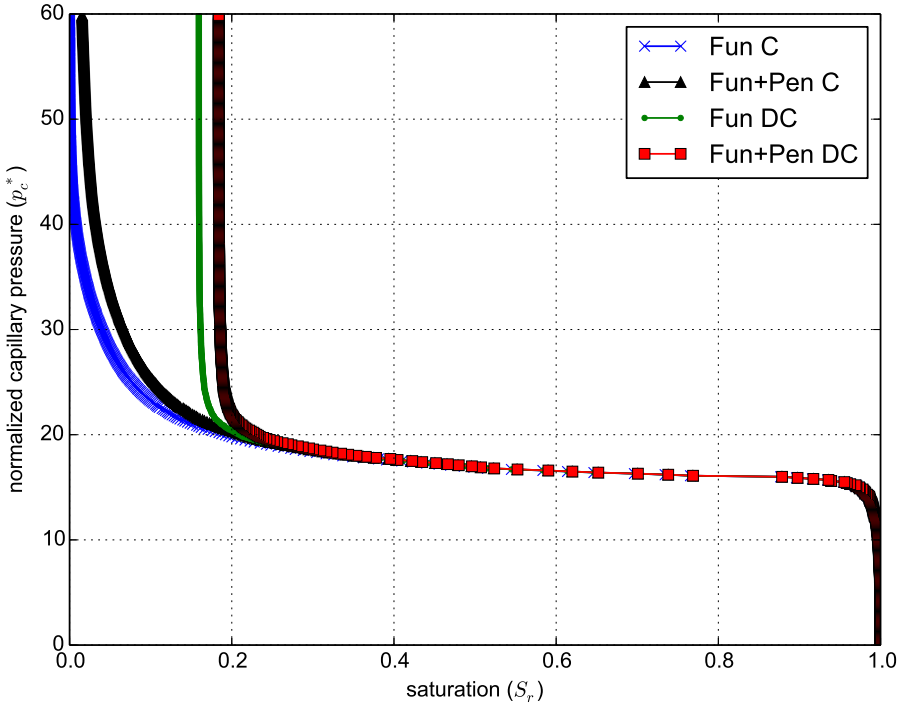

(b) Loose

Figure 6.6 The water retention curves for both dense and loose packings in the case of connected (C) and disconnected phases (DC).

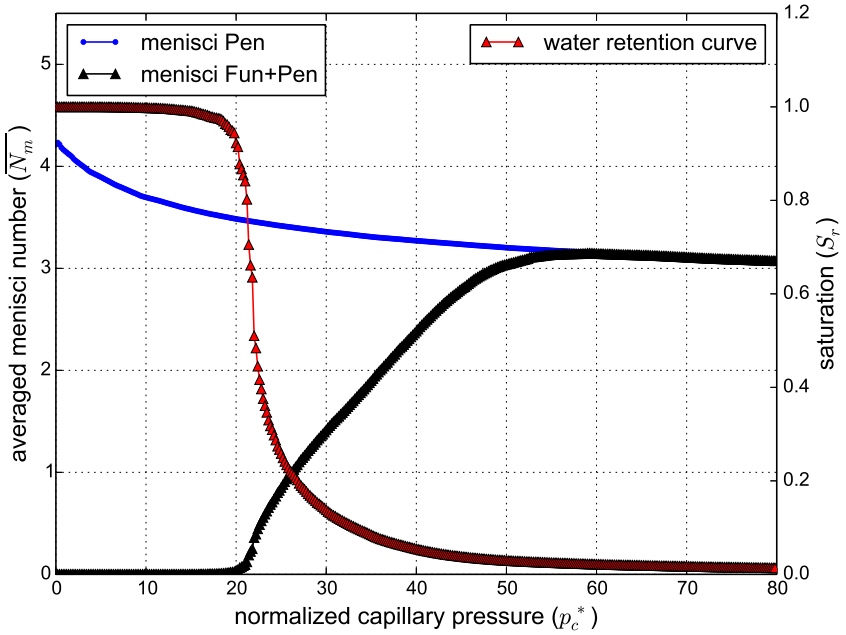

Figure 6.7 The evolution of the normalized number of menisci ($\overline{N_m} = N_m/N_{cont}$) with the suction and the saturation.

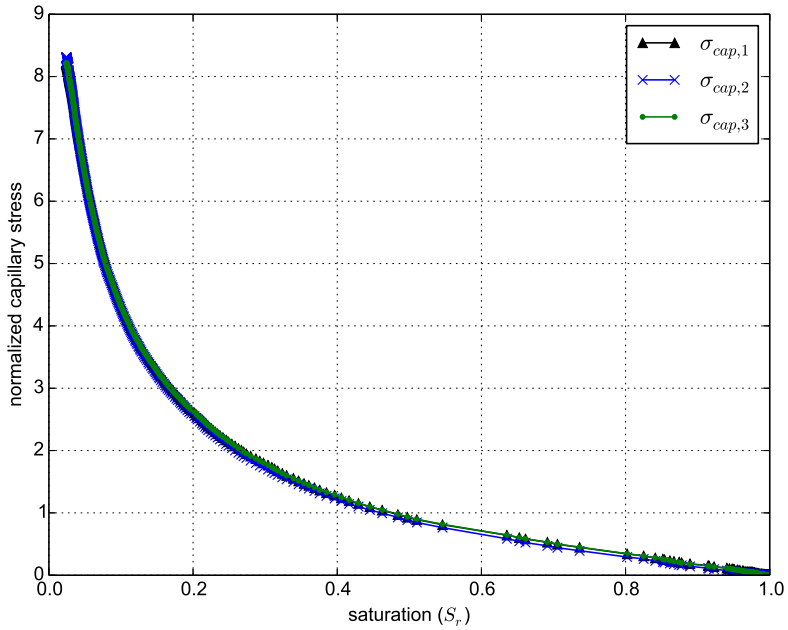

Figure 6.8 The capillary stress components during the drainage process.

To evaluate the number of distant menisci, the probability density functions of the menisci are plotted as function of the normalized distance between the pairs of grains of radii R_1 and R_2 :$D^* = 2D/(R_1 + R_2)$ at the end of the drainage phase in the case of connected and disconnected phases (figure 6.9).

The results show that in the case of disconnected phases, the number of grains in contact is about 80% of the total number of menisci. The frequency of distant menisci decreases when the distance increases.

In the case of connected phases, the number of menisci formed between grains in contact increases to 85%.

We also notice that the maximum value of the normalized distance is higher in the case of disconnected phases (0.17 in the disconnected phases case compared to 0.07 in the case of connected phases).

This can be explained by the fact that in the case of disconnected phases the menisci when formed at a specific suction keep their suction ultimately while in the case of connected phases, the suction is uniform in the whole packing. Then, the suction of menisci that are formed at a previous step will increase, and when the suction increases, the volume of menisci decreases and the rupture distance decreases as well. These menisci will break eventually during the drainage.

That means that at the end of the drainage, the menisci that are at a higher distance than the rupture distance corresponding to the final suction value (the highest suction) will break eventually, which will also decrease the frequency of the distant menisci.

The comparison between dense and loose packings show that there are more distant menisci in the loose packing.

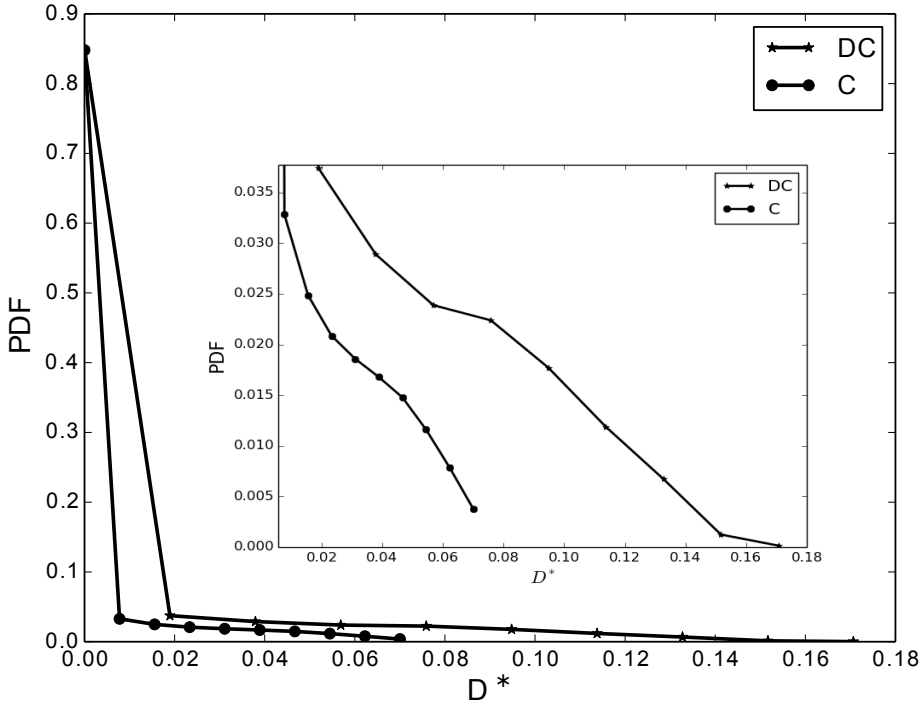

(a)

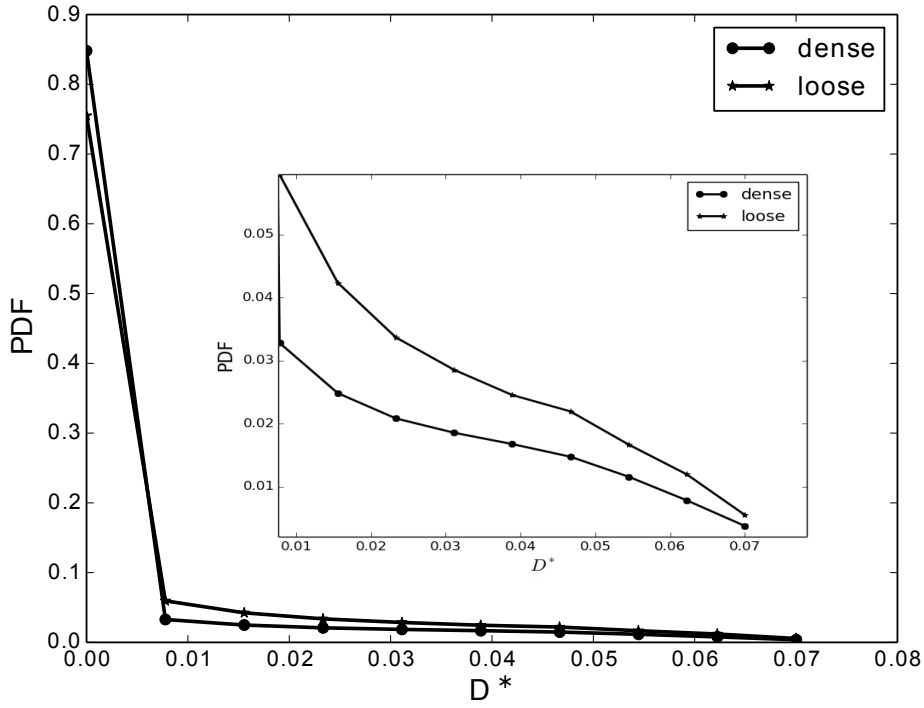

(b)

Figure 6.9 The probability density functions of the number of the menisci as function of the distance (a) in the case of connected and disconnected phases and (b) in the case of dense and loose packing.

6.5.2 Mechanical behavior

Stress contributions of pendular and funicular regimes

The normalized mean funicular and capillary stresses are plotted as function of the suction in figures 6.10 and 6.11:

$$\sigma^*_{fun} = (\sigma_{fun} - pw) * R_m/\gamma_{nw} \tag{6.16}$$

$$\sigma^*_{pen} = \sigma_{pen} * R_m/\gamma_{nw} \tag{6.17}$$

R_m is the mean radius in the sample. When the sample is fully saturated, σ^*_{fun} is the only stress that exists in the sample. It is equal to $-p_w I$. The pressure of the water decreases, and the value of the stress increases. The pendular stress is equal to zero.

When the saturation decreases, menisci start to appear, the capillary stress increases and the funicular stress decreases. If the phases are connected, the funicular stress decreases to zero at the end of the drainage, and the only stress due to the presence of the water is the pendular stress (figure 6.10). When the phases are disconnected, trapped water and menisci are left and at the end of the drainage both funicular and pendular stress exist and remain constant (figure 6.11).

6.5.3 $p_c - \varepsilon - S_r$ relationship

The $p_c - \varepsilon$ curves are plotted in the case of connected and disconnected phases.

In the case of disconnected phases, the $p_c - \varepsilon$ curves for dense and loose packing show that when the sample is still highly saturated ($S_r \approx 1$, $p^*_c < 20$), the deformation is linear. This can be explained by the fact that the deformation is still dominated by the effective stress of the fully saturated soil:

$$\sigma' = \sigma - p_w I \tag{6.18}$$

The pressure of the w-phase p_w decreases leading to an increase of the effective stress provoking the shrinkage of the sample until the invasion of the n-phase. The deformations are higher in the case of loose packing (almost twice higher than the deformation of the dense packing) (figures 6.12 and 6.13).

For the funicular model only, when the n-phase starts invading the granular sample, the strain evolution becomes non linear, and the sample starts swelling. At the end of the

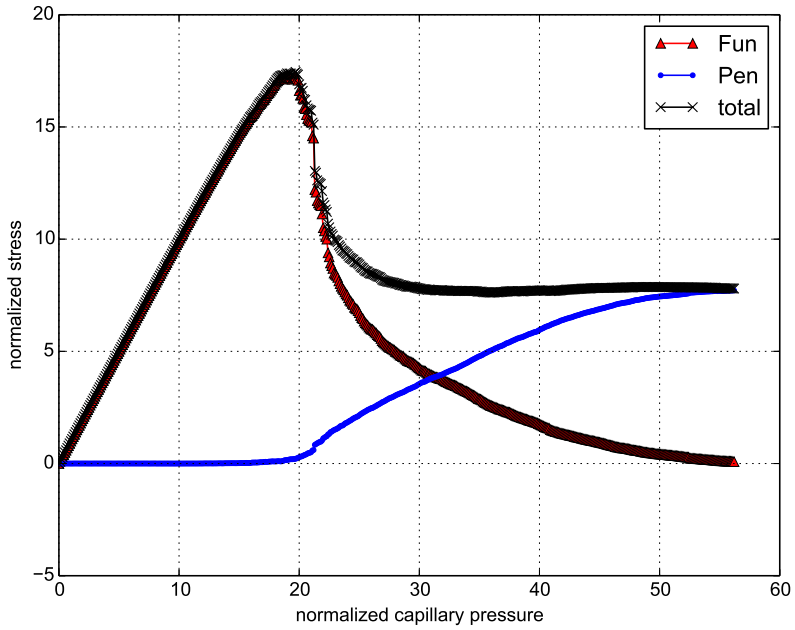

Figure 6.10 The stresses (capillary,funicular and total stresses) evolution during the drainage process in the case of connected phases.

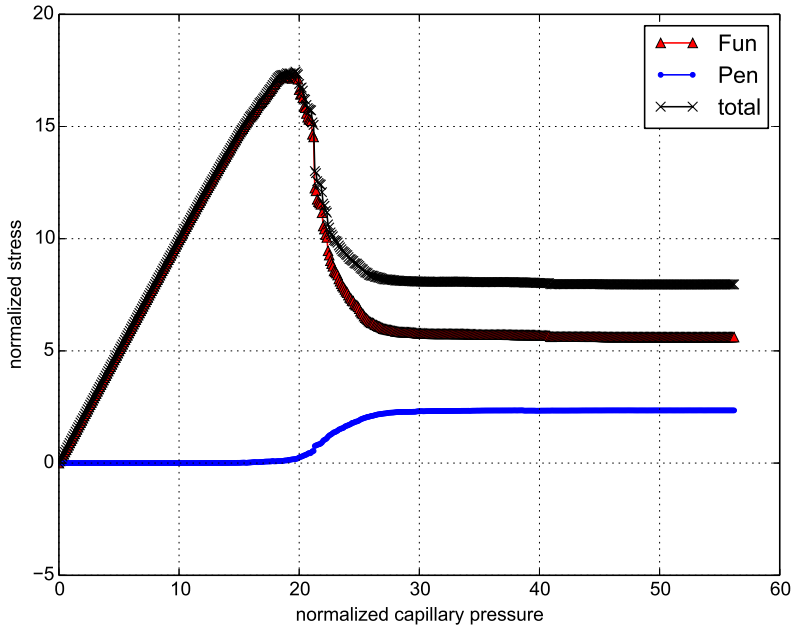

Figure 6.11 The stresses (capillary,funicular and total stresses) evolution during the drainage process in the case of disconnected phases.

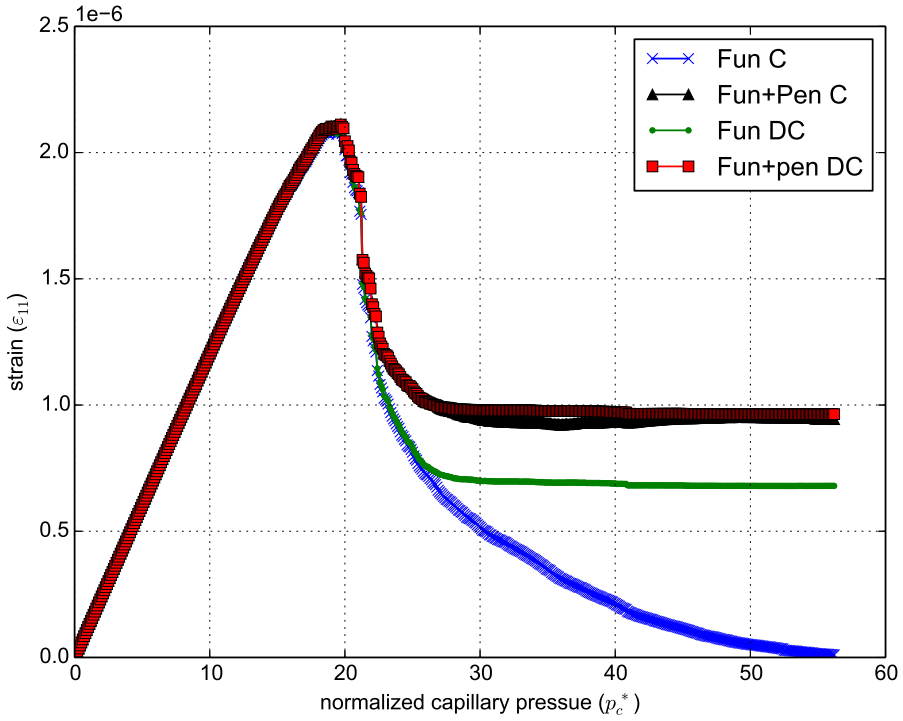

Figure 6.12 The evolution of strain with the capillary pressure during the drainage process for the dense packing in the case of connected and disconnected phases.

drainage, the deformation induced by the drainage is fully eliminated in the case of connected phases, while in the case of disconnected phases a residual deformation remains at the end of the process due to the presence of trapped water in the pores.

When the menisci are added to the simulation, in the case of pendular-funicular coupling, menisci start to form between the grains during the drainage process when the n-phase starts invading the sample. The menisci connect the particles by an attractive capillary force which reduces the swelling of the sample compared to the funicular alone. The deformation induced by the drainage is not fully eliminated at the end of the process in the case of connected phases, and it is higher compared to the funicular model only in the case of disconnected phases.

In the presence of menisci, the residual deformation in the case of connected and disconnected phases at the end of the process is almost the same (slightly higher in the case of connected phases). It means that the influence of the trapped water on the mechanical behavior of the sample is slightly smaller than the effect of the menisci that replace it in the

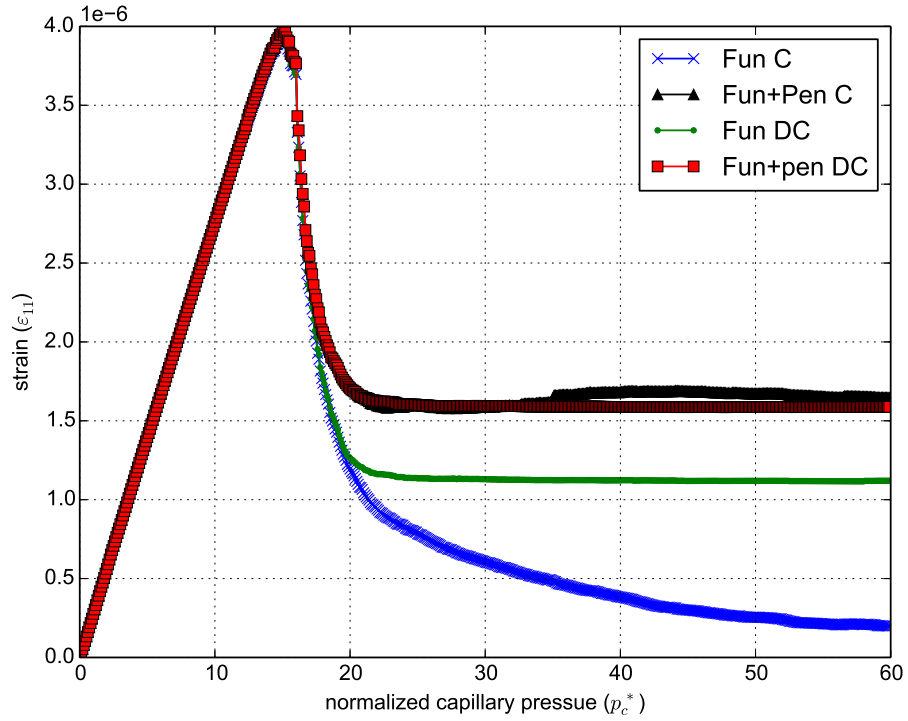

(a)

Figure 6.13 The evolution of strain with the capillary pressure during the drainage process for the loose packing in the case of connected and disconnected.

case of connected phases.

The results are similar for the loose packings (figure 6.13).

Effective stress parameter

Bishop's generalized the effective stress formulation of Terzaghi to the following form:

$$\sigma' = (\sigma - p_n) + \chi(p_n - p_w) \tag{6.19}$$

χ is the effective stress parameter. It is a function of saturation and it is equal to 0 when the granular medium is dry and equal to 1 when it is fully saturated.

The effective stress parameter χ can be computed in two ways:

- From a macroscopic point of view using the macroscopic elastic deformation and assuming $\sigma' = E\varepsilon$

$$\chi^M = \frac{E\varepsilon - (\sigma - p_n)}{p_n - p_w} \tag{6.20}$$

- From a microscopic point of view if σ' is assumed to be equal to the contact stress computed using Love-Weber formula σ_{cont}

$$\chi^m = \frac{\sigma_{cont} - (\sigma - p_n)}{p_n - p_w} \tag{6.21}$$

Both ways lead to the same results in the calculations of Yuan [93] for dense packing in the funicular case. We follow here again both ways to calculate the effective stress parameter and the results with the presence of the pendular bridges are compared to the results obtained with the funicular model only.

The presence of the pendular rings in both connected and disconnected cases increases the value of the effective stress parameter. The difference between χ in the funicular and funicular/pendular is zero when the sample is saturated and maximum when the drainage process is over (figure 6.14).

When the packing is dense, the value of χ computed from the macro or micro points of view is almost the same. In the case of loose packing, figure 6.15 shows that it is not the same. If we plot the contact stresses as function of the deformations we realize that while the dense packing's deformation is purely elastic from the loading unloading curves, the loose packing's deformation is not. This explains the difference between the χ values calculated in both approaches. The χ calculated from the macroscopic deformation is based on the assumption that the deformation remains elastic only which is not valid for the loose packing, hence the effective stress parameter calculated at the micro scale is more reliable.

6.6 Conclusion

The pendular model was coupled with the funicular model in this chapter to simulate a complete drainage process. The main results and findings of this chapter are summarized as follows:

- The addition of the menisci has no big influence on water retention curve, the degree of saturation slightly increases when the menisci are taken into account.

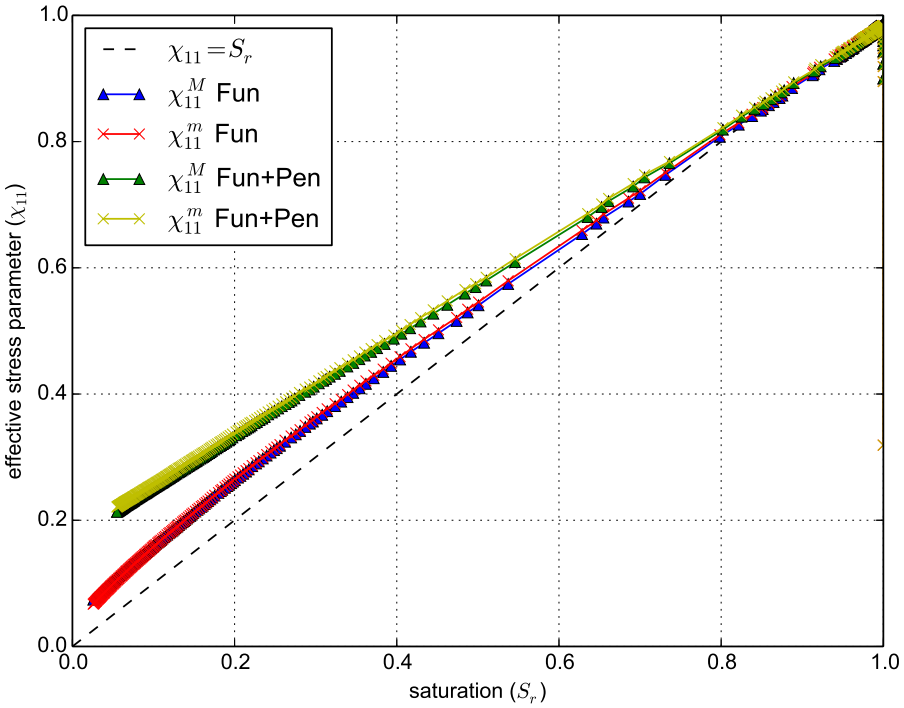

(a) Connected phases

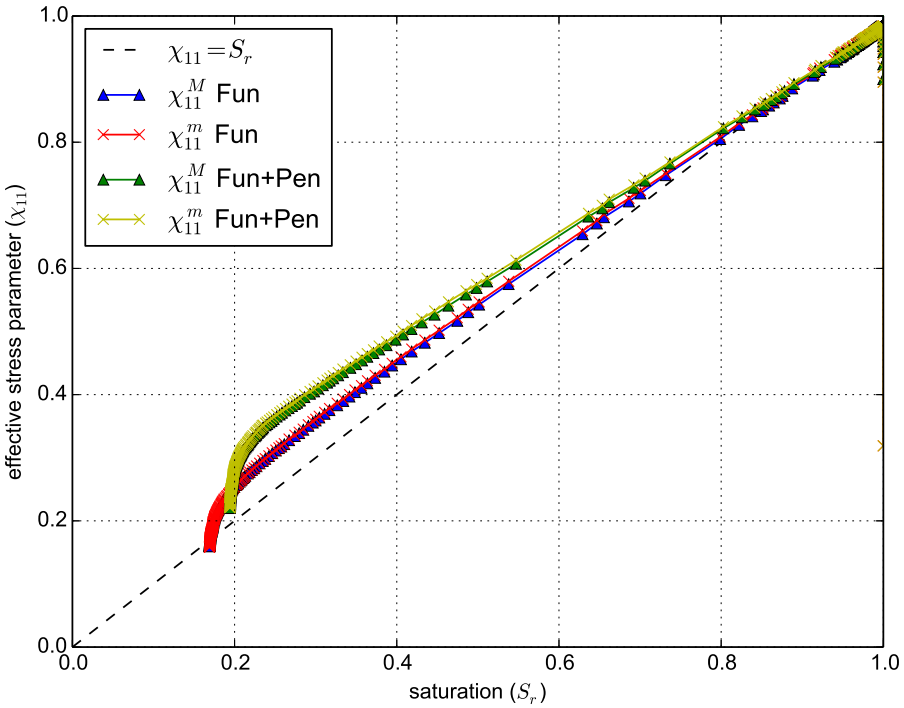

(b) Disconnected phases

Figure 6.14 The variation of the effective stress parameter with the saturation for the dense packing in the case of connected and disconnected phases.

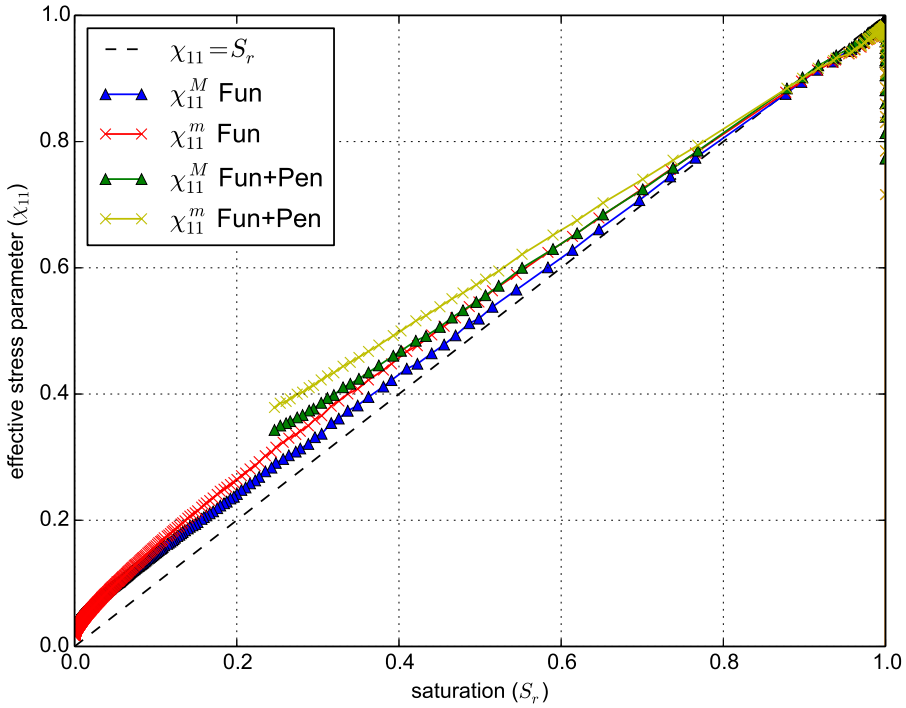

(a) Connected phases

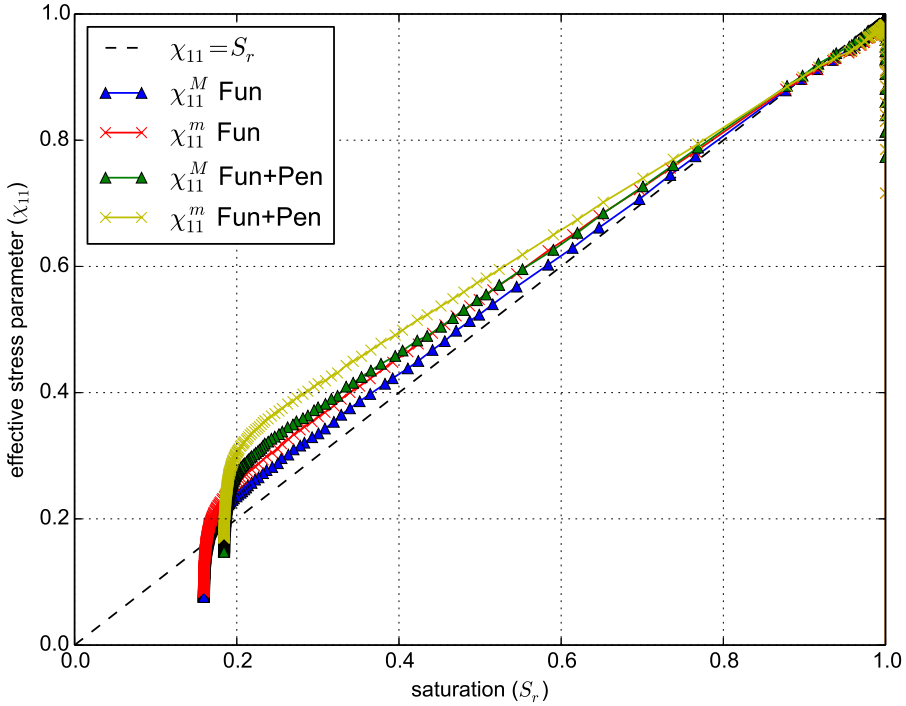

(b) Disconnected phases

Figure 6.15 The variation of the effective stress parameter with the saturation for the loose packing in the case of connected and disconnected phases.

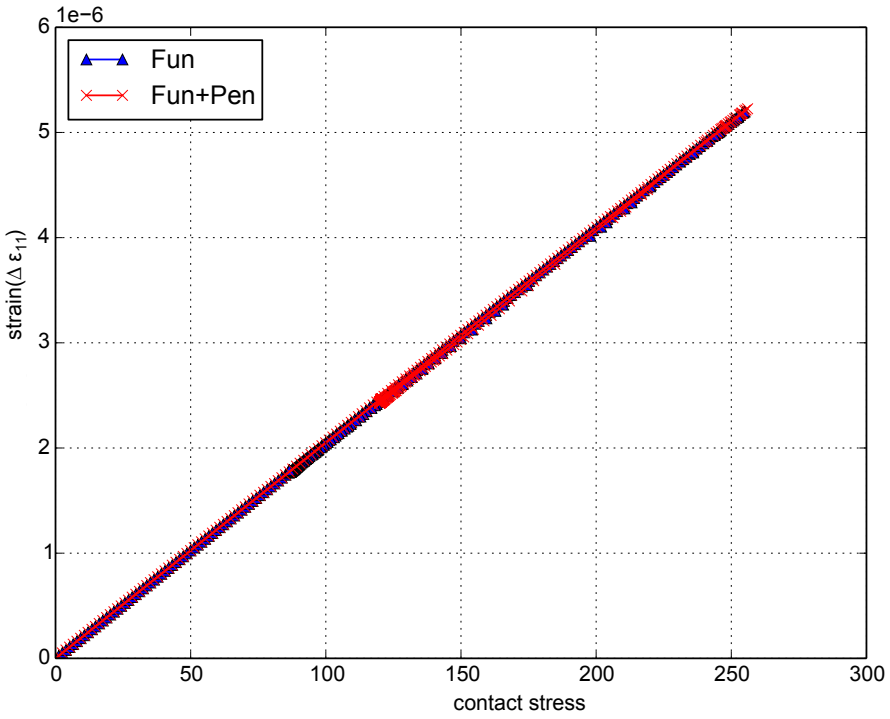

(a) Dense

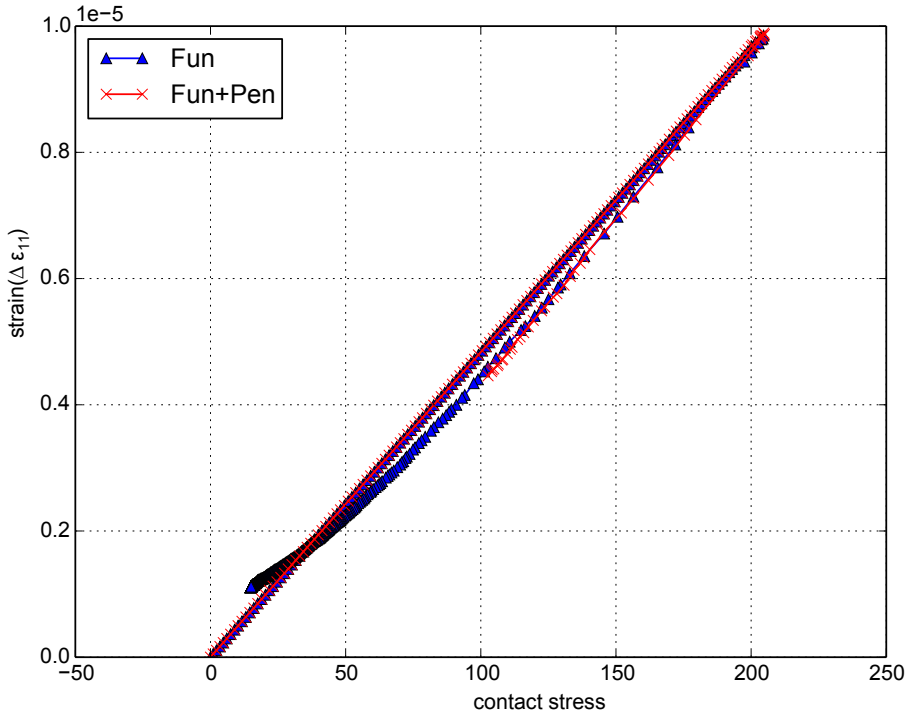

(b) Loose

Figure 6.16 The loading unloading paths for dense and loose packings.

- The menisci's influence on the mechanical behavior of unsaturated soils is not negligible, and they must be accounted for to predict the deformation and the behavior of unsaturated soils. The menisci resist to the swelling of the sample and keep a residual deformation that is not recovered at the end of the drainage and higher than the one for the funicular model alone.

- The addition of the menisci to the sample increases also the value of the effective stress parameter calculated by the funicular model only.

  The results for the effective stress parameter are more reliable in the case of dense packing where the deformation remains elastic.

Chapter 7

Compaction of a proppant region using DEM

7.1 Introduction

Hydraulic fracturing dates back to seven decades. The first commercial application of hydraulic fracturing as a well treatment technology to stimulate oil and gas production has occurred between 1946 and 1949 [52].

The discovery of hydraulic fracturing has made a revolution in the unconventional production of tight reservoirs that was almost impossible before, which improved the process of energy production and made it quite valuable (it is believed that 60 to 80 % of the reservoirs in the united states require hydraulic fracturing to keep operating [52]). It is also used to extend the life of old fields, and in many other applications such as geothermal energy extraction [66], CO_2 injection, deep earth disposal of waste, estimation of in situ stress state [32]...

Hydraulic fracturing is a technique in which rock is fractured by a pressurized liquid. It is used after drilling is completed. The process involves the high-pressure injection of fluid that contains proppants into a wellbore to create cracks in the rock formations. The pressure of the fluid must overcome the in-situ geologic stresses and the strength of the formation to propagate the fracture. When the pressure of the fracturing liquid is reduced, the proppant injected with the fluid must maintain the fractures open to increase the permeability of the rock formation and facilitate the extraction of hydrocarbons.

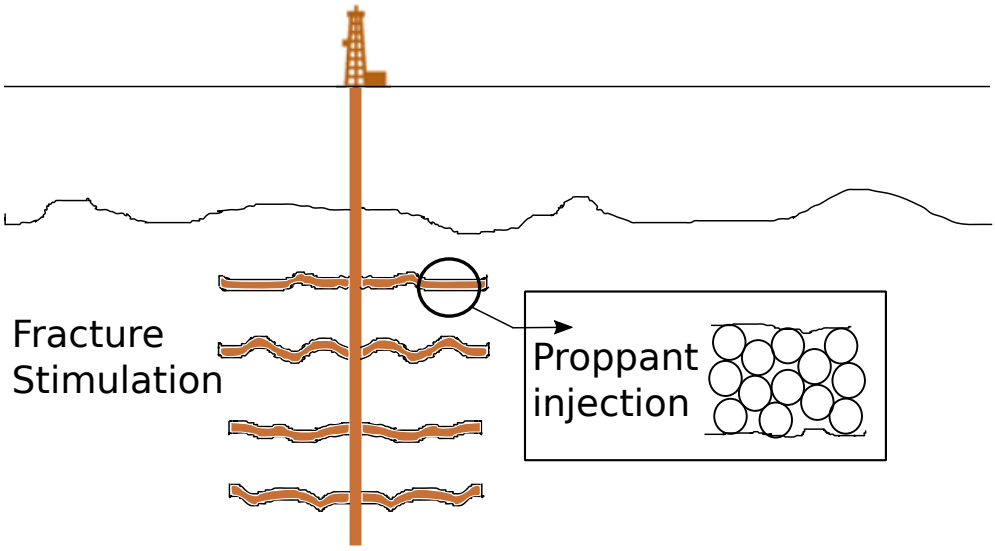

Figure 7.1 Illustration of a vertical well.

The process consists on four main stages that also include protecting the ground water supplies. The stages are briefly described below:

- Stage 1: Acid stage: This stage consists of using water mixed with dilute acid such as hydrochloric or muriatic acid to pave the cement debris in the wellbore after drilling and open the way for the injection of fluids used for hydraulic fracturing.

- Stage 2: Pad stage: During this stage water is used without proppant material to initiate fractures in the formation and to facilitate the flow and the placement of the proppant. The generation of a fracture will depends on the material (formation) strength and in situ stresses. In shallow earth environment, the fracture is influenced by the material strength, while in deep earth environment it is controlled by in situ stress states.

  These fractures are restricted to brittle elastic ones, and they are formed in the direction that is perpendicular to the direction of the minimum principal stress. At shallow depths (<610 m), the overburden stress is the least principal stress and the fractures will be horizontally oriented. At large depth, overburden stress increases and becomes the dominant stress. The resulting fracture will have a vertical orientation. The fracture can also cross over a boundary where the principal stress direction changes and leads to the reorientation of the fracture. The problem however is not that simple,

the reorientation of fracture is also influenced by the material inhomogeneity, rates of fluid injections, poromechanical effects, ...

The topography of the fracture, can be quite complex. Experimental analyses on fractures show that fracture surface topographies are rough [13, 73]. The surface topography depends not only on the stress state but also, any small heterogeneity, which can result in a quite different fracture topography. The fracture topography is of great importance and influences strongly the permeability of the fracture, because it influences the fluid transport characteristics [47, 67].

The extent of the fracture is also controlled by many parameters: the upper confining formation, the volume, rate and pressure of the pumped fluid. It is also influenced by natural fractures and faults.

- Stage 3: Prop sequence stage: This stage consists of a sequence of injecting water combined with proppant materials.

The deposition of the proppant is a major concern in the study of this stage. It is generally assumed to be Stokes settling. Therefore, the proppant settling rate is normally based on Stokes' law [17, 83] (figure 7.2). For low Reynolds number ($R_e < 2$)the settling rate is:

$$V_S = \frac{2}{9}\frac{(\rho_p - \rho_f)}{\mu} g R^2 \tag{7.1}$$

where V_S is Stokes' settling velocity (m/s), g is the gravitational acceleration (m/s^2), ρ_p is the mass density of the particles (kg/m^3), ρ_f is the mass density of the fluid (kg/m^3), μ is the dynamic viscosity (kg/ms) and R the radius of the particle.

In reality the gravitational settling of the proppant depends on many factors such as the fluid viscosity, the proppant size, fracture wall effect, dynamic state of the fluid, turbulence, inertial effects and the treatment duration [22, 27, 41, 59].

Studies that have been used in areas of applications such geomorphology in order to understand the sediment transport as function of grains size and fluid velocity in rivers and deltas [4] have been performed on the settling of the proppant.

A part of these were experimental studies[11, 85]. In experiments conducted using

glass plates, it was found that stable proppant packs of single proppant grain widths could only be formed when proppant diameters were the same size as the fracture width [5].

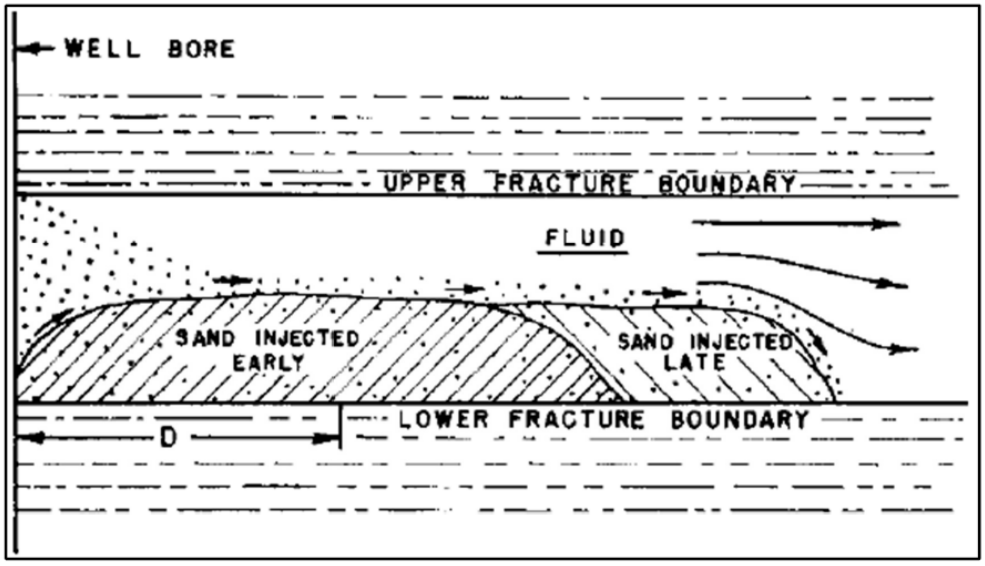

Figure 7.2 Sand movement and settling in slot flow experiment [38].

During the process, the injected fluids carry confining stresses, but once the pumping is stopped, the stresses are transferred to the deposited proppant packs. These proppants play a crucial role in keeping the fracture open at the desired conductivity. They can vary from common sand, to manufactured polymer beads and can be coated with resins or other surface modification agents to improve proppant pack cohesion, compressive strength and permeability. Proppant should be permeable under high pressures and strong enough to support the closure of the fracture: sand of large particle size have greater permeability but risk to crush under high pressures and produce finer particles which will reduce their permeability. Coating sand by resin or using ceramic and the manufactured proppant will help maintaining the ideal mesh size with sufficient strength. Proppants with high spherity are also usually a better choice. The size of the proppants usually vary from 0.21 and 0.85 mm.

- Stage 4: Flushing stage: This stage consists on flushing the excess of proppant from the wellbore using only fresh water.

The study of hydraulic fracturing is a very complex problem in which many factors are involved. Summarizing the main issues that it addresses, we obtain three main questions:

- What is the injection pressure needed to create a fracture?
- What is the length, orientation and topography of the fracture?
- How can the fracture be maintained in an open configuration to increase the efficiency of the energy recovery? This question is the focus of this study.

Many studies have been done to answer these questions. Models to describe hydraulic fracturing (more specifically cracks opening and propagation) can be divided into two categories:

- The uncoupled models based on the elasticity theory. In these models the rock formation is assumed to be elastic. The fracture opening is calculated using elastic constants of the rock, in situ stresses and pressure within the fracture.

- The coupled models including the poromechanical effects. These models are relatively new (since 1970). The poromechanical effects are taken into account based on Biot's theory of poroelasticity [6], the volumetric response of the body is sensitive to loading rate . Fluid pressure is also a dependent variable. Darcy law is used for the flow of the fluid through the pores and Hooke's law is used for the elastic behavior of the rock formation.

  Some studies include the thermal effects as well [82].

The third question that is the interest of this study exposes the problem of proppant-rock formation interaction at the fracture [81].

The analysis of the interaction between the proppant and the formation presents several unilateral contact problems in mechanics:

- The extent of the proppant zone.
- The aperture of the fracture.
- What happens to the proppant when the resource is extracted.

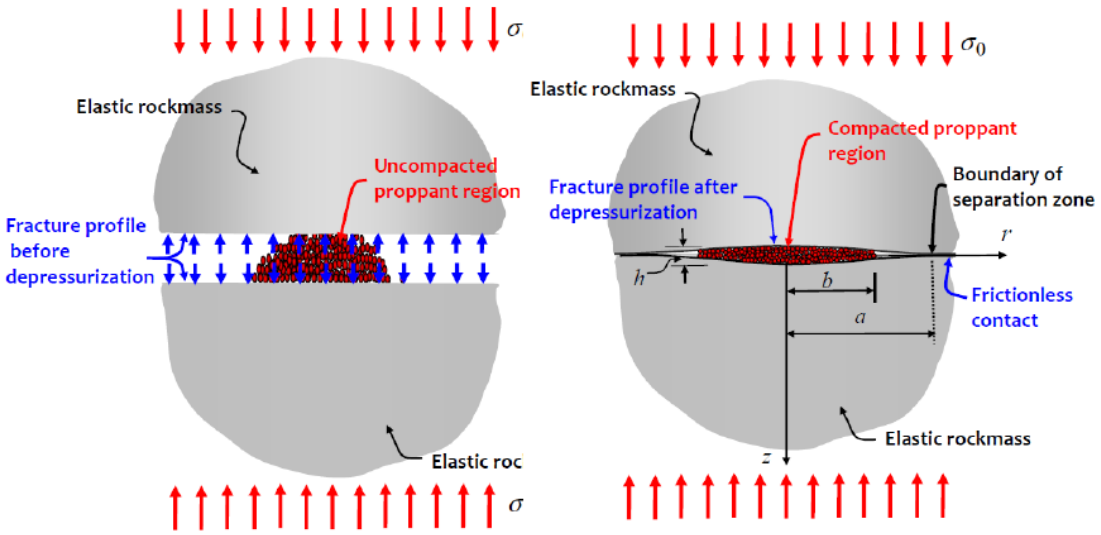

Figure 7.3 The idealized study where proppant is discrete and rock formation is modeled as an elastic continuum.

Both finite elements models [43, 60] and discrete elements models [3] can be used to study proppant-rock interaction problems.

Finite element models treat volumes of the fracture, in either two dimensions or three dimensions ,as grid blocks for a finite calculation mesh and use continuum equations. These models are not able to model the proppant that is a granular medium.

Discrete element models use the basic mechanical interaction between the proppant grains and fracture walls in this case and appropriate boundary conditions to achieve a similar result.

DEM models might be expensive in terms of computational cost of the simulation, since computation time grows as a function of particle number (mainly to simulate the rock block).

The idealized approach to study this problem will be to consider the rock mass as an elastic rock mass and the proppant region as a granular medium (figure 7.3).

Other approaches also studied this problem. Selvadurai [78, 79] have studied the zone of separation created by the proppant in hydraulic fracturing techniques. Analytical solutions have been developed as function of the material properties of the rock formation in the case of rigid disc shaped proppant region of finite thickness (figure 7.4).

The zone of separation is studied also by replacing the rigid inclusion by a concentrated load (figure 7.6) or an axisymmetric internal distributed pressure (figure 7.5)that simplifies the mathematical analysis considerably [80]. This assumption is valid for fractures oriented

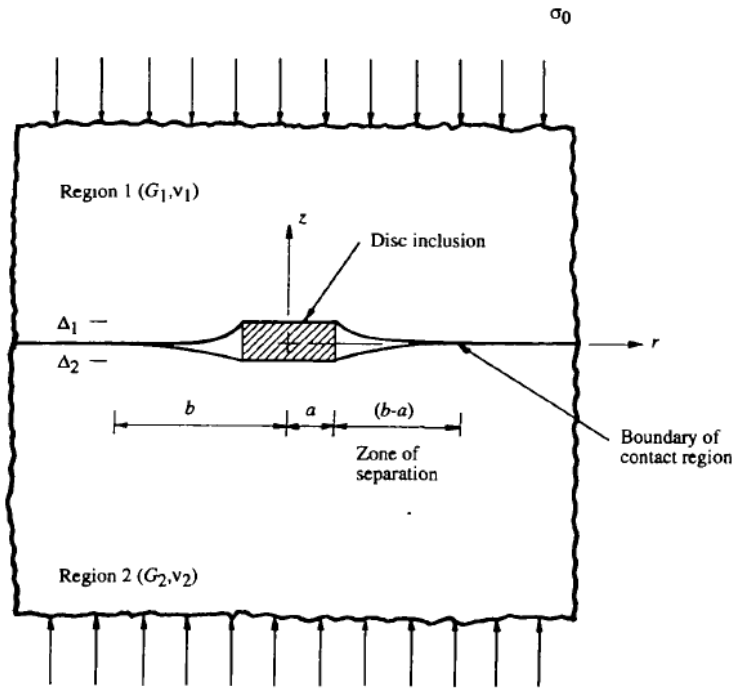

Figure 7.4 A disc inclusion between two elastic semi infinite spaces (from [79])

normal to the direction of compression.

Writing the mixed boundary value condition at the interface depending on the problem (disc inclusion or applied load), the value of the zone of separation can be determined.

The problem can be solved using Love's strain-potential approach [42], that is written as following in the absence of body forces:

$$\nabla^2\nabla^2\Phi(r,z) \tag{7.2}$$

where $\Phi(r,z)$ is Love's strain potential and

$$\nabla^2 = \frac{\partial^2}{\partial r^2} + \frac{1}{r}\frac{\partial}{\partial r} + \frac{\partial^2}{\partial z^2} \tag{7.3}$$

In the case of axisymmetric internal distributed pressure, in the analytical studies, Love's strain function should be solved with the following mixed boundary conditions (a being the zone of seperation (figure 7.5)):

$$\sigma_{rz}^{(1)}(r,0) = \sigma_{rz}^{(2)}(r,0) = 0 \qquad 0 \leqslant r < \infty \tag{7.4}$$

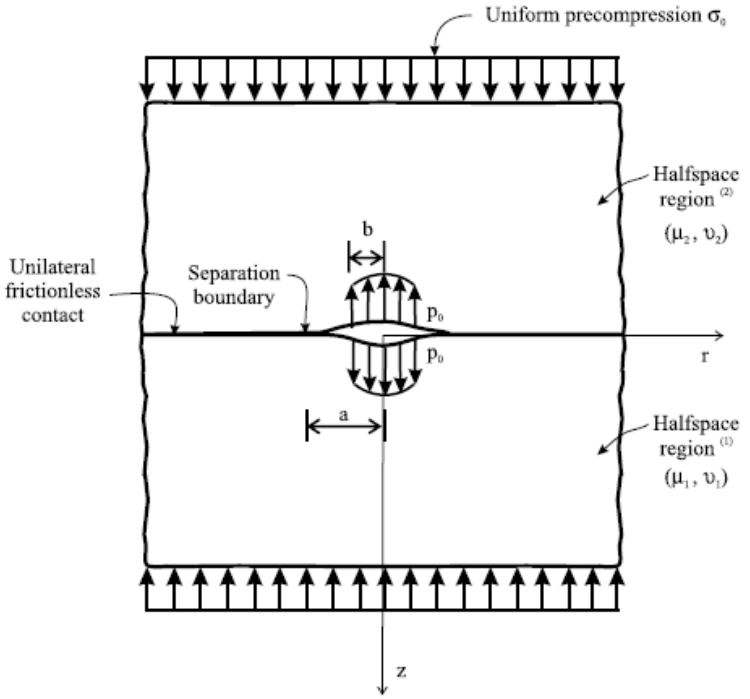

Figure 7.5 Separation at the elastic interface by tractions (from [80])

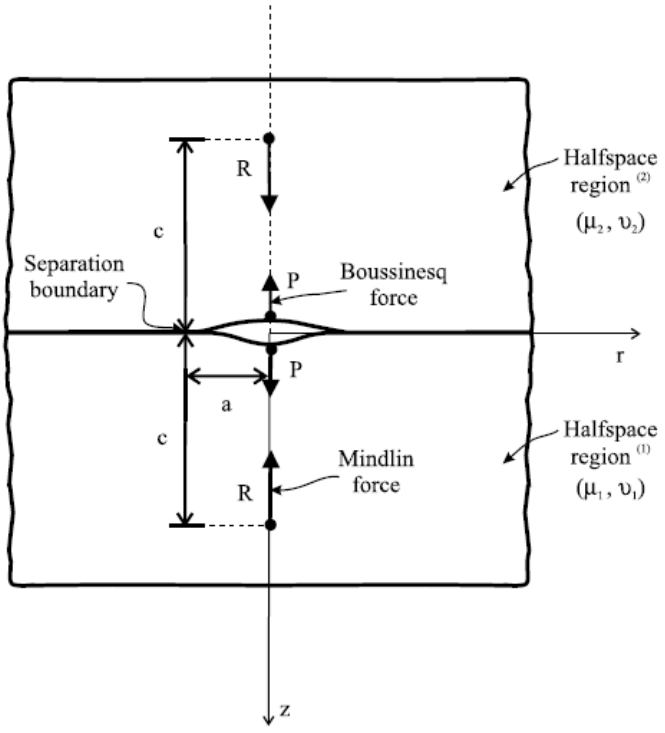

Figure 7.6 Separation at the interface by equal concentrated forces (from [80])

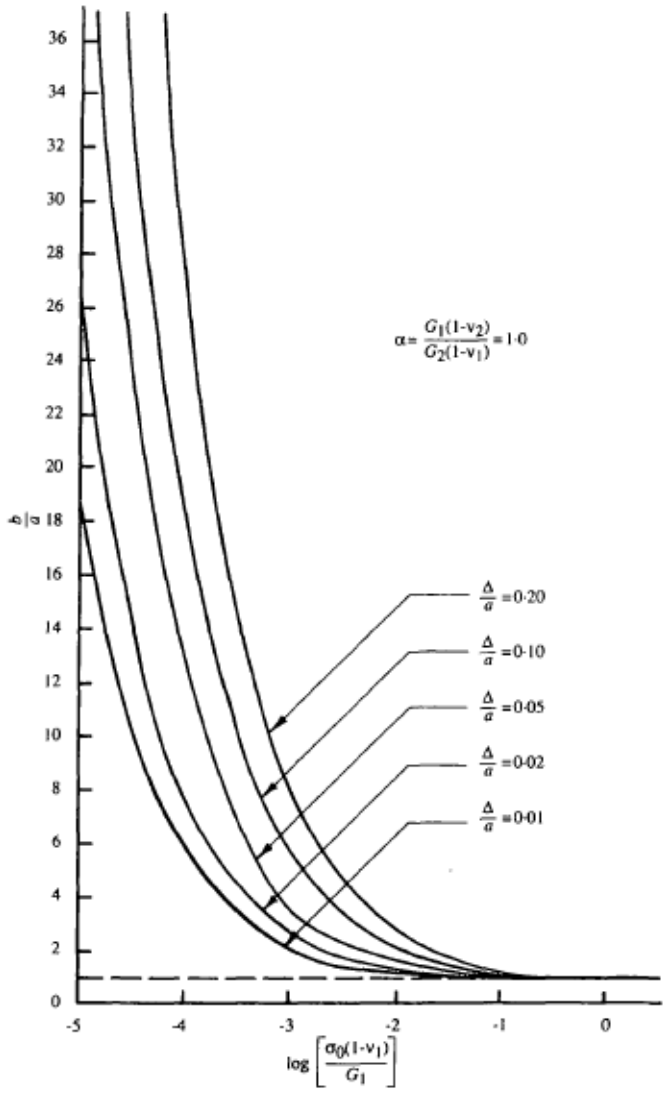

Figure 7.7 Results for the zone of separation at the interface for different disc thicknesses(from [79])

$$\sigma_{zz}^{(1)}(r,0) = \sigma_{zz}^{(2)}(r,0) \qquad a \leqslant r < \infty \tag{7.5}$$

a is here the extent of the fracture.

$$u_z^{(1)}(r,0) = u_z^{(2)}(r,0) \qquad a \leqslant r < \infty \tag{7.6}$$

σ_{zz} is the normal stress acting on the rock blocks , and u_z refers to the vertical displacement.

$$\sigma_{zz}^{(1)}(r,0) = p^1(r) \qquad 0 \leqslant r < b \tag{7.7}$$

$$\sigma_{zz}^{(2)}(r,0) = p^2(r) \qquad 0 \leqslant r < b \tag{7.8}$$

$p^1(r)$ and $p^2(r)$ are the normal stress distribution acting on the rock formations, and b is the radius on which are acting the load $p^1(r)$ and $p^2(r)$. Also the solution should satisfy the regularity conditions:

$$\sigma_{zz}^{(1)}(r,0) = \sigma_{zz}^{(2)}(r,0) \to 0 \qquad r \to a \tag{7.9}$$

$$\sigma_{zz}^{(1)}(r,z) = \sigma_{zz}^{(2)}(r,z) \to -\sigma_0 \qquad |z| \to \infty \tag{7.10}$$

The solution to the above mixed boundary value problem can be approached in a variety of ways to determine the extent of the fracture [79].

In the case of two unequal concentrated load, the value of the zone of separation a as function of both loads P_1 and P_2 is (figure 7.6):

$$a = (\frac{P_1 + P_2}{4\pi\sigma_0})^{0.5} \tag{7.11}$$

In the case of disc inclusion the displacement is imposed and the boundary conditions are written as function of the disc thickness. The results of the extent of zone of the separation (b) at the interface for different values of disc inclusions are presented in figure 8.10.

This chapter suggests a solution that improves the analytical results. The suggested model aims to get information about the stress distribution exerted by the granular proppant on the rock formation. These information can be used in the analytical studies or in FEM

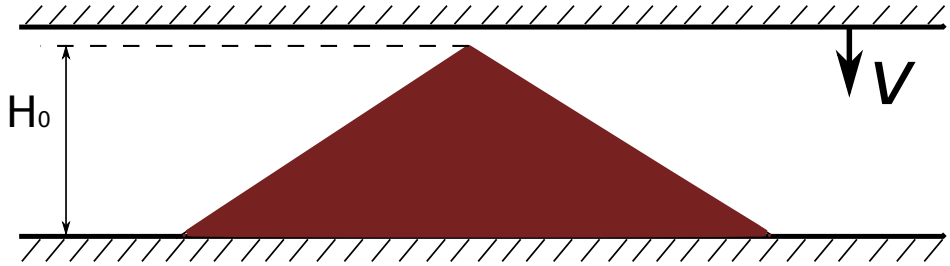

Figure 7.8 Illustration of the model.

simulations in order to identify the fracture extent.
The model is in fully dry conditions, the effect on the hydraulic fracturing fluids is not taken into account.

7.2 Development of the DEM model for the proppant region

A DEM model is built where the rock formations are replaced by two rigid plates. The proppant is represented by spherical particles of 1 mm diameter size. The intergranular friction angle is equal to 30 degrees. The friction angle between the plates and the grains is also set to 30 degrees.

The lower plate is fixed. The proppant pack is deposited by gravity on the lower plate, to form a pile. Once the pile is in equilibrium, and the slope has reached the angle of repose (between 28 and 30 degrees), the upper plate is subjected to a displacement at constant velocity v (figure 7.8).

7.3 Proppant Compaction

We define H_0 as the initial gap between the upper and lower plates which also corresponds to the height of the pile of proppant. H is updated value of the gap between both plates (figure 7.9).

b_u and b_L are the radii of the upper and lower zones of contact with the upper and lower plates respectively, normalized by the diameter of the proppant grains. To calculate the value of b_u and b_L, rings of two grain diameters thickness and with different radii covering

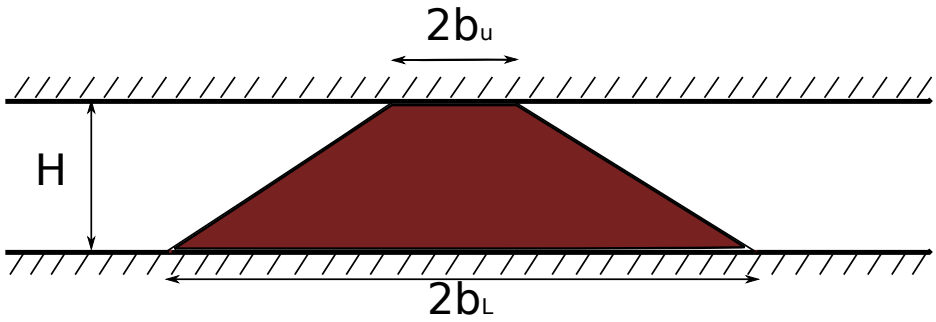

Figure 7.9 Illustration of the model during the simulation.

the whole proppant zone are considered. Only if the ring has enough grains inside, it is taken into account. This condition is verified if the surface of the k grains inside the ring cover at least 2/3 of the total surface of the ring (figure 7.10).

$$\Sigma_1^k \pi r_i^2 > \frac{2}{3} A_{ring} \tag{7.12}$$

While the upper plate is moving, the upper radius b_u increases to approach b_L that remains constant for a while before it starts growing with the upper radius in the same time (figure 7.11).

The whole system during the simulation is in equilibrium. The total force applied on the upper plate is equal to the total force acting on the lower one ($F_u = F_L$). This is checked during the simulation. The radii of both upper and lower zones are different and so is the averaged stresses $P_{u,L}$ that is equal to the ratio of the total force divided by the area of the contact zone are also different.

$$P_{u,L} = \frac{F_{u,L}}{\pi b_{u,L}^2} \tag{7.13}$$

The proppant compaction curves ($P_{u,L} = f(log(H_0/H))$) are presented below (figures 7.12 and 7.13).

The curve shows that $P_{u,L}$ increase with the decrease of H, until the movement of the upper plate is blocked by the pile of proppant. At this stage the pressure on the plates keeps increasing while the value of H remains almost constant, which corresponds to the final value of H, defining the asymptote of the curve ($Log(H0/H) \approx 1.4$).

If we zoom on the first part of the curve before the movement of the upper plate is almost blocked by the proppant, we observe that there are some pressure drops just before

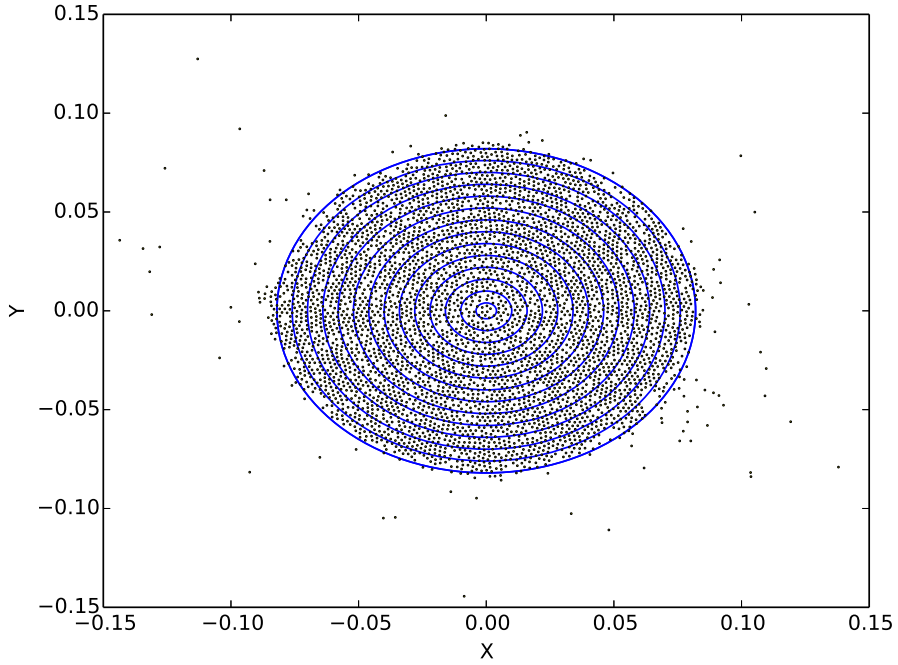

Figure 7.10 The rings that are taken into account in the estimation of b.

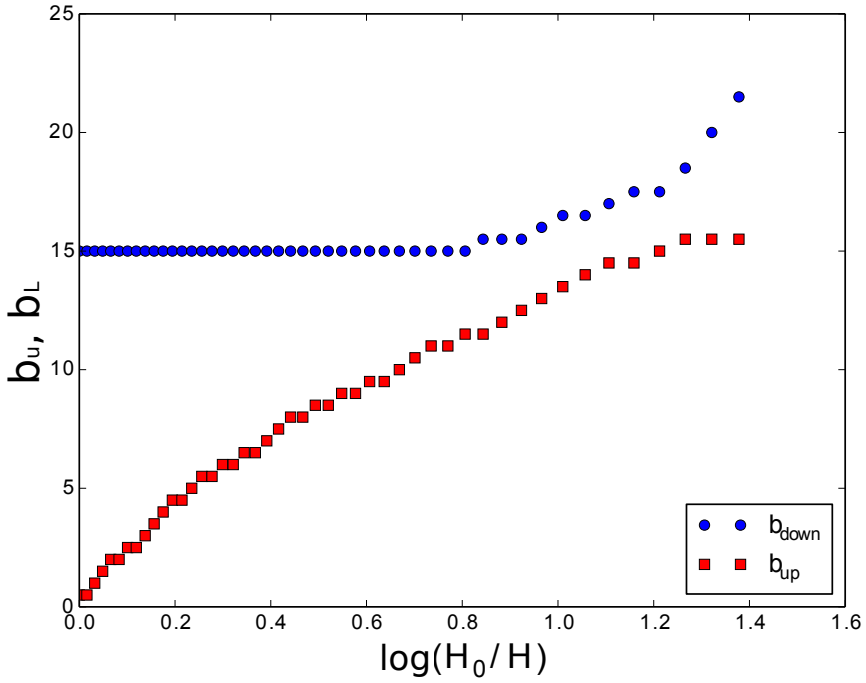

Figure 7.11 Evolution of the upper and lower contact zone radii during the simulation.

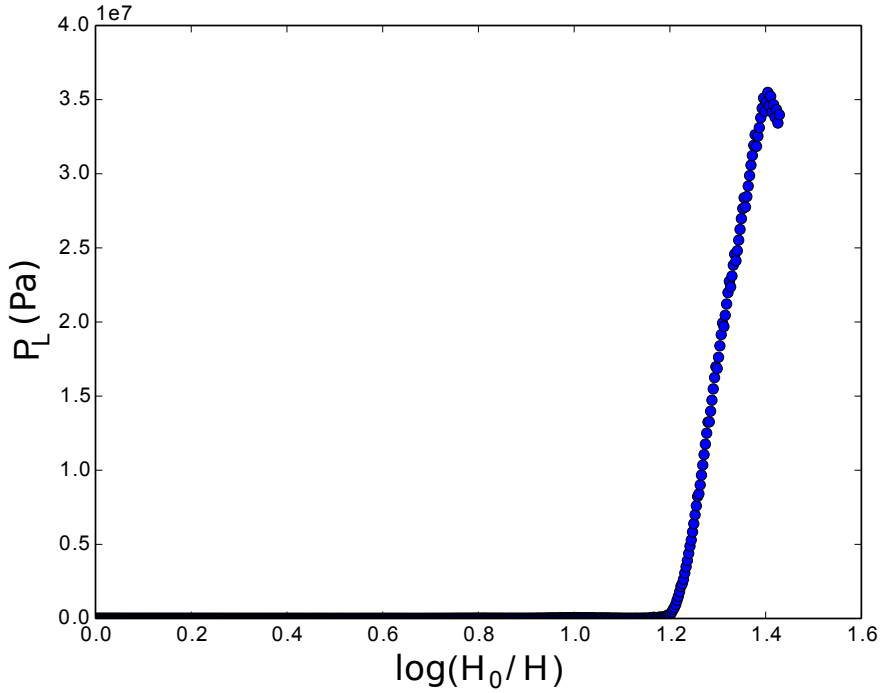

Figure 7.12 The proppant compaction curve of the lower contact zone.

the asymptote (figure 7.14).

These drops of pressure refer to grain avalanches and can be justified with the plots of kinetic energy [20, 21] . The work of [21] show that there is a strong correlation in time and space between the kinetic energy and the negative values of second order work (figure 7.15).

In a continuum , the second-order work is linked to Hill's condition of stability [34]:

$$d^2W = d\sigma : d\varepsilon \tag{7.14}$$

When the second-order work is positive for any value of σ and ε linked by a constitutive relation, the material point is considered stable. When failure occurs, the second order work is negative and deformation continues without any input of energy from outside.

In the case of pile of proppant (slope), the failure is diffuse and the failure is generally characterized by granular avalanches, whether they are local or global. These avalanches can be detected by the kinetic energy.

The kinetic energy of a particle given by :

$$E_{kin} = 0.5mv_g^2 + 0.5I\omega^2 \tag{7.15}$$

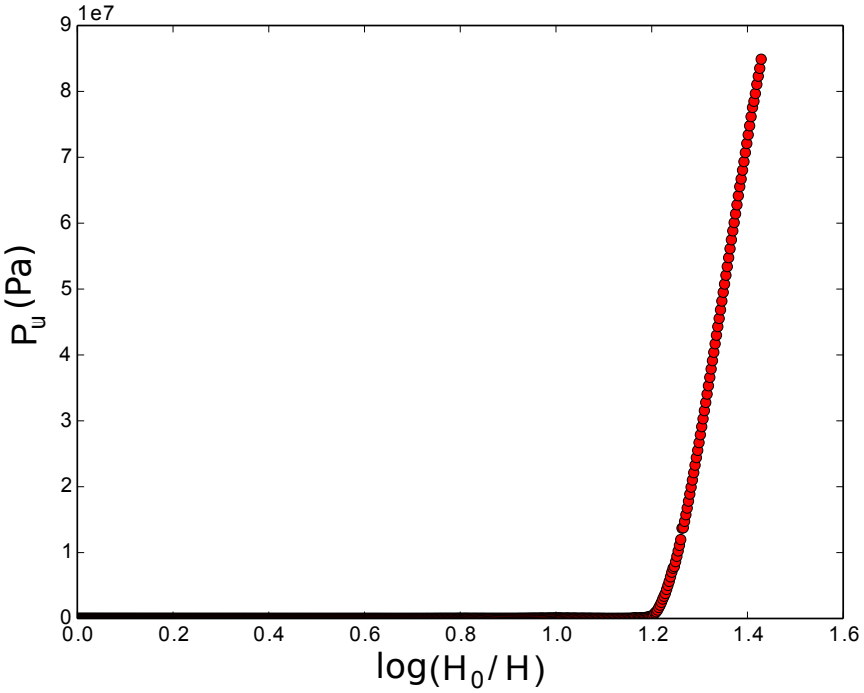

Figure 7.13 The proppant compaction curve of the upper contact zone.

where v_g is the grain velocity, m the mass, I the moment of inertia and ω the rotational velocity. The total kinetic energy is the sum of the kinetic energies of the particles.

It is obvious from this formulation that brutal motions of one or many grains will lead to an increase in the total kinetic energy. Small peaks will lead to limited motions of some particles and more important ones will lead to larger grain motions or grain avalanches.

Figure 7.16 shows that kinetic energy curve is strongly correlated with the pressure drops. When the kinetic energy is low the proppant compaction curve is linear. After some time, the avalanches start and the trend of the proppant compaction curve changes and the pressure increases to reach a pic and decreases again when the avalanches stop. The curve of kinetic energy show also high kinetic energy in the last part of the curve which are some avalanches and mainly the instability of the grains that left the pile and are rolling and rebounding on the plate.

7.4 Stress distribution

The stress distribution on the lower and upper plate is very important question and is the main objective of this study.

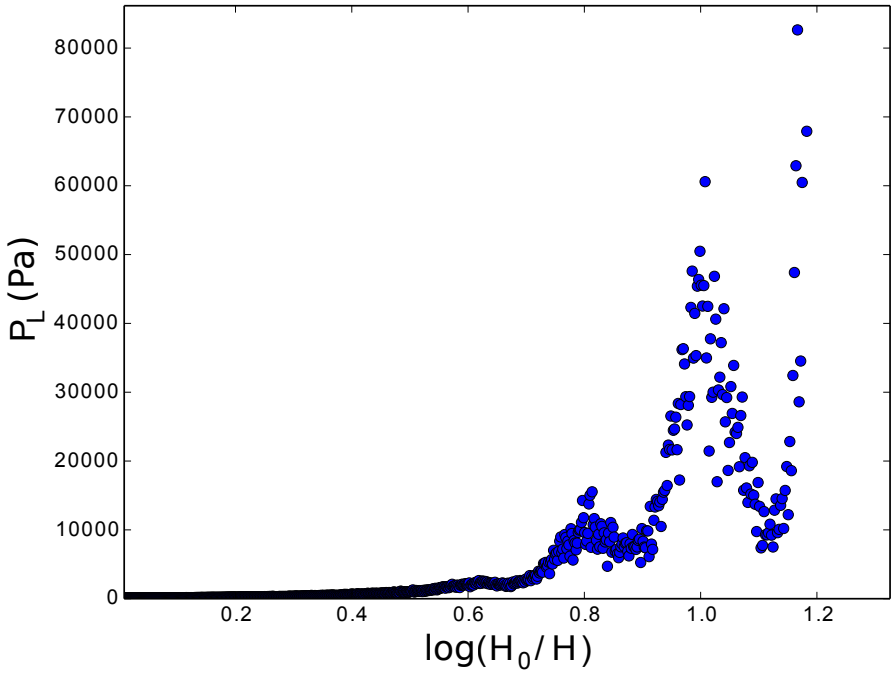

Figure 7.14 The proppant compaction curve of the lower contact zone.

The stress distribution on the lower and upper plate are plotted for various values of $Log(H_0/H)$. We consider different points on the contact area, and squares around each point in which we compute stress by dividing the total normal force on the particles inside the square over the area of the square (figure 7.19).

$$\sigma_{u,L} = \frac{\sum F_p}{A_{square}} \tag{7.16}$$

The stresses are expressed in Pa. The crucial question is the number of particles that should be taken into account within a square. If the number of particles is not sufficient, the stress distribution will be quite noisy. Different square sizes are tested until the value of stress stabilizes . The square size should not exceed the size of the contact zone. If the squares are too big the values of the stress in each square will start converging toward the value of the mean stress. 100 particles is a good number, which means squares of 10 x 10 particles dimensions.

The problem is axi-symmetric, and the value of the stress we get is almost the same in any direction we consider for the points lying on the same circle centered at the center of the contact zone (figure 7.18). A two dimensional plot of the stress distribution along one

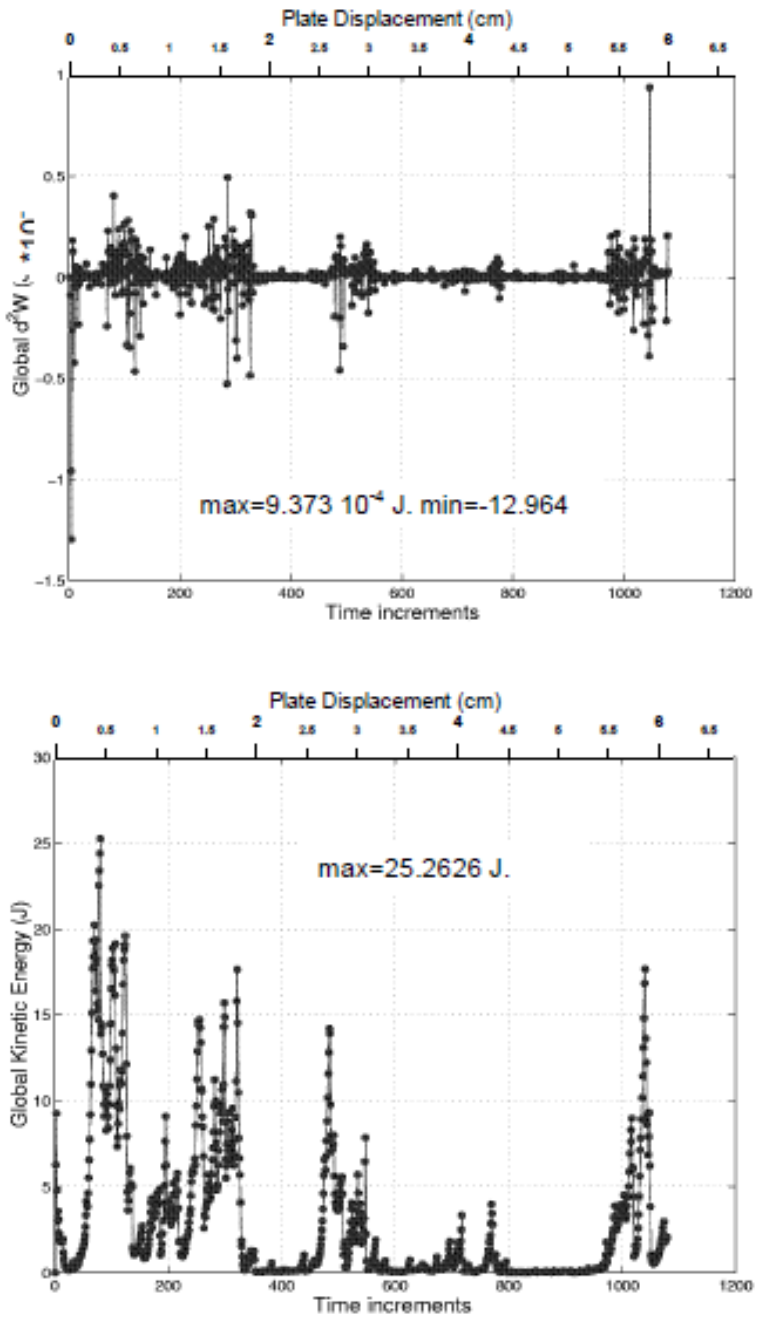

Figure 7.15 The global second order work and the kinetic energy versus the plate displacement.(from [20])

diameter direction is presented below for the lower and upper contact zone for different H values.

The results are consistent with the results of [45] (figure 7.20). The comparision here is qualitative,a two dimensional plane strain compression of ideal soil between two rigid

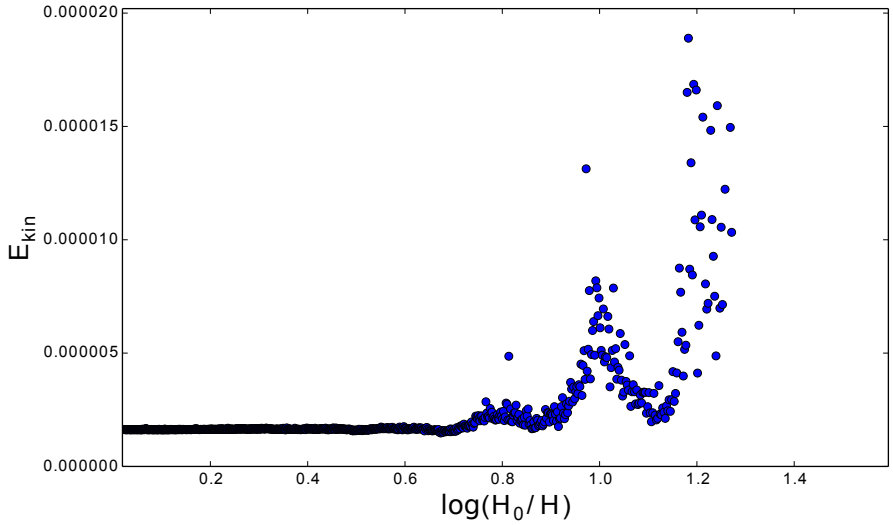

Figure 7.16 The kinetic energy on the lower contact zone.

parallel plates with sliding friction at the plates was considered in [45]. The shape of the curves in both cases (slab compression and pile of proppant compression) show very big similarities.

7.5 Influence of the plate friction angle

The proppant compaction curve is dependent of many factors. The plate friction is one of the important factors. The results presented above were for the case where the frictional constant at the plates was 30 degrees.

The same simulation is repeated for three different values for the plate friction angle (20,30,40) degrees, and the proppant compaction curves for the upper and lower contact zones are presented in figure 7.21. The inter-granular friction is kept equal to 30 degrees.

When the friction angle of the plate is changed, the initial deposited configuration is changed as well. Lower the friction angle, higher is the initial radius of the contact zone with the lower plate and lower is the value of H_0. The difference in our model between the three configurations is not very remarkable (table 7.1).

During the compaction process, the low friction of the plate will allow the grains to

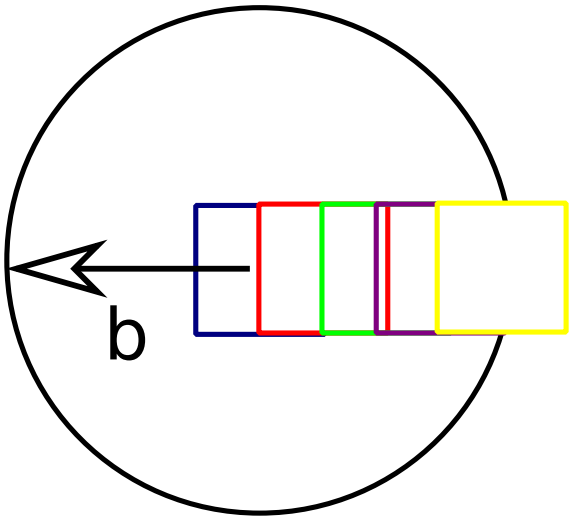

(a)

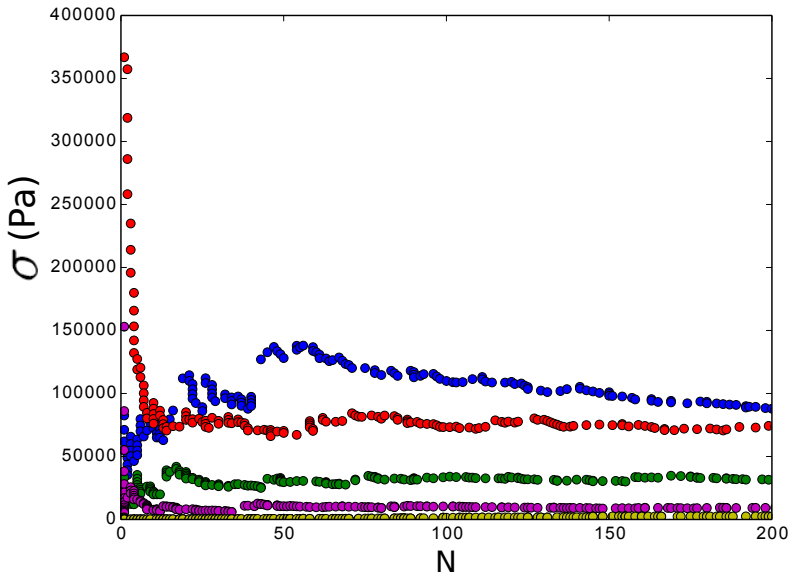

(b)

Figure 7.17 (a) Illustration of the square taken into account to calculate the stress distribution in the contact zone. (b) Stress value in different squares as function of the number of the particles inside the square.

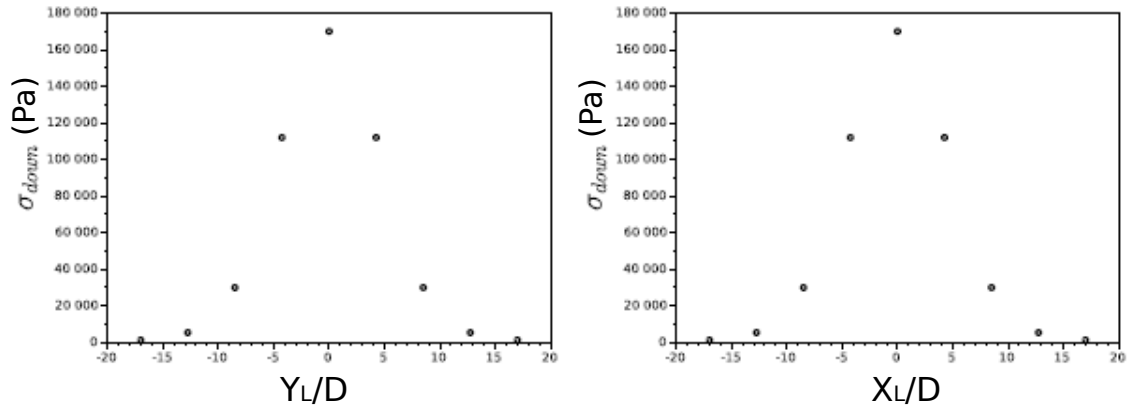

Figure 7.18 Stress distribution on the lower plate in X and Y directions

Table 7.1 The initial deposited configuration of the pile of sand for different plate friction.

friction angle	b_0	angle of repose
20	12	29
30	12	29.1
40	12	29.1

slide easily on the plate which will also lead to a higher contact zone. So for the same load applied on the upper plate, the displacement of the upper plate will be higher in the case of the lower friction (lower H, higher $Log(H_0/H)$) The value of the asymptote of the proppant compaction curve is also higher. And that is what we observe when the proppant compaction curves for the three friction angle values are compared.

The proppant compaction curves for both 30 and 40 degrees friction are almost the same, while in the case of 20 degrees friction , the difference is quite obvious (figure 7.21). The three curves are quite close until the curves start to reach their asymptotes. In the case of 30 or 40 degrees, the displacement of the upper plate is blocked, but the case of 20 degrees, the grains in contact with the plates start sliding and a big grain avalanche occur and the plate continue to move to reach a smaller H value before the displacement of the upper plate stops.

7.6 Influence of the inter-granular friction angle

The inter-granular friction is also a very important parameter. In this section, the plate friction is kept equal to 30 degrees and three values of inter-granular friction are chosen: 20,

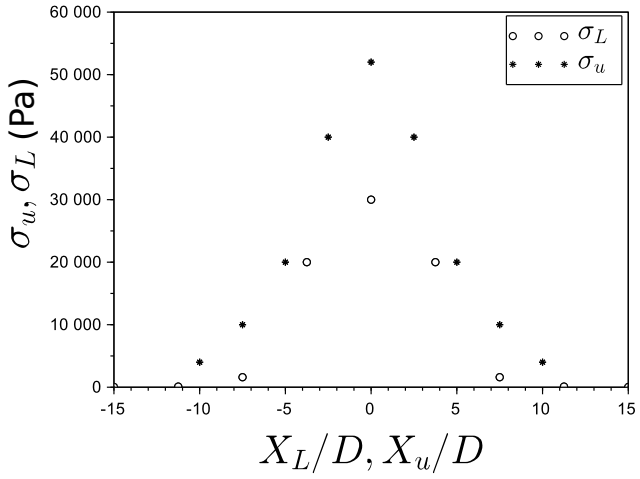

(a)

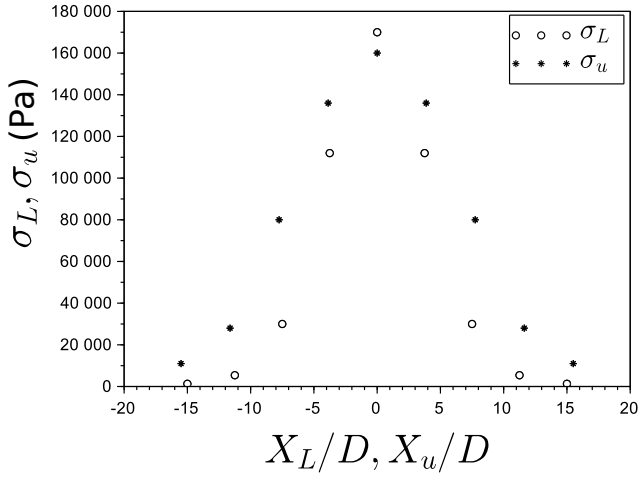

(b)

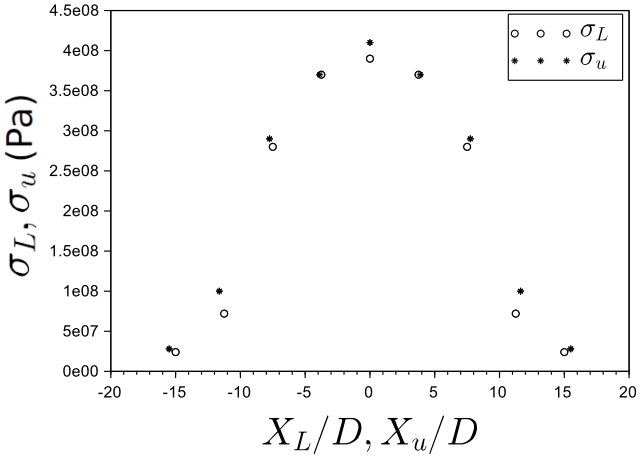

(c)

Figure 7.19 (a)Stress distribution on the upper and lower zone for $Log(H_0/H) = 0.63$(c)Stress distribution on the upper and lower zone for $Log(H_0/H) = 1.17$ (e)Stress distribution on the upper and lower zone for $Log(H_0/H) = 1.44$

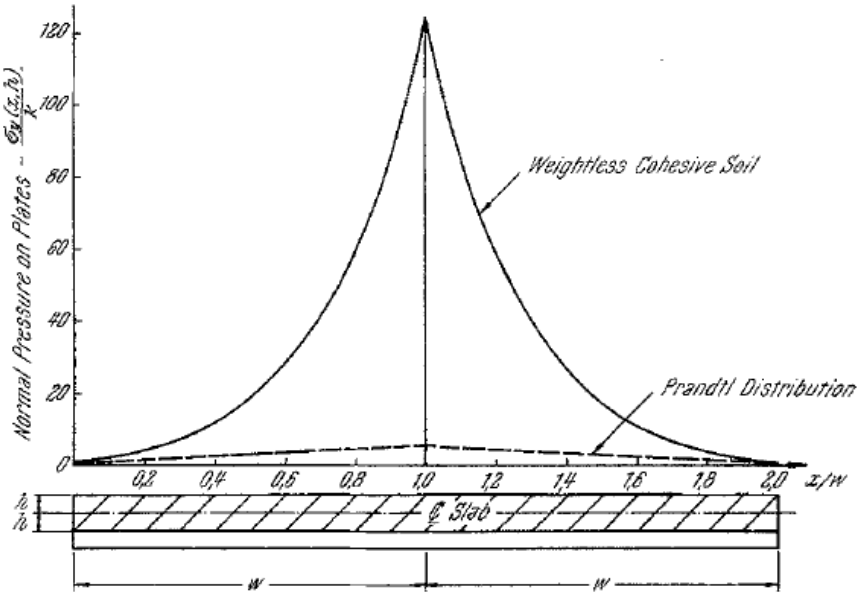

Figure 7.20 The distribution of normal stresses on the compression plates used to compress a slab of a cohesive soil, and compared to PRANDTL distribution for an ideal metal. (from [45])

30, 40.

When the inter-granular friction decreases, the resistance to the sliding of the grains between each other and related to the wall will be reduced, and this will lead to higher displacement of the upper plate and higher contact zone.

The plots of the proppant compaction curves show similar results to the ones presented in the previous section, when the friction angle of the plate is changed. In the case of 20 degrees inter-granular friction angle, we also observe the instabilities near the end, due to grains sliding and grain avalanches that occur.

Before reaching the asymptotes of the curves, the difference between the three curves is more obvious than in the case of different plate frictions, because in the case on different plate friction, the grains that are in contact with the plates are mainly affected by the change, while for a different inter-granular friction, the whole system is directly affected by the change, which makes a bigger difference.

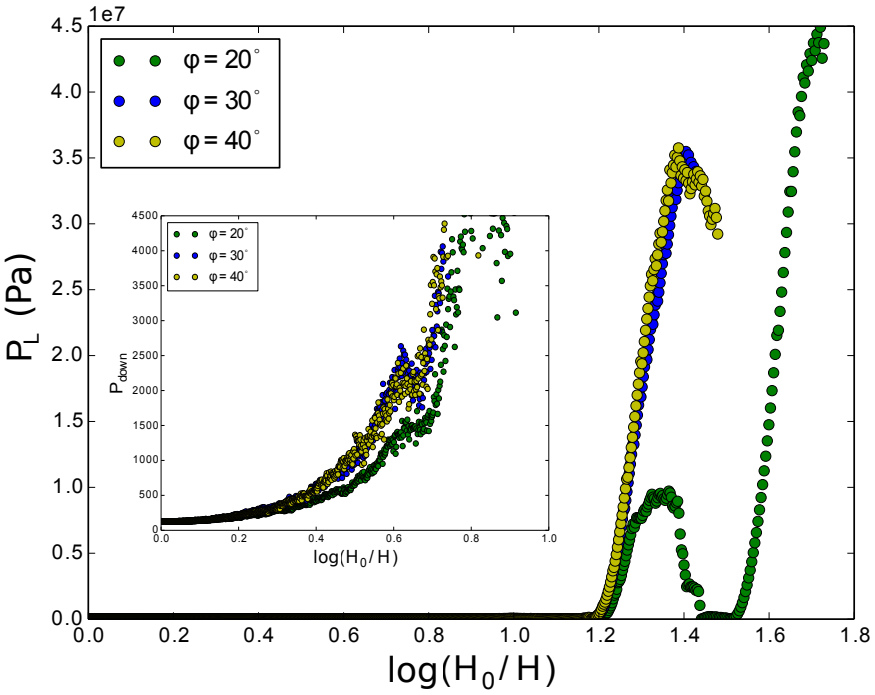

(a)

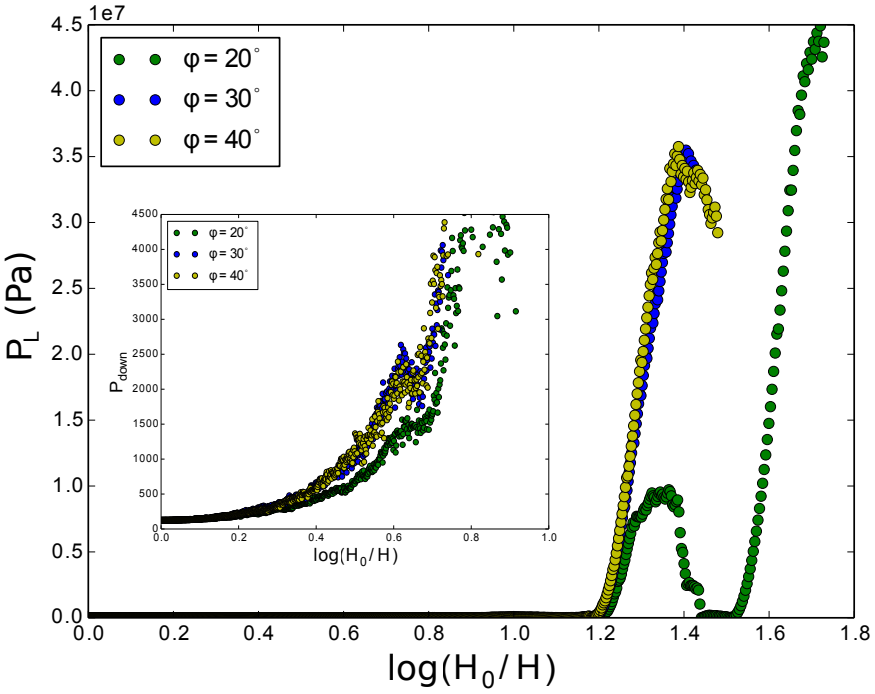

(b)

Figure 7.21 The proppant compaction curves for different plate sliding friction.

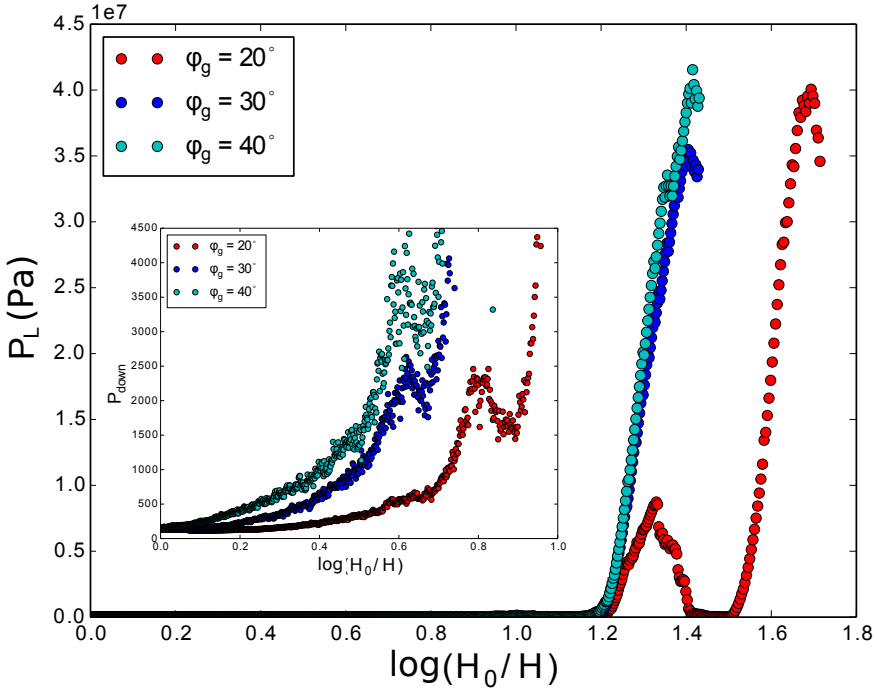

(a)

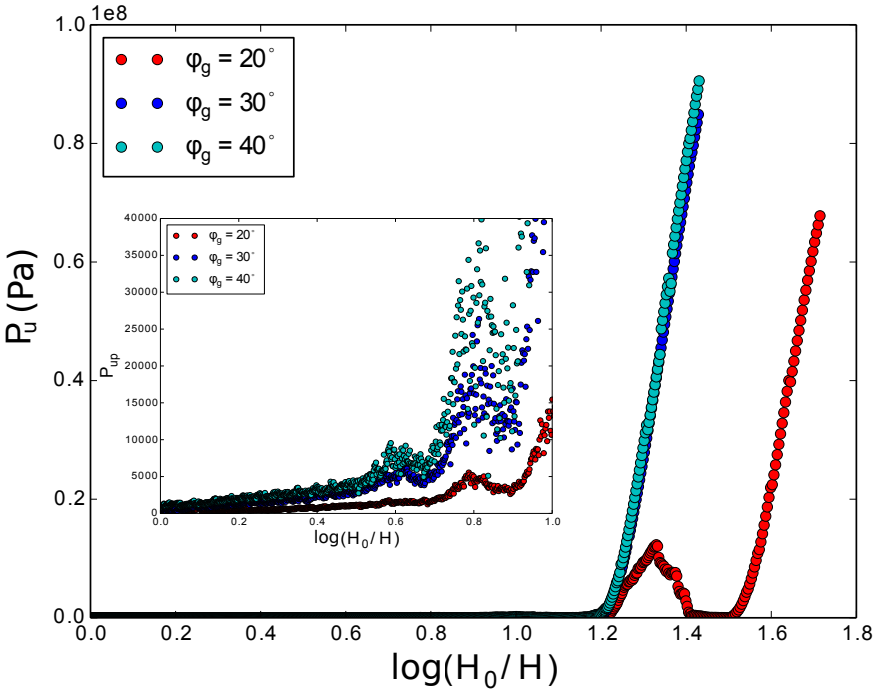

(b)

Figure 7.22 The proppant compaction curves for various inter-granular friction angles.

Chapter 8

Simulation of the compression of proppant between two similar elastic rock blocks.

8.1 Introduction

The compaction of a proppant between two rigid plates has been examined in the previous chapter, and the stress distribution on both plates has been evaluated. These results can be used in separate FEM simulations to determine the fracture opening due to the presence of the proppant and to provide improved estimates for the interaction of proppant with the fracture. Another way to treat the problem is to simulate the complete problem using DEM by improving the model and replacing the rigid plates by an elastic rock block.

In this chapter, we examine the problem of the compression of a granular proppant region between two similar elastic rock blocks. The proppant region is essentially a granular material that will possess a subsequently lower rigidity to the rock surfaces that induce compression due to geostatic stresses. The deformed fracture configuration is related to the characteristics of the rock blocks and primary properties of the proppant, including particle size distribution, elasticity of particles and interface frictional characteristics that were studied in the previous chapter. The determination of fracture opening should allow the evaluation of its effective permeability which is an important parameter in a resource extraction exercise.

When the deformations of the rock medium stabilize after the injection of the proppant, the deformations of the formations can be estimated from the behavior of the elastic skeleton. The transition afterwards when the pressure of the injected fluids decreases is not immediate, but since the interest of this study is to determine the opening of the fracture, the extreme elastic study case provide useful results.

Researchers have examined the problem of the compression of a "rigid" object between elastic media [29]. Several works have been done to examine this problem of a smooth precompressed elastic interface and determine the opening of the fracture. The separation of a bi-material elastic interface by a spheroidal shape axisymmetric , non symmetric with respect to the interface was studied in [29]. Selvadurai [79] examined the problem by considering a disc shaped rigid body between two dissimilar elastic half spaces (half spaces that have different elastic properties (G, E, ν)).

Before simulating the interactions between the rock block and the granular proppant, in order to ensure that the discrete element code have capabilities of treating the interaction of a particulate system with a linear elastic continuum element, an axisymmetric static problem of a disc inclusion between two similar elastic rock blocks is studied in the first part of the chapter and the results are compared to the work of [79]. In the second part of this chapter the compaction of granular proppant between elastic rock blocks is studied.

8.2 Simulation of the compression of a rigid disc inclusion between two similar elastic rock blocks.

8.2.1 Model description

The problem of disc inclusion between two similar elastic spaces is an axysimmetric problem (figure 8.1) with respect to the interface, thus computational costs can be reduced by considering only one elastic rock block. An inclusion of a disc of half thickness is then simulated.

The elastic continuum (rock block) is constructed by creating a cloud of spheres of a given tightly graded grain size distribution (the dispersion from the mean radius is 1 %) and random position in a domain of a given dimension. The grains are then allowed to grow progressively inside the domain until they form a dense packing filling the cube, and we

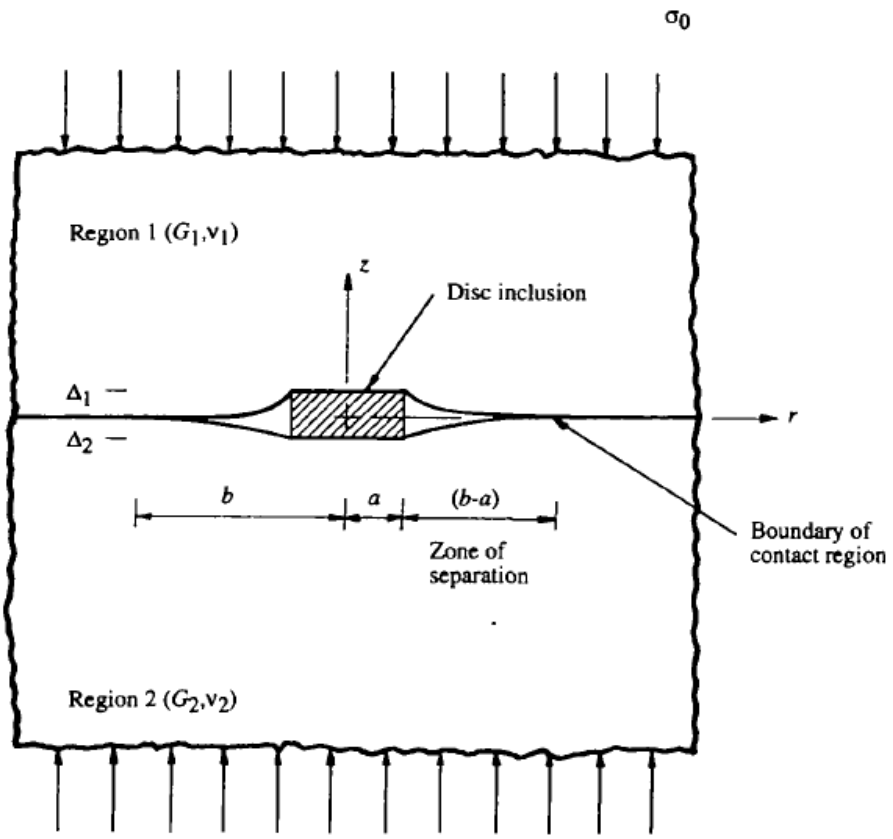

Figure 8.1 A disc inclusion between two elastic semi infinite spaces (from [79]).

Figure 8.2 Illustration of the rock block with the defined dimensions.

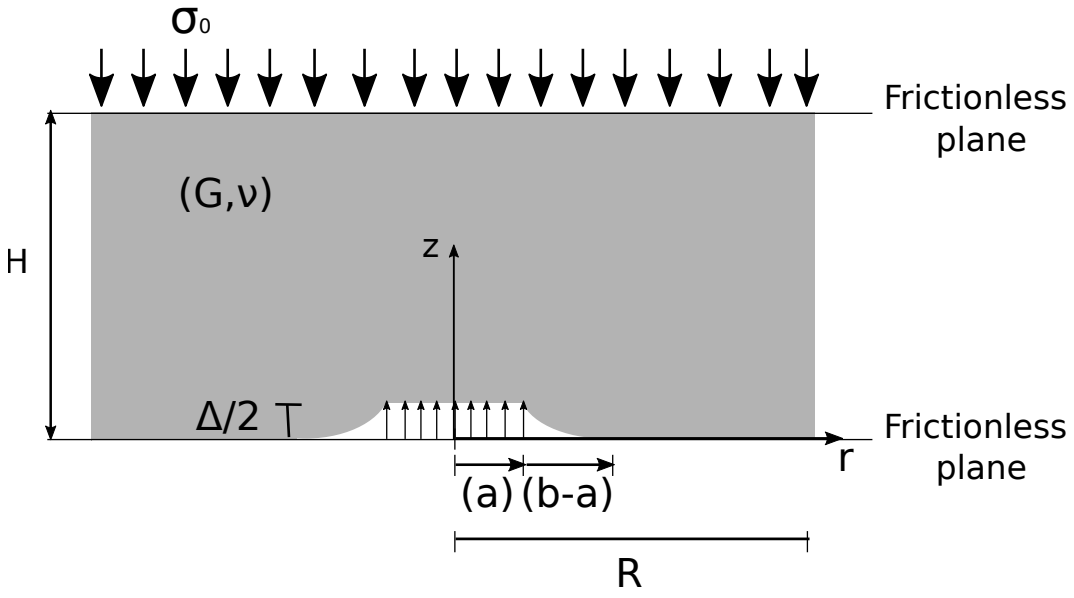

Figure 8.3 Illustration of the model.

reach a predefined confinement pressure. The intergranular normal stiffness (k_n) is set to $10^9\ N/m$, the intergranular shear stiffness (k_t) is set to $0.5k_n$ to create a nearly incompressible rock block. The linear elastic-plastic contact law is used for the models.

Once the packing is dense, the spherical particles are glued together by applying a very high cohesion to all the contacts. When the rock is deformed, new contacts might occur, but no cohesive contact will be created.

When the packing assembly is ready, frictionless rigid planes are placed on the upper and lower surfaces of the packing. The base is fixed to ensure the axisymmetric conditions and the upper wall can only move in the vertical direction. The dimension of the rock block are chosen in a way to eliminate the boundary conditions effects during the simulation so the side boundary conditions can be either fixed or free. If $2a$ is the diameter of cylinder, the rock block is of $10a$ of thickness and of $22a$ of length and depth (figure 8.2).

The disc inclusion is simulated by applying a uniform displacement to the particles of the block that are in contact with the lower boundary and verify the following condition: $x^2+y^2 \leq a^2$ (The initial pressure applied on the rock block is equal to $\sigma_0 = 1.5e3KPa$)

When the displacement of the grains is equal to the desired thickness ($\Delta/2$), the position

of the displaced particles are fixed in the rest of the simulation (figure 8.4).

The boundary conditions are the following:

$$\sigma_{zz}(r,H) = \sigma_0 \qquad r \in (0,R) \tag{8.1}$$

$$\sigma_{rz}(r,z) = 0 \qquad r \in (0,R) \tag{8.2}$$

$$\sigma_{rr}(R,z) = 0 \qquad z \in (0,H) \tag{8.3}$$

$$\sigma_{rz}(R,z) = 0 \qquad z \in (0,H) \tag{8.4}$$

$$\sigma_{rz}(r,0) = 0 \qquad r \in (0,R) \tag{8.5}$$

$$\sigma_{zz}(r,0) = 0 \qquad r \in (0,b) \tag{8.6}$$

$$u_{rz}(r,z) = \Delta/2 \qquad r \in (0,a) \tag{8.7}$$

In the next step, the upper wall is subjected to a displacement until the value of the zone of separation (b-a) tends to zero. The stresses σ_0 applied to the upper wall and the position of the grains in contact with the lower wall are saved during the loading process in order determine the fracture opening and related to the total stress applied to the upper wall.

The simulations are repeated for two values of Δ/a, 0.1 and 0.2.

The comparision with the analytic results of [79] requires the elastic properties of the rock block and the value of separation.

8.2.2 Elastic properties of the rock block

The elastic properties of the rock block are evaluated by performing a triaxial test on the rock block. The pressure is kept constant and equal to the initial confinement pressure on the sides and a vertical displacement is applied in the vertical direction z.

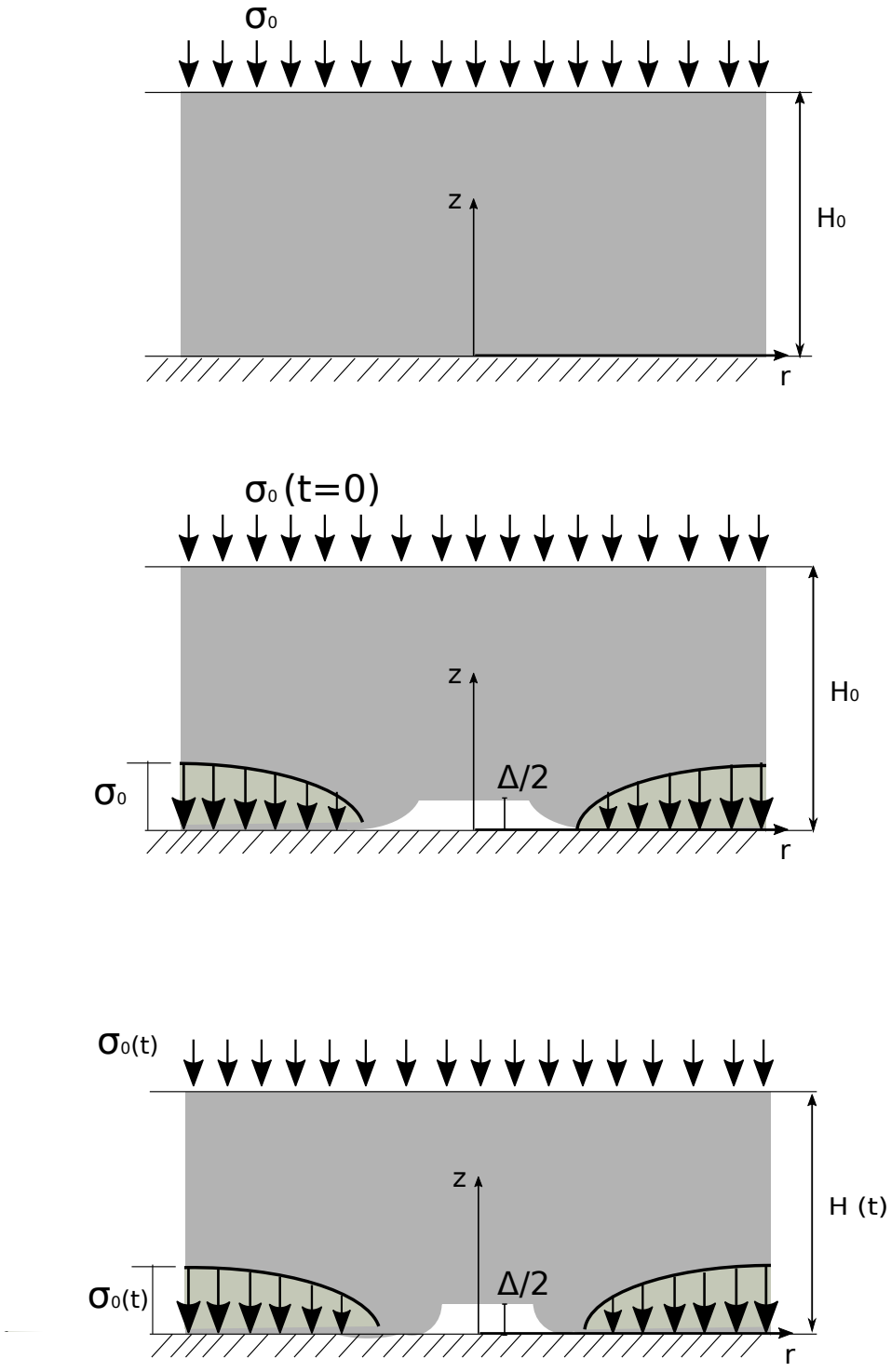

Figure 8.4 Illustration of the different stages of the disc inclusion simulation.

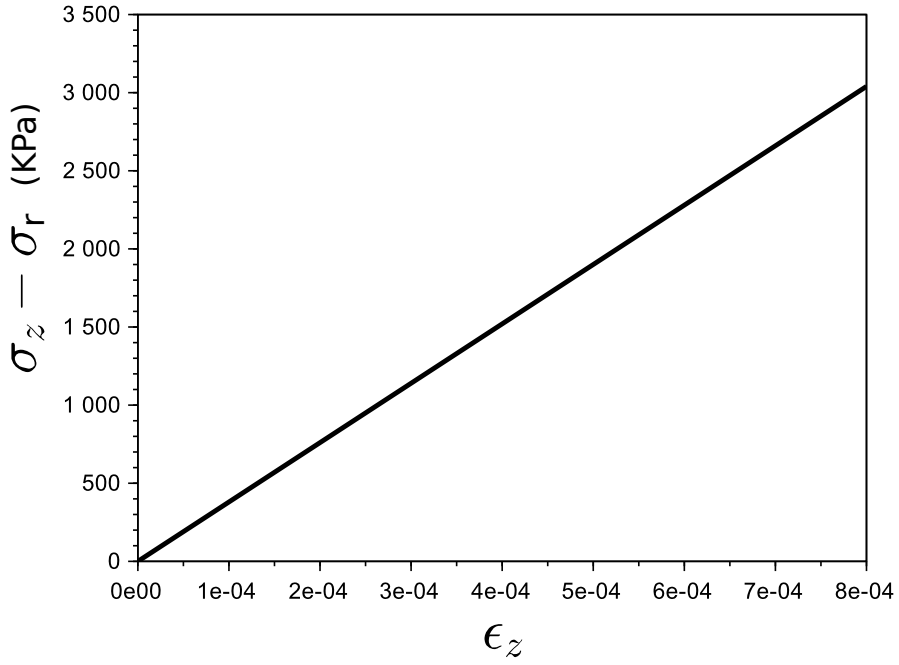

Figure 8.5 $(\sigma_z - \sigma_r)$ as function of the vertical strain.

$(\sigma_z - \sigma_r)$ is plotted as function of the vertical strain ε_z (figure 8.5). The slope of the linear curve is equal to the young modulus E ($E = 4e5KPa$).

Poisson's ratio is calculated by plotting the lateral strain as function of the vertical strain (figure 8.6) ($\nu = -\frac{\varepsilon_x}{\varepsilon_z}$). We find $\nu = 0.45$. The obtained Poisson's ratio is very close to 0.5.

The shear modulus of the rock block is calculated for homogeneous and isotropic material as following:

$$G = \frac{E}{2(1+\nu)} \tag{8.8}$$

We find $G = 1.5e5KPa$.

8.2.3 Fracture opening and stress distribution

The stress distribution on the base surface ($z = 0$) is evaluated during the loading. To evaluate the stress distribution, we consider several rings in which the stress is calculated as the

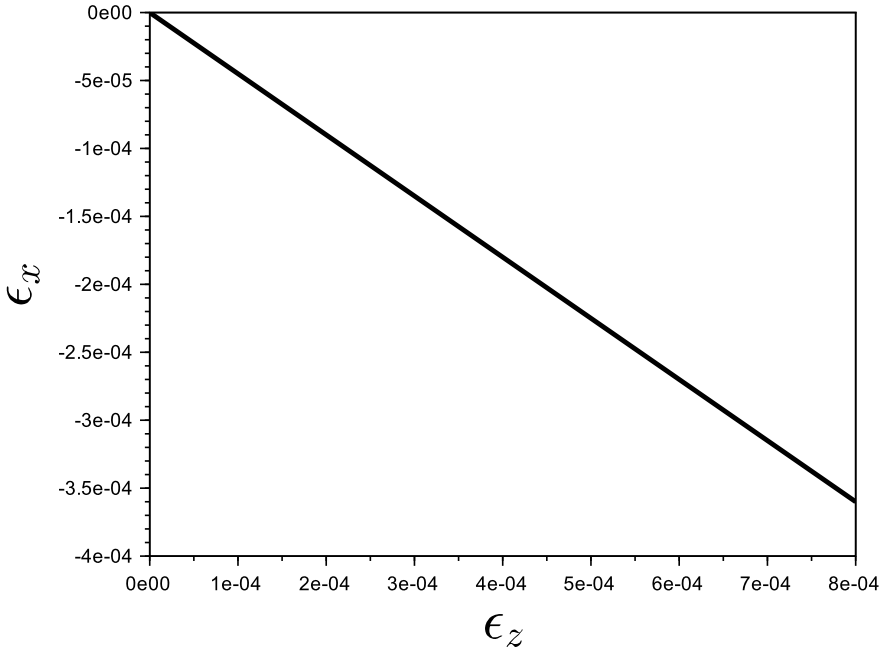

Figure 8.6 The lateral strain as function of the vertical strain.

sum of all the normal forces applied by the particles on the base surface over the area of the ring (figure 8.7).

As it is the case in the chapter 7, the crucial question is the number of particles that should be taken into account within each ring in order to have a smooth stress distribution representation. For this reason the rings are allowed to overlap.

Figure 8.8 shows the stress distribution on the lower boundary for different values of σ_0. The stress is equal to zero when the rock block is not in contact with the lower boundary ($0 < r < b$), where b is the radius of the zone that is not in contact with the lower boundary (the fracture opening). Once the rock block is in contact with the base, the stress starts to increase linearly until it reaches a maximum value and remains almost uniform and equal to σ_0 until we reach the edge of the elastic domain ($r/a = 11$) and then decreases again to zero when the rings are outside the domain.

The stress distribution curve can be used to determine the value of the fracture opening b. Higher is the value of σ_0, lower is the value of the opening.

The opening b can be also determined by considering successive rings of the thickness of two grains diameters. If the ring contains enough grains it is taken into account, if not it is neglected. As it is done in the previous chapter the condition to verify is that surface of the m grains inside the ring cover at least 2/3 of the total surface of the ring :

$$\Sigma_1^m \pi r_i^2 > \frac{2}{3} A_{ring} \tag{8.9}$$

Both approaches give very similar results. The comparison between both methods is given in table 8.1

Table 8.1 The values of the opening obtained from the stress distribution curve and from the ring method.

Δ/a	σ (KPa)	b/a (from stress dist. curve)	b/a (from the ring method)
0.2	1.5E3	3.9	3.84
0.2	5.5E3	2	2.04
0.2	20E3	1.4	1.44
0.2	27E3	1.2	1.2
0.1	1.5E3	2.7	2.64
0.1	5.5E3	1.7	1.68
0.1	20E3	1.16	1.2
0.1	27E3	1	1.08

8.2.4 Validation of the results

Once the opening of the fracture and the elastic properties of the rock block are determined, the numerical results can be compared to the analytic results of [79] (figure 8.9).

The selected analytical results of [79] in figure 8.10 are the results that correspond to the case of similar rock blocks where the axial displacement of the rock formation beyond the opening zone is equal to zero, which is exactly the case in the simulations.

The plots show that the numerical results of the DEM simulations fit very well the analytic curve.

The validation of results is limited to a value of b/a equal to 4. This is not a limitation of the DEM model, but for higher values of b/a the length of the rock block is not sufficient to neglect the boundary conditions effect. Having a complete curve as in figure 8.10 will

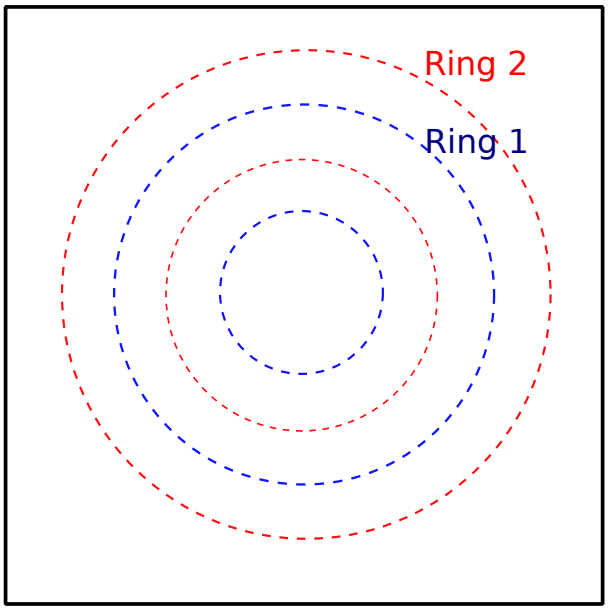

Figure 8.7 Illustration of the interface view of the rock block showing the rings considered to evaluate the stresses.

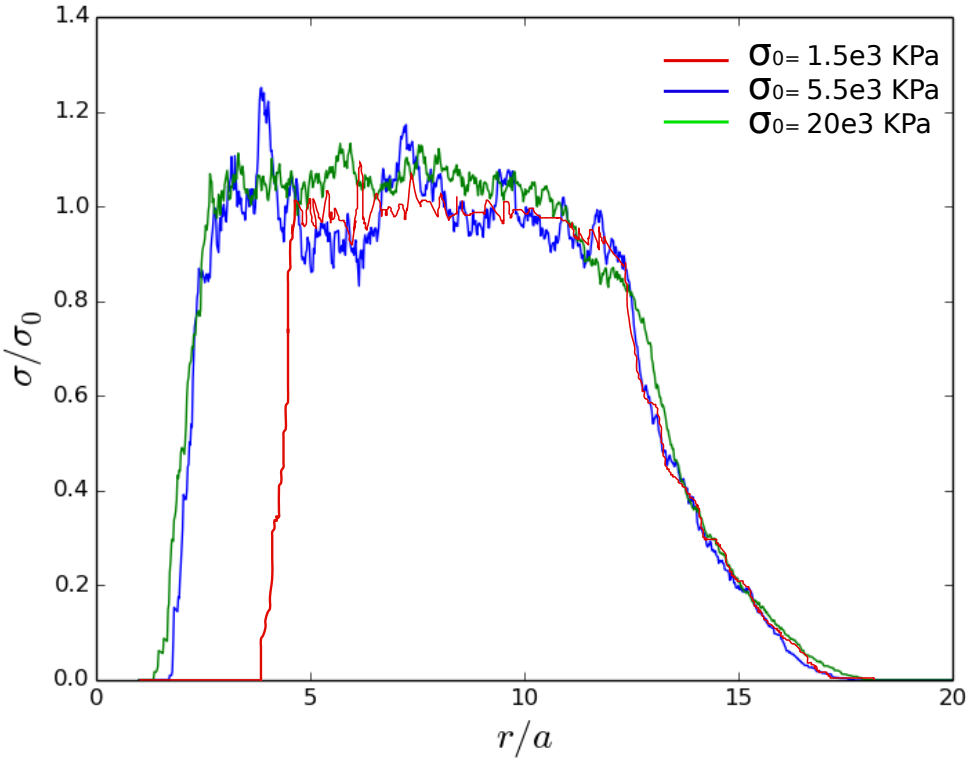

Figure 8.8 Stress distribution on the interface.

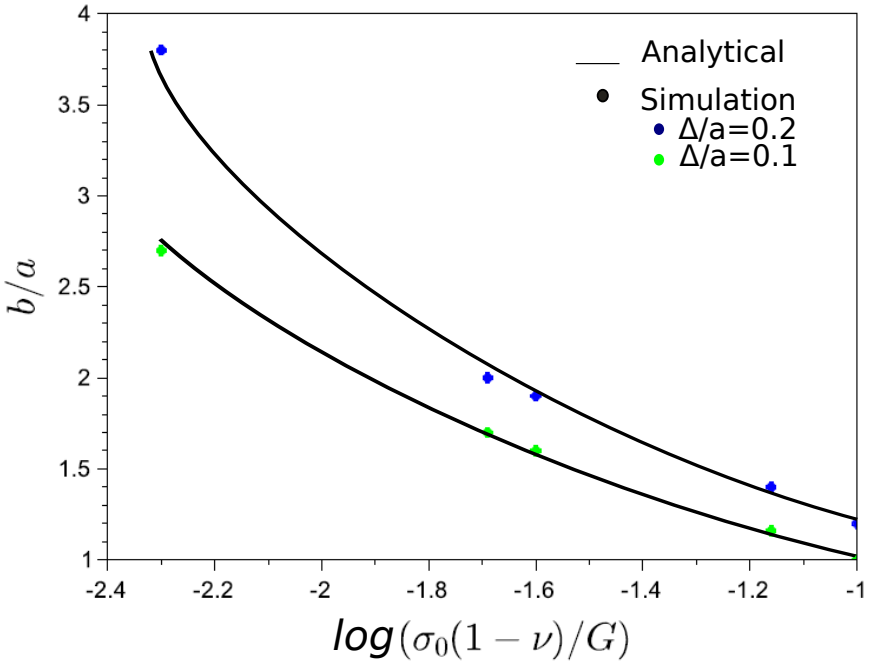

Figure 8.9 The validation of the numerical results: comparision with the analytic results of [79].

require a much bigger model, a larger number of particles and a much longer computational time.

8.3 Simulation of the compression of granular proppant between two similar elastic rock blocks.

8.3.1 Model description

The problem of compaction of granular proppant between two similar elastic spaces having the same elastic properties (G, E, ν) is treated in this section. We consider that the problem is an axysimmetric problem with respect to the interface to reduce the computational costs. Only one elastic rock block is considered.

The same elastic block used in the previous section is used for the following study as well.

Frictionless rigid planes are placed on the upper and lower surfaces of the packing. The

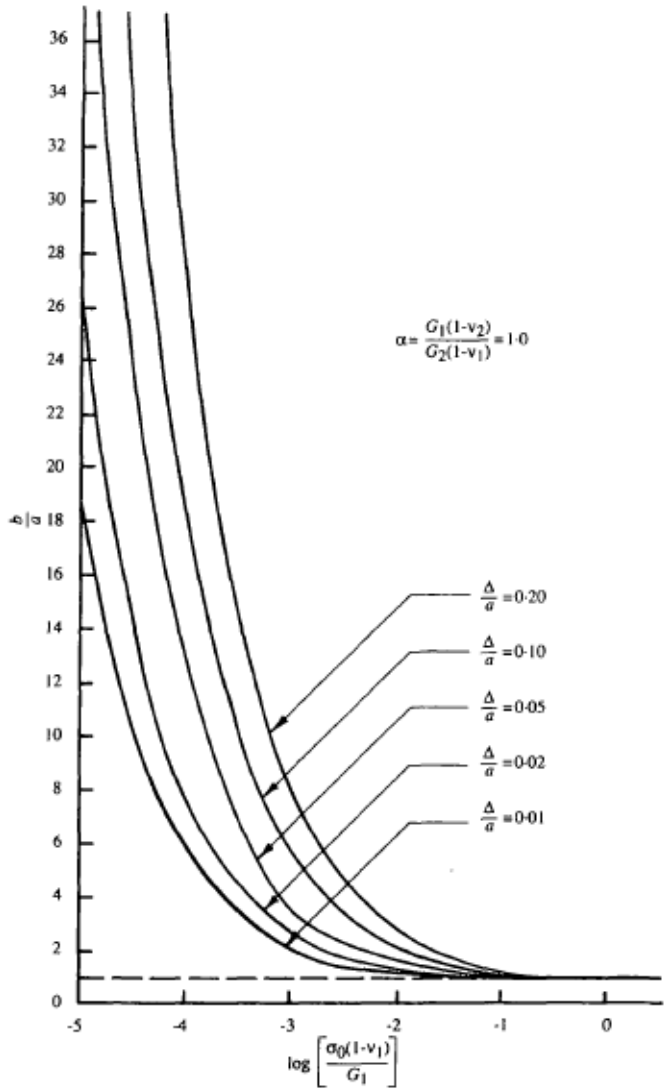

Figure 8.10 Results for the zone of separation at the interface for different disc thicknesses(from [79])

base is fixed to ensure the axisymmetric conditions and the upper wall can only move in the vertical direction. The initial applied pressure is also equal to $1.5e3KPa$.

In the next step, a cavity is created and the proppant is deposited by gravity inside the cavity through a borehole. The volume of the deposited proppant is equal to the volume of the rigid disc shaped proppant of $\Delta/a = 0.2$.

The shape of the cavity at the moment of the deposition of the proppant is considered to be the same as in the case of a disc inclusion of $\Delta/a = 0.2$. A uniform displacement is then applied to the particles of the block that are in contact with the lower boundary inside the domain ($x^2 + y^2 \leq a^2$) as in the case of disc inclusion (case of $\Delta/a = 0.2$).

The positions of all the particles of the rock block are fixed afterwards and a borehole centered in the middle of the cavity is created by removing the grains inside the domain ($x^2 + y^2 \leq (a/4)^2$).

Once the borehole created, granular proppant of uniform particle size distribution is deposited by gravity in the cavity through the borehole. When the deposition of the proppant is finished, the borehole is closed again to reproduce the original elastic rock block. The fixed grains of the elastic rock block are released and the geometry of the fracture is defined for the initial given value of the applied stress when equilibrium is reached. The upper wall is afterwards subjected to a vertical displacement (figure 8.11).

The stresses σ_0 applied to the upper wall and the position of the grains in contact with the lower wall are saved during the loading process in order determine the fracture opening and the distribution of the proppant inside the fracture and relate it to the total stress applied to the upper wall.

The boundary conditions are the following:

$$\sigma_{zz}(r,H) = \sigma_0 \qquad r \in (0,R) \tag{8.10}$$

$$\sigma_{rr}(R,z) = 0 \qquad z \in (0,H) \tag{8.11}$$

$$\sigma_{rz}(R,z) = 0 \qquad z \in (0,H) \tag{8.12}$$

$$\sigma_{rz}(r,0) = 0 \qquad r \in (a,R) \tag{8.13}$$

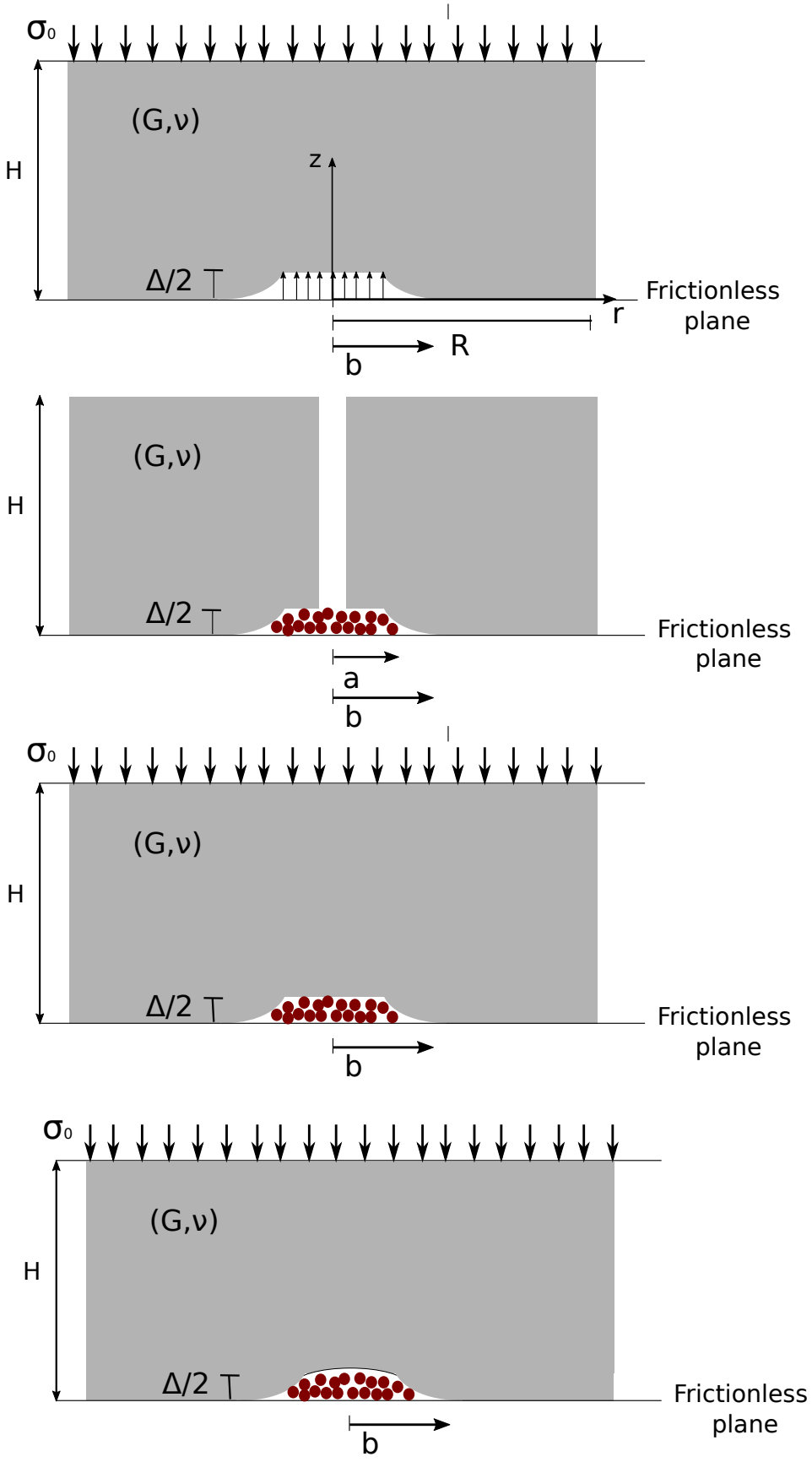

Figure 8.11 Illustration of the different stages of the deposition of the granular proppant.

$$\sigma_{zz}(r,0) = 0 \qquad r \in (a,b) \tag{8.14}$$

8.3.2 Fracture opening

The values of the area occupied by the proppant inside the fracture (a) and the opening of the fracture (b) are determined by considering successive rings of the thickness of two grains diameters. If the ring contains enough grains it is taken into account, if not it is neglected (see previous section).

In the case of disc inclusion problem, the proppant is rigid, then the opening of the fracture Δ and the area occupied by the proppant a are fixed and do not change during the simulation. The extent of the fracture b is the only variable changing with the applied stress. When the rigid disc is replaced by a granular proppant of the same volume, the problem is more complex, and all the variables Δ, b and a are changing during the compression. When the applied stress (σ_0) increases , the aperture of the fractures Δ decreases and a increases.

The results relating b/a to the applied stress on the elastic rock block ($b/a = f(Log_{10}(\sigma_0(1-\nu)/G))$) are presented in figure 8.12 and compared to the analytic results of [79] in the case of a disc inclusion of the same volume. For the same volume of a rigid disc of ($\Delta/a = 0.2$), and for the same applied stress, the ratio b/a is smaller in the case of granular proppant. When the stress increases, b/a approaches the analytic curve and tend to 1 when the stress is too high.

Figure 8.13 shows the evolution of the proppant distribution during the proppant compaction by plotting Δ/a. The ratio is smaller compared to its value in the case of disc shaped proppant, and decreases when the applied pressure increases. It means that the decrease of the aperture of the fracture is faster than the increase of a with the compression of the block. When the applied pressure is too high, this value also tends toward a constant value (around 0.06).

In figure 8.14, we show the evolution of the geometry of the fracture by plotting Δ/b during the compaction of the proppant. The plot shows that this ratio remains almost constant during the simulation ($\Delta/b = 0.06$) and mostly smaller than the value of Δ/b in the case of rigid disc shaped proppant. The evolution is much more important in the case of disc inclusion as shows the analytic curves. However the fact that the ratio (Δ/b) is almost

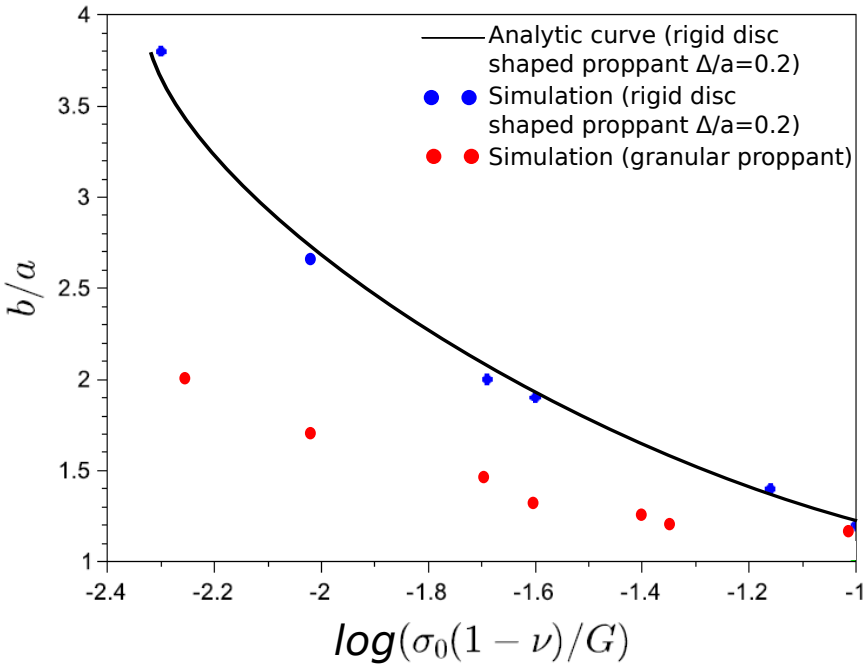

Figure 8.12 Results for the evolution of b/a in the case of granular proppant compaction and comparison with the results in the case of disc inclusion.

constant means that the geometry of the fracture could be predicted during the compaction of the proppant from the initial configuration. If the opening and the extent of the fracture are known for a given overburden stress, their values can be estimated for other values of stresses, for the same volume of the injected proppant.

The evolution of $\Delta * a/D^2$ and $\Delta * b/D^2$ plotted in figures 8.15 and 8.16. These values give an indication on the evolution of the volumes of the proppant and the fracture during the simulation.

The plots shows that the volumes of the proppant and the fracture decreases during the simulation before reaching a constant value when the applied pressure is very high ($\Delta * a/D^2 \approx 40$ and $\Delta * b/D^2 \approx 40$). At this stage, the proppant occupies all the space inside the fracture.

8.4 Conclusion

In this chapter, it is shown that, with suitable constraints, discrete element method is able to reproduce the behavior of an isotropic elastic continuum. The model of a constraint discrete

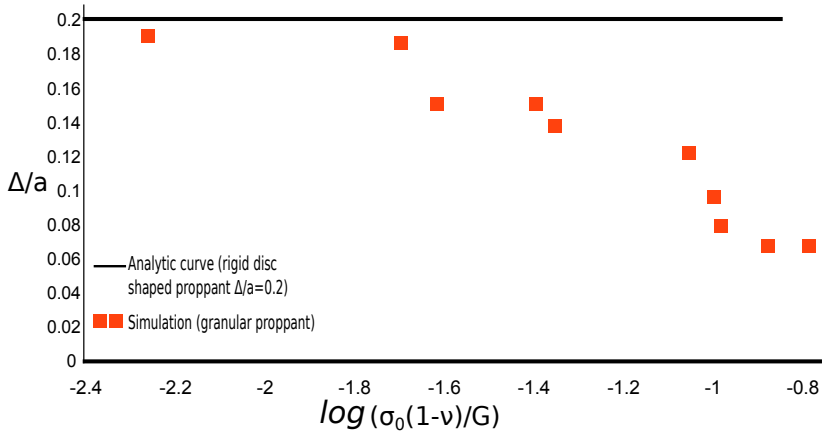

Figure 8.13 Results for the evolution of Δ/a during the compaction of the proppant (disc shaped and granular pile).

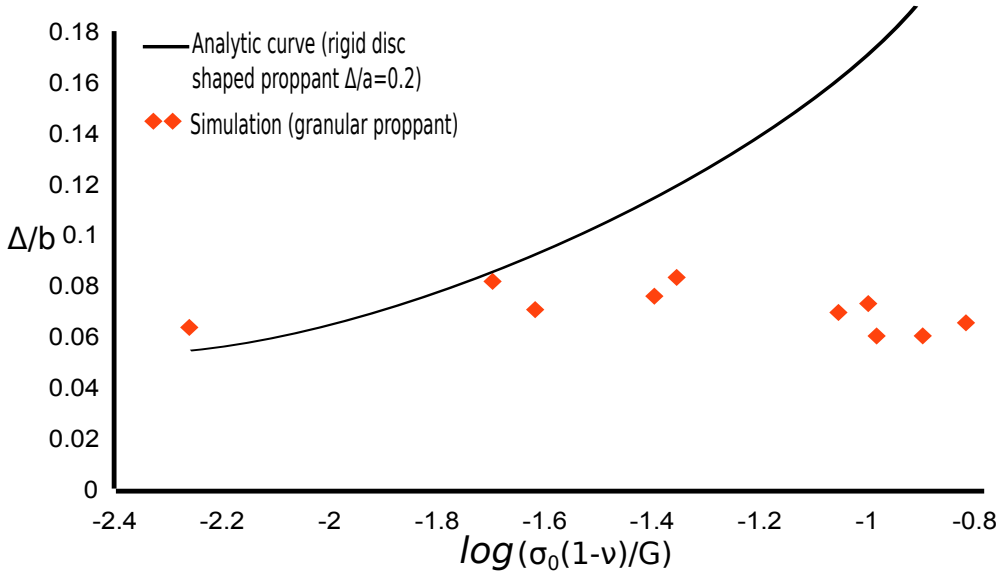

Figure 8.14 Results for the the evolution of Δ/b during the compaction of the proppant(disc shaped and granular pile).

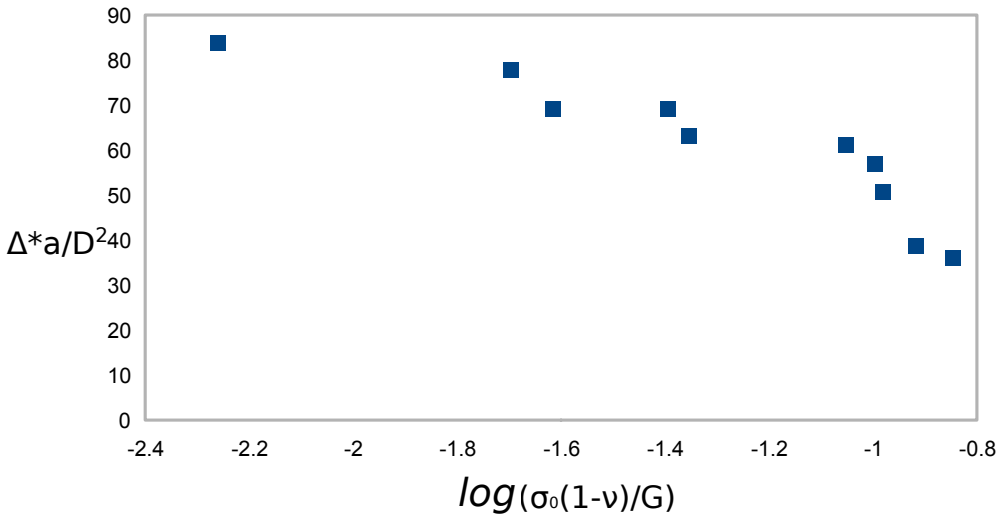

Figure 8.15 The evolution of $\Delta * a/D^2$ during the compaction of the proppant.

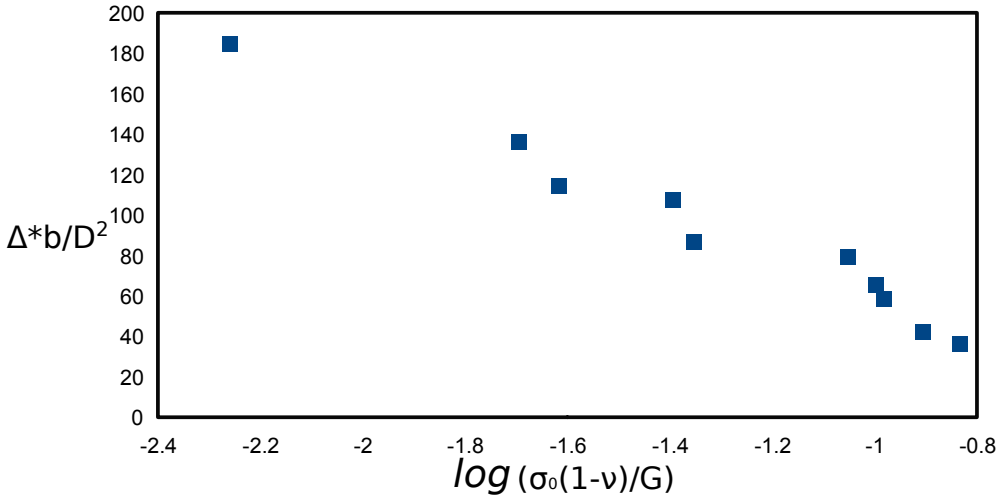

Figure 8.16 The evolution of $\Delta * b/D^2$ during the compaction of the proppant.

system is used to examine the problem of a rigid circular disc embedded in a smooth contact between two similar halfspaces, and subjected to compression. The opening of the fracture is related to the compression stress value and to the elastic properties of the rock block. These results are compared to the analytic results of [79].

The results fit very well the analytic curves. The only limitation of DEM modeling is computational cost that can be very high in terms of time when the opening of the fracture is very long.

In the second part of the chapter, the rigid disc is replaced by a pile of granular proppant deposited by gravity, and the geometry of the fracture is examined. This final model allows to improve the analytic results relating the opening and the extents of the fracture to the overburden stress in the case of granular proppant. It is shown that the ratio b/a of the extent of the fracture to its aperture is lower in the case of granular proppant compared to a rigid disc shaped proppant of the same volume. The distribution of the proppant inside the fracture and the geometry of the fracture were also presented. It is shown, since the ratio Δ/b is almost constant that the geometry of the fracture could be predicted from the initial configuration for several overburden stress values. It is also shown that the volume of the fracture in the case of granular proppant is smaller compared to the case of rigid disc shaped proppant of the same volume.

Chapter 9

Conclusion and Perspectives

This thesis was mainly interested in multi-phase and rock-granular interactions using DEM models.

9.1 Multiphase system

9.1.1 Conclusions

In the multiphase systems, a numerical model for partially saturated soils in the pendular regime was presented. The capillary interaction law is based on the capillary theory. We solved the exact solution of Young-Laplace equation numerically for different configurations of two grains in order to compute the capillary forces and the geometric properties of the liquid bridge.

The model enables the determination of the interfaces separating the different phases and the corresponding energy. These elements were used to validate the model from an energetic point of view, and it has been proved that it is important to take them into account. It was shown that if one or all the energetic terms related to the interfaces were neglected, the energy balance is not verified.

The model also takes into account the roughness of the grains models as a positive or negative separation of two grains. The roughness is shown to have an importance influence on the norm and the evolution of the capillary forces.

Thermodynamic interpretations of DEM simulations of an assemblies of grains were

used to discuss concept of effective stress in the pendular regime. Although, the averaged contact stress calculated by the Love-Weber formula is frequently supposed to be the effective stress in partially saturated soils, It was however proved in this work that this assumption is not always valid. In the elastic regime, the contact stress is not equal to the effective stress derived from the energy of the deformation in the granular materials.

At the pic in a monotonic triaxial shear, the contact stress does not predict the rupture of the soil. Plotted in the (p_{cont}, q_{cont}) plane, the peak values do not fall on a unique Mohr-Coulomb envelop for all the possible particle size distribution. For all the authors considering that the contact stress is the micromechanical effective stress and presenting analytical formulations based on the Love-Weber formula, the domain of validity of their results remain to be defined.

The pendular model was also coupled with the funicular model in this thesis in order to simulate a full drainage. It is noticed that the addition of the pendular liquid bridge to the funicular regime has a noticeable impact on the behavior of partially saturated granular media. The presence of the menisci increases the value of the effective stress parameter χ and increase the difference between the χ obtained from the simulations and $\chi = S_r$.

9.1.2 Perspectives

The numerical model for the pendular regime has the potential to be extended to multiphysical coupling taking into account for example the different phenomena related to the change of temperature and salinity of the fluid. The transfer of water between the pores when the grains are deformed or when the menisci are broken is also an interesting option to be investigated.

More complex formulations of the effective stress based on the thermodynamic approach should then be considered. The energetic analysis that was presented in this thesis in the elastic regime can be extended to plasticity in order to build progressively a constitutive framework in which the material properties can be obtained by simulations or experiments.

To complete the study, a model for the imbibition can be developed. The pendular model is to be improved by improving local rules governing the coalescence of multiple pendular

bridges. The new geometry of the water in the pore after the fusion of the menisci is complex and corresponds to a minimum energy of interfaces. The correct configuration can be then determined through an iterating calculation to reach the minimum energy of the interfaces.

The funicular model is also adequate only for the small deformation, extension to higher deformation is one of the options to improve the model.

9.2 Multi-material system

9.2.1 Conclusions

In the multi-material system, DEM was used to study the compaction of a proppant region. In the first part, DEM was used to simulate the compaction of a granular pile of proppant between two rigid plates. The stress distribution induced by the proppant on the plates was determined. This stress distribution can be used in analytic analysis to improve the results of the studies that aim to determine the geometry of the fracture as a function of the applied stress, or in FEM simulations.

On the other side a DEM model was developed to study the interaction rock-proppant. The rock block was constructed using DEM that is found to be adequate to simulate a continuum elastic media. The comparison of the results for the geometry of the fracture with the analytic results developed for rigid shaped proppant fit very well. The rigid shaped proppant was afterwards replaced by a granular proppant of the same volume and the results for the fracture geometry were presented and compared with the results of the disc shaped rigid proppant case. It is shown that considering a rigid disc shaped proppant overestimates the volume of the fracture compared to a granular pile of proppant of the same volume.

9.2.2 Perspectives

More investigations on the geometry of the fracture can be done by considering two dissimilar rock blocks or a proppant with a different particle size distribution. The results can be also improved by considering that the grains do not remain intact during the compaction, the grains break which results in a decrease in the volume of the fracture.

The model is built in dry conditions; In reality the fracture is fully saturated. A model in fully saturated conditions accounting also for the evolution of the fluid pressure value after the proppant injection will also improve the results to approach more the reality.

Bibliography

[1] Aitchison, G. D. (1965). Moisture equilibria and moisture changes in soils beneath covered areas; a symposium in print.

[2] Andreotti, B., Forterre, Y., and Pouliquen, O. (2013). *Granular media: between fluid and solid*. Cambridge University Press.

[3] Asgian, M., Cundall, P., Brady, B., et al. (1995). The mechanical stability of propped hydraulic fractures: a numerical study. *Journal of Petroleum Technology*, 47(03):203–208.

[4] Baker, V. R. and Pyne, S. (1978). Gk gilbert and modern geomorphology. *American Journal of Science*, 278(2):97–123.

[5] Barree, R., Conway, M., et al. (2001). Proppant holdup, bridging, and screenout behavior in naturally fractured reservoirs. In *SPE Production and Operations Symposium*. Society of Petroleum Engineers.

[6] Biot, M. A. (1941). General theory of three-dimensional consolidation. *Journal of applied physics*, 12(2):155–164.

[7] Bishop, A. and Donald, I. (1961). The experimental study of partly saturated soil in the triaxial apparatus. In *Proceedings of the 5th International Conference on Soil Mechanics and Foundation Engineering, Paris*, volume 1, pages 13–21.

[8] Bishop, A. W. (1960). *The principles of effective stress*. Norges Geotekniske Institutt.

[9] Bishop, A. W. and Blight, G. (1963). Some aspects of effective stress in saturated and partly saturated soils. *Geotechnique*, 13(3):177–197.

[10] Blight, G. (1967). Effective stress evaluation for unsaturated soils. *Journal of the Soil Mechanics and Foundations Division*, 93(2):125–148.

[11] Brenner, H. (1964). The stokes resistance of an arbitrary particle—iv arbitrary fields of flow. *Chemical Engineering Science*, 19(10):703–727.

[12] Brooks, R. H. and Corey, A. T. (1964). Hydraulic properties of porous media and their relation to drainage design. *Transactions of the ASAE*, 7(1):26–0028.

[13] Brown, S. R. and Scholz, C. H. (1985). Broad bandwidth study of the topography of natural rock surfaces. *Journal of Geophysical Research: Solid Earth (1978–2012)*, 90(B14):12575–12582.

[14] Chang, C. S. and Kuhn, M. R. (2005). On virtual work and stress in granular media. *International Journal of Solids and Structures*, 42(13):3773–3793.

[15] Chareyre, B., Scholtès, L., and Darve, F. (2009). Micro-statics and micro-kinematics of capillary phenomena in dense granular materials. In Nakagawa, M. and Luding, S., editors, *Powder and Grains*, volume 1145 of *AIP Conference Series*, pages 927–930.

[16] Christoffersen, J., Mehrabadi, M., and Nemat-Nasser, S. (1981). A micromechanical description of granular material behavior. *Journal of Applied Mechanics*, 48(2):339–344.

[17] Clark, P. E., Quadir, J. A., et al. (1981). Prop transport in hydraulic fractures: a critical review of particle settling velocity equations. In *SPE/DOE Low Permeability Gas Reservoirs Symposium*. Society of Petroleum Engineers.

[18] Cundall, P. A. and Strack, O. D. (1979). A discrete numerical model for granular assemblies. *Geotechnique*, 29(1):47–65.

[19] Dangla, P. and Coussy, O. (2002). Approche énergétique du comportement des sols non saturés.

[20] Darve, F., Laouafa, F., and Servant, G. (2003). Discrete instabilities in granular materials. *Rivista Italiana di Geotechnica*, 3:57–67.

[21] Darve, F., Servant, G., Laouafa, F., and Khoa, H. (2004). Failure in geomaterials: continuous and discrete analyses. *Computer methods in applied mechanics and engineering*, 193(27):3057–3085.

[22] Dayan, A., Stracener, S. M., Clark, P. E., et al. (2009). Proppant transport in slickwater fracturing of shale gas formations. In *SPE Annual Technical Conference and Exhibition*. Society of Petroleum Engineers.

[23] El Shamy, U. and Gröger, T. (2008). Micromechanical aspects of the shear strength of wet granular soils. *International journal for numerical and analytical methods in geomechanics*, 32(14):1763–1790.

[24] Engel, J., Schanz, T., and Lauer, C. (2005). State parameters for unsaturated soils, basic empirical concepts. In *Unsaturated Soils: Numerical and Theoretical Approaches*, pages 125–138. Springer.

[25] Ennis, B. J., Li, J., Robert, P., et al. (1990). The influence of viscosity on the strength of an axially strained pendular liquid bridge. *Chemical Engineering Science*, 45(10):3071–3088.

[26] Fredlund, D. G. and Rahardjo, H. (1993). *Soil mechanics for unsaturated soils*. John Wiley & Sons.

[27] Gadde, P. B., Liu, Y., Norman, J., Bonnecaze, R., Sharma, M. M., et al. (2004). Modeling proppant settling in water-fracs. In *SPE annual technical conference and exhibition*. Society of Petroleum Engineers.

[28] Gili, J. and Alonso, E. (2002). Microstructural deformation mechanisms of unsaturated granular soils. *International journal for numerical and analytical methods in geomechanics*, 26(5):433–468.

[29] Gladwell, G. and Hara, T. (1981). The contact problem for a rigid obstacle pressed between two dissimilar elastic half-spaces. *The Quarterly Journal of Mechanics and Applied Mathematics*, 34(2):251–263.

[30] Gray, W. G. and Schrefler, B. A. (2001). Thermodynamic approach to effective stress in partially saturated porous media. *European Journal of Mechanics-A/Solids*, 20(4):521–538.

[31] Guo, P. (2014). Coupled effects of capillary suction and fabric on the strength of moist granular materials. *Acta Mechanica*, 225(8):2261–2275.

[32] Haimson, B. C. (1975). Deep in-situ stress measurements by hydrofracturing. *Tectonophysics*, 29(1):41–47.

[33] Hassanizadeh, S. M. and Gray, W. G. (1990). Mechanics and thermodynamics of multiphase flow in porous media including interphase boundaries. *Advances in water resources*, 13(4):169–186.

[34] Hill, R. (1958). A general theory of uniqueness and stability in elastic-plastic solids. *Journal of the Mechanics and Physics of Solids*, 6(3):236–249.

[35] Jain, S. P. and Gupta, R. C. (1974). In-situ shear test for rock fills. *Journal of the Geotechnical Engineering Division*, 100(9):1031–1050.

[36] Jennings, J. and Burland, J. (1962). Limitations to the use of effective stresses in partly saturated soils. *Géotechnique*, 12(2):125–144.

[37] Jiang, M., Leroueil, S., and Konrad, J. (2004). Insight into shear strength functions of unsaturated granulates by dem analyses. *Computers and Geotechnics*, 31(6):473–489.

[38] Kern, L., Perkins, T., Wyant, R., et al. (1959). The mechanics of sand movement in fracturing. *Journal of Petroleum Technology*, 11(07):55–57.

[39] Khalili, N. and Khabbaz, M. (1998). A unique relationship of chi for the determination of the shear strength of unsaturated soils. *Geotechnique*, 48(5).

[40] Khalili, N. and Zargarbashi, S. (2010). Influence of hydraulic hysteresis on effective stress in unsaturated soils. *Geotechnique*, 60(9):729–734.

[41] King, G. E. et al. (2010). Thirty years of gas shale fracturing: what have we learned? In *SPE Annual Technical Conference and Exhibition*. Society of Petroleum Engineers.

[42] Love, A. E. H. (1927). *A treatise on the mathematical theory of elasticity*. Cambridge University Press.

[43] Mangeney, A., Bouchut, F., Thomas, N., Vilotte, J., and Bristeau, M. (2007). Numerical modeling of self-channeling granular flows and of their levee-channel deposits. *Journal of Geophysical Research: Earth Surface*, 112(F2).

[44] Mani, R., Kadau, D., and Herrmann, H. J. (2013). Liquid migration in sheared unsaturated granular media. *Granular Matter*, 15(4):447–454.

[45] Marshall, E. (1967). The compression of a slab of ideal soil between rough plates. *Acta Mechanica*, 3(2):82–92.

[46] Mayer, R. P. and Stowe, R. A. (1965). Mercury porosimetry—breakthrough pressure for penetration between packed spheres. *Journal of colloid Science*, 20(8):893–911.

[47] Méheust, Y. and Schmittbuhl, J. (2003). Scale effects related to flow in rough fractures. *Pure and Applied Geophysics*, 160(5-6):1023–1050.

[48] Mehrabadi, M. M., Nemat-Nasser, S., and Oda, M. (1982). On statistical description of stress and fabric in granular materials. *International Journal for Numerical and Analytical Methods in Geomechanics*, 6(1):95–108.

[49] Mikami, T., Kamiya, H., and Horio, M. (1998). Numerical simulation of cohesive powder behavior in a fluidized bed. *Chemical Engineering Science*, 53(10):1927–1940.

[50] Molenkamp, F. and Nazemi, A. (2003a). Interaction between two rough spheres, water bridge and water vapour. *Geotechnique*, 53(2):255–264.

[51] Molenkamp, F. and Nazemi, A. (2003b). Interactions between two rough spheres, water bridge and water vapour. *Géotechnique*, 53(2):255–264.

[52] Montgomery, C. T., Smith, M. B., et al. (2010). Hydraulic fracturing: history of an enduring technology. *Journal of Petroleum Technology*, 62(12):26–40.

[53] MOREAU, J. J. (1994). Some numerical methods in multibody dynamics: application to granular materials. *European journal of mechanics. A. Solids*, 13:93–114.

[54] Morrow, N. R. (1970). Physics and thermodynamics of capillary action in porous media. *Industrial & Engineering Chemistry*, 62(6):32–56.

[55] Nazemi, A. and Majnooni-Heris, A. (2012). A mathematical model for the interactions between non-identical rough spheres, liquid bridge and liquid vapor. *Journal of colloid and interface science*, 369(1):402–410.

[56] Nichiporovitch, A. and Rasskazov, L. (1967). Shear strength of coarse fragmental materials.

[57] Nikooee, E., Habibagahi, G., Hassanizadeh, S. M., and Ghahramani, A. (2012). The effective stress in unsaturated soils: Insights from thermodynamics. In *Unsaturated soils: Research and applications*, pages 5–11. Springer.

[58] Nikooee, E., Habibagahi, G., Hassanizadeh, S. M., and Ghahramani, A. (2013). Effective stress in unsaturated soils: A thermodynamic approach based on the interfacial energy and hydromechanical coupling. *Transport in porous media*, 96(2):369–396.

[59] Palisch, T. T., Vincent, M., Handren, P. J., et al. (2010). Slickwater fracturing: food for thought. *SPE Production & Operations*, 25(03):327–344.

[60] Parker, M., Weaver, J., and Van Batenburg, D. (1999). Understanding proppant flowback. In *SPE annual technical conference*, pages 681–693.

[61] Perrot, A. (1968). Etude de la résistance au cisaillement des matériaux grossiers. *Rapport interne du laboratoire des Ponts et Chaussées*.

[62] Philipponnat, G. (1987). Le phicomètre, analyse de 200 essais de cisaillement in situ. In *Annales de l'ITBTP*, volume 460, pages 66–87.

[63] Philipponnat, G. and Zerhouni, M. (1993). Interprétation de l'essai au phicomètre. *Revue française de géotechnique*, (65).

[64] Pietsch, W. (1968). Tensile strength of granular materials.

[65] Pitois, O. (1999). *Assemblées de grains lubrifiés: elaboration d'un système modèle expérimental et étude de la loi de contact*. PhD thesis.

[66] Popovski, K., Dickson, M., Fanelli, M., et al. (1995). Greenhouse heating. *Geothermal energy.*, pages 125–154.

[67] Pyrak-Nolte, L. and Morris, J. (2000). Single fractures under normal stress: The relation between fracture specific stiffness and fluid flow. *International Journal of Rock Mechanics and Mining Sciences*, 37(1):245–262.

[68] Rabinovich, Y. I., Adler, J. J., Esayanur, M. S., Ata, A., Singh, R. K., and Moudgil, B. M. (2002). Capillary forces between surfaces with nanoscale roughness. *Advances in colloid and interface science*, 96(1):213–230.

[69] Radjai, F., Roux, S., and Moreau, J. J. (1999). Contact forces in a granular packing. *Chaos: An Interdisciplinary Journal of Nonlinear Science*, 9(3):544–550.

[70] Richefeu, V. (2005). *Approche par éléments discrets 3D du comportement de matériaux granulaires cohésifs faiblement contraints*. PhD thesis, Université Montpellier II-Sciences et Techniques du Languedoc.

[71] Richefeu, V., El Youssoufi, M. S., and Radjai, F. (2006). Shear strength properties of wet granular materials. *Physical Review E*, 73(5):051304.

[72] Rideal, E. and Davies, J. (1963). Interfacial phenomena.

[73] Schmittbuhl, J., Gentier, S., and Roux, S. (1993). Field measurements of the roughness of fault surfaces. *Geophysical Research Letters*, 20(8):639–641.

[74] Scholtès, L. (2008). *Modélisation micromécanique des milieux granulaires partiellement saturés*. PhD thesis, Institut National Polytechnique de Grenoble-INPG.

[75] Scholtès, L., Chareyre, B., Nicot, F., and Darve, F. (2009). Micromechanics of granular materials with capillary effects. *International journal of engineering science*, 47(1):64–75.

[76] Schrefler, B. (1984). *The finite element method in soil consolidation (with application to surface subsidence)*. PhD thesis, University College of Swansea.

[77] Seif El Dine, B. (2007). *Etude du comportement mécanique des sols grossiers à matrice*. PhD thesis, Marne-la-Vallée, ENPC.

[78] Selvadurai, A. P. S. (1994a). Separation at a pre-fractured bi-material geological interface. *Mechanics research communications*, 21(1):83–88.

[79] Selvadurai, A. P. S. (1994b). A unilateral contact problem for a rigid disc inclusion embedded between two dissimilar elastic half-spaces. *The Quarterly Journal of Mechanics and Applied Mathematics*, 47(3):493–510.

[80] Selvadurai, A. P. S. (2003). On an invariance principle for unilateral contact at a bimaterial elastic interface. *International journal of engineering science*, 41(7):721–739.

[81] Selvadurai, A. P. S. and Mahyari, A. T. (1998). Computational modelling of steady crack extension in poroelastic media. *International Journal of Solids and Structures*, 35(34):4869–4885.

[82] Selvadurai, A. P. S. and Suvorov, A. P. (2014). Thermo-poromechanics of a fluid-filled cavity in a fluid-saturated geomaterial. In *Proceedings of the Royal Society of London A: Mathematical, Physical and Engineering Sciences*, volume 470, page 20130634. The Royal Society.

[83] Shah, S. N. et al. (1982). Proppant settling correlations for non-newtonian fluids under static and dynamic conditions. *Society of Petroleum Engineers Journal*, 22(02):164–170.

[84] Soulié, F. (2005). *Cohésion par capillarité et comportement mécanique de milieux granulaires*. PhD thesis, Université Montpellier II-Sciences et Techniques du Languedoc.

[85] Stokes, G. G. (1851). On the composition and resolution of streams of polarized light from different sources. *Transactions of the Cambridge Philosophical Society*, 9:399.

[86] Terzaghi, v. K. (1936). The shearing resistance of saturated soils and the angle between the planes of shear. In *Proceedings of the 1st International Conference on Soil Mechanics and Foundation Engineering*, volume 1, pages 54–56. Harvard University Press Cambridge, MA.

[87] Vallé, N. (1998). Mesure de la résistance du cisaillement des sols grossiers à la boîte de cisaillement. *Mémoir de DEA, Ecole Centrale de Paris*.

[88] Van Zwol, P., Palasantzas, G., and De Hosson, J. T. M. (2007). Influence of random roughness on the adhesion between metal surfaces due to capillary condensation. *Applied Physics Letters*, 91(10):101905.

[89] Van Zwol, P., Palasantzas, G., and De Hosson, J. T. M. (2008). Influence of roughness on capillary forces between hydrophilic surfaces. *Physical Review E*, 78(3):031606.

[90] Wan, R., Khosravani, S., and Pouragha, M. (2014). Micromechanical analysis of force transport in wet granular soils. *Vadose Zone Journal*, 13(5).

[91] Weber, J. (1966). Recherches concernant le contraintes intergranulaires dans les milieux pulvérents; applicationa la rhéologie de ces milieux. *Cahiers français rhéol*, 2:161–170.

[92] Wheeler, S., Sharma, R., and Buisson, M. (2003). Coupling of hydraulic hysteresis and stress–strain behaviour in unsaturated soils. *Géotechnique*, 53(1):41–54.

[93] Yuan, C., Chareyre, B., and Darve, F. (2015a). Pore-scale simulations of drainage in granular materials: finite size effects and the representative elementary volume. *Advances in Water Resources*, pages –.

[94] Yuan, C., Chareyre, B., and Darve, F. (2015b). Pore-scale simulations of two-phase flow in granular materials. *Geomechanics group annual report*.

[95] Zerhouni, M. (1991). *Rôle de la pression interstitielle négative dans le comportement des sols: application au calcul des routes*. PhD thesis, Châtenay-Malabry, Ecole Centrale Paris.